The failure modelling of structures composed of quasi-brittle materials via IGABEM and the Extended Lumped Damage approach

Modelagem da falha de estruturas compostas por materiais quase-frágeis via IGABEM e a abordagem do Dano Concentrado Expandido

Deborah Cristina Nardi

Dissertação de Mestrado do Programa de Pós-Graduação em Engenharia Civil (Engenharia de Estruturas) da Escola de Engenharia de São Carlos, Universidade de São Paulo

EESC · USP

Deborah Cristina Nardi

The failure modelling of structures composed of quasi-brittle materials via IGABEM and the Extended Lumped Damage approach

Modelagem da falha de estruturas compostas por materiais quase-frágeis via IGABEM e a abordagem do Dano Concentrado Expandido

Dissertation presented to the São Carlos School of Engineering, University of São Paulo, for obtaining the Master's degree in Sciences - Graduate Program in Civil Engineering (Structural Engineering).

Concentration Area: Structures

Advisor: Prof. Dr. Edson Denner Leonel

CORRECTED VERSION

(Original version is available at São Carlos School of Engineering)

São Carlos

2024

FOLHA DE JULGAMENTO

Candidata: Bacharela **DEBORAH CRISTINA NARDI**.

Título da dissertação: "A modelagem da falha de estruturas compostas por materiais quase frágeis via IGABEM e o modelo de dano concentrado expandido".

Data da defesa: 21/02/2024.

Comissão Julgadora	**Resultado**
Prof. Titular Edson Denner Leonel (Orientador) (Escola de Engenharia de São Carlos/EESC-USP)	APROVADA
Prof. Dr. Aref Kalilo Lima Kzam (Universidade Federal da Integração Latino-Americana/UNILA)	APROVADA
Prof. Dr. Caio Gorla Nogueira (Universidade Estadual Paulista "Júlio de Mesquita Filho"/UNESP - Bauru)	APROVADA

Coordenador do Programa de Pós-Graduação em Engenharia Civil (Engenharia de Estruturas):
Prof Associado **Ricardo Carrazedo**

Presidente da Comissão de Pós-Graduação:
Prof. Titular **Carlos De Marqui Junior**

To my beloved brother, Rodrigo (in memorian).

Ao meu amado irmão, Rodrigo (em memória).

ACKNOWLEDGEMENTS

AGRADECIMENTOS

Gostaria de agradecer aos meus pais, Lurdes e Ademir, pelo amor e apoio incondicional ao longo da minha vida. Vocês são minha inspiração, minha paixão e minha motivação.

Gostaria de agradecer ao meu irmão, Rodrigo, que agora está olhando para nós do céu, por me ensinar o verdadeiro significado de amar e cuidar.

Este trabalho não teria sido possível sem o apoio do meu orientador, Prof. Dr. Edson Denner Leonel, que tem sido tão paciente e que me guiou ao longo desses anos. Sou grata pela oportunidade de trabalhar com o senhor.

Também gostaria de expressar minha gratidão ao Prof. Dr. Julio Flórez-López, meu primeiro mentor, que me apresentou à alegria da mecânica computacional.

Obrigada às minhas irmãs, Samanta e Joyce, por tornarem minha vida muito mais divertida e cheia de amor. Nós podemos não compartilhar o mesmo sangue, mas compartilhamos o mesmo coração.

Obrigada ao meu querido parceiro, Sérgio, por transformar esses dois últimos anos em luz, alegria e amor.

Sou muito grata pela equipe de pesquisa do Dr. Leonel, por todos os momentos juntos aprendendo, compartilhando, rindo e crescendo. Um agradecimento especial ao Daniel e Matheus R., que me guiaram, me ensinaram e me ajudaram de muitas maneiras durante esta pesquisa.

Obrigada aos meus amigos da UNILA e da BU: Bianca, Thays, Rafa, Erik, Isa, Lucca e Lisa. É ótimo ainda compartilhar momentos com vocês, mesmo que estejamos longe um do outro.

Também gostaria de agradecer aos meus amigos de São Carlos: Jéssica, Chiara, Gilmara, Juliana, Naomi, Lara, Emerson, B.O., Gabriel, Matheus Y. e Caio. Obrigada por todos os momentos divertidos ao longo desses anos e por tornar essa difícil jornada do mestrado muito melhor.

Por último, mas não menos importante, gostaria de agradecer ao CNPQ (Conselho Nacional de Pesquisa), pelo apoio financeiro.

ABSTRACT

NARDI, D. C. **The failure modelling of structures composed of quasi-brittle materials via IGABEM and Extended the Lumped Damage approach**. 2024. 117p. Dissertation (Master) - Escola de Engenharia de São Carlos, Universidade de São Paulo, São Carlos, 2024.

Accurately predicting the mechanical behavior of structures poses a challenge for civil engineers, requiring the translation of numerous fundamental aspects into the adopted numerical model. For instance, the type of the structure's material is a factor that needs to be considered. A significant range of quasi-brittle materials is present in the engineering world, due to their versatility and applicability. Ceramics and cementitious are classic examples of this class of materials. In parallel, it is known that the mechanical response is highly affected when physical phenomena such as cracking appear and start to propagate in elements composed of quasi-brittle materials. The strong material nonlinear behaviour caused by this problem can be represented in the numerical models by the damage mechanics, a theory which incorporates the internal variable of damage into the problem. In this context, the present work presents the development of a damage formulation via the Boundary Element Method (BEM). The adopted constitutive model is the Lumped Damage Mechanics for bidimensional media, the so-called Extended Lumped Damage Mechanics (XLMD). The model effectively captures the material nonlinear behavior due to crack propagation. Nonlinear analysis in the BEM context proves to be a challenging task. The main reason is the requirement for domain discretization, making the use of a boundary-based method unfeasible. In light of this, the present work proposes the coupling of XLDM in the context of an isogeometric analysis in Boundary Element Method (IGABEM). Quadrilateral cells are employed to account for the nonlinear effects via the initial stress field approach. The domain is only discretized where the damage is expected to propagate, enabling the application of BEM in the context of damage mechanics. A total of five examples are presented: the initial two ones for validating the IGABEM formulation and the later ones for validating the proposed damage approach. The results achieved by the proposed formulation are compared with numerical and experimental outcomes available in the literature. A good agreement with both experimental and numerical findings are achieved. The proposed approach is promising and improvements are proposed for future works.

Keywords: boundary element method; isogeometric analysis; extended lumped damage mechanics; nonlinear analysis.

RESUMO

NARDI, D. C. **Modelagem da falha de estruturas compostas por materiais quase-frágeis via IGABEM e a abordagem do Dano Concentrado Expandido**. 2024. 117p. Dissertation (Master's degree) - Escola de Engenharia de São Carlos, Universidade de São Paulo, São Carlos, 2024.

Prever com precisão o comportamento mecânico de estruturas representa um desafio para os engenheiros civis, exigindo a tradução de inúmeros aspectos fundamentais no modelo numérico adotado. Por exemplo, o tipo do material estrutural é um aspecto que precisa ser levado em consideração. Uma variedade significante de materiais quase-frágeis está presente na engenharia, devido a sua versatilidade e aplicabilidade. Em paralelo, sabe-se que a resposta mecânica é altamente afetada quando fenômenos físicos como a fissuração aparecem e iniciam o processo de propagação em elementos feitos de tal material. O forte comportamento não linear causado por esse problema pode ser representado em modelos númericos por intermédio da mecânica do dano, teoria a qual incorpora a variável interna de dano ao problema. Neste contexto, o presente trabalho apresenta o desenvolvimento de uma formulação de dano via Método dos Elementos de Contorno (BEM). O modelo constitutivo adotado é a Mecânica do Dano Concentrado Expandida (MDCX). O modelo captura efetivamente o comportamento material não linear devido à propagação de fissuras. A análise não linear no contexto do MEC é considerada uma tarefa desafiadora. O principal motivo é a exigência de discretização de domínio, inviabilizando o uso de um método baseado em apenas discretização de contorno. Diante disso, o presente trabalho propõe o acoplamento da MDCX no contexto de uma análise isogeométrica no Método dos Elementos de Contorno (IGABEM). Células quadriláteras são empregadas para considerar os efeitos não lineares via abordagem de campo de tensões iniciais. O domínio é discretizado apenas onde se espera que o dano se propague, possibilitando a aplicação do MEC no contexto da mecânica do dano. Um total de cinco exemplos são apresentados: os dois primeiros para validação da formulação do IGABEM e os últimos para validação da abordagem de dano proposta. Os resultados alcançados pela formulação proposta são comparados com respostas numéricas e experimentais disponíveis na literatura. Uma boa concordância com resultados experimentais e numéricos é alcançada. A abordagem proposta é promissora e melhorias são propostas para trabalhos futuros.

Palavras-chave: método dos elementos de contorno; análise isogeométrica; mecânica do dano concentrado expandida; análise não-linear.

LIST OF FIGURES

CONTENTS

1 INTRODUCTION

Materials characterized by a gradually decreasing stress after the stress peak, known as softening, such as ceramic and cementitious ones, are called quasi-brittle materials (SHAH; SWARTZ; OUYANG, 1995). These are heterogeneous materials with brittle constituents, which typically do not lose all their capacity of load-carrying at the onset of damage. There is a gradual degradation of the material strength, which comes from the microscale decohesion and damage mechanisms (NARAYAN; ANAND, 2019).

Besides, quasi-brittle materials present large extension of strain softening zones, which has been defined as the deterioration of material strength with increasing strain, reflecting the material's ability to resist crack propagation (LEUNG, 2001). The microcracks triggered in the damaging process come from uniformly distributed isotropic damage, which becomes localized until it evolves into a macro-crack (SOARES; ITURRIOZ, 2016).

In this context, it is important to point out that concrete structures, in which the main constituent is quasi-brittle, have been employed widely in engineering practice. Examples of such structures, illustrated in Figure 1, contribute significantly to improving the quality of human life worldwide. Hence, concrete is considered one of the main structural materials used in construction and it belongs to a research field that has gained notoriety in the last century since engineers started to look for improvements in safety and economic issues (BARBOSA *et al.*, 1998; HAIFENG; JIANGUO, 2009).

Once the concrete is relatively weak and brittle in tension, concrete cracking and the interactions between steel and cracked concrete can cause highly nonlinear material behaviour. The failure of many structures is due to this crack propagation (HU; SCHNOBRICH, 1990). Mechanical models can capture the material's nonlinear behaviour, as well as predict crack initiation and propagation, by simulating how a structure responds to applied loads and physical, thermal, or chemical phenomena.

The correct understanding and the mechanical modelling of the damage process are of vital importance to discuss the effects of material deterioration in macroscopic behaviour. For this reason, according to Ghrib and Tinawi (1995), a systematic relationship to interrelate the defects distribution and such macroscopic behaviour can be given through the introduction of an internal variable. This variable directly characterizes the microcracks distribution, establishing equations that describe both its evolution and the mechanical behaviour of the damaged element. Thus, the spread of diffuse cracking is continually represented by the internal damage variable.

Therefore, following the concepts presented in Flórez-López, Marante and Picón (2015), as the goal of damage mechanics involves the description and quantification

Figure 1 – (a) Concrete section of Itaipu Dam (b) Concrete tunnel in the São Paulo subway
and (c) Concrete bridge in the city Winnipeg, Canada.

(a)   (b)   (c)
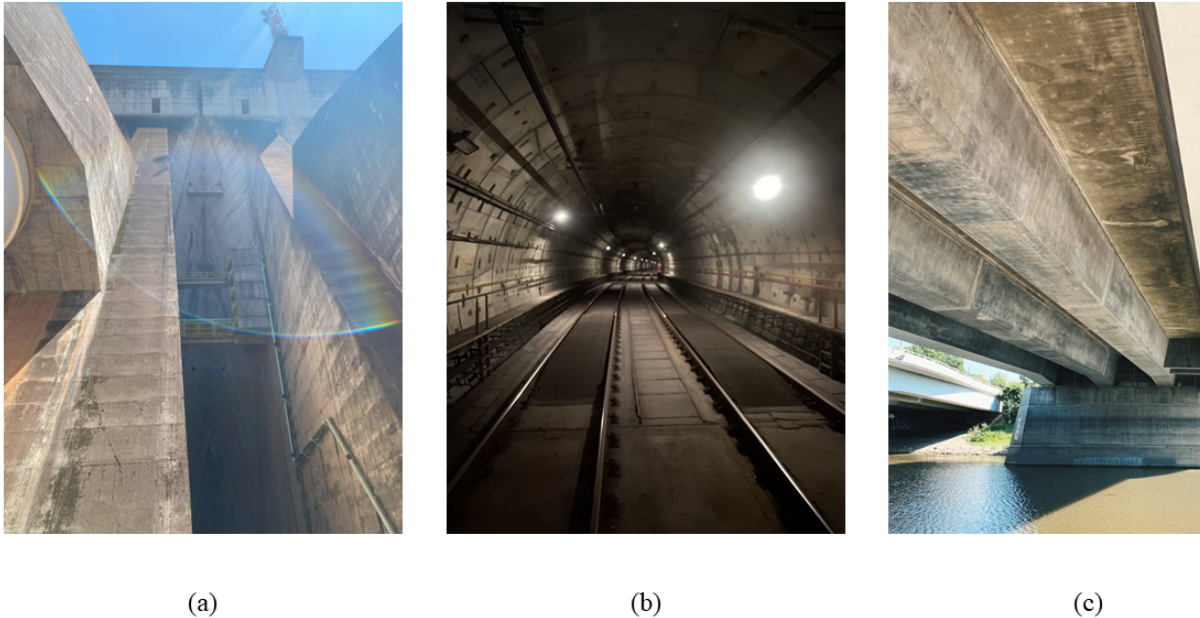
Source: The author.

of these flaws, the authors proposed a nonlinear theory for that purpose, the so-called
Lumped Damage Mechanics (LDM). The LDM is considered an alternative form of damage
mechanics and it was primarily created to provide a better description of the structural
deterioration phenomena for applications in civil engineering (AMORIM, 2016).

The LDM has its roots in bar elements, where it is commonly utilized. Nevertheless,
as it is a comprehensive theory, its applications go beyond. The pioneering work from
Amorim (2016) extends the LDM to any continuous media analysis, being then named
Extended Lumped Damage Mechanics (XLMD). All the works available in the literature
considering either LDM or XLDM use the Finite Element Method (FEM) for solving the
numerical problem. A different proceeding, such as the Boundary Element Method (BEM),
for example, has never been considered yet, which inspires the developments herein.

Summarily, while the FEM is a domain discretization method for solving differential
equations, the BEM provides boundary discretization and the solution to boundary integral
equations. Hence, in the BEM, the numerical discretization is conducted at reduced
dimensionality of the problem, i.e., for problems in two spatial dimensions, for example,
the discretization is performed over boundary curves. This reduced dimension enables
smaller linear systems, less computer memory requirements, and consequently, more
efficient computation (CHENG; CHENG, 2005).

The BEM has a wide range of applications in several engineering areas: geotechnics

(PROCHÁZKA, 1992; LIANG *et al.*, 2012; PANJI; ANSARI, 2017; NIE *et al.*, 2020), fluid mechanics (RAVNIK; ŠKERGET; HRIBERŠEK, 2004; HELTAI *et al.*, 2017), in thermoelasticity (HOSSEINI-TEHRANI; ESLAMI, 2000; ZHANG; QU; CHEN, 2013), fracture mechanics (PAN, 1999; QIN; MAI, 2002; OLIVEIRA; LEONEL, 2013; CORDEIRO; LEONEL; BEAUREPAIRE, 2017), and others.

Added to these applications, it is important to mention that crack growth simulation is one of the most appealing applications of the BEM due to the ability of the method to automatically follow the path of a growing crack with limited remeshing and no user intervention. Furthermore, the BEM can also be used for plasticity analysis, where the potential plastic zone can be discretized into cells (LEITAO; ALIABADI; ROOKE, 1995; ALIABADI, 2002).

As the BEM provides a very good precision for the stress field evaluation (RAVEENDRA; CRUSE, 1989; MELLINGS; BAYNHAM; ADEY, 2005; LEONEL; VENTURINI; CHATEAUNEUF, 2011), the use of this method allows an adequate estimative of the adopted constitutive model, predicting accurately the real behaviour of the structures.

In this context, the present study aims to be the first to propose a model using the XLDM formulation within BEM. It is believed that besides making use of a recent theory that can predict the mechanical response of quasi-brittle materials, the range of BEM applications is also expanded. These contributions are fundamental for enhancing nonlinear discretizations methods and for broadening computational mechanics in terms of efficiency and computational time and costs.

1.1 Research Group Development Records

This topic presents the research group's works developed over the past few years, which examine the deteriorating process of structures using damage models. For instance, in light of providing a computational model that can estimate the service life of reinforced concrete structures under the corrosion phenomenon, Pellizzer (2015) treated this problem in reinforced concrete structures subjected to chloride penetration through a mechanical-probabilistic approach. The study of Pellizzer (2015) was the first contribution that considered a damaging technique.

In the proposed model, the mechanical nonlinear analysis is performed with (FEM) taking into account the Mazars damage model to describe the concrete mechanical behaviour, while the steel behaviour is determined by the elastoplastic model. The results show that the rigidity of the structure is degraded as the corrosive process advances. For the same loading value, higher displacements and strains are obtained.

The model proposed by Pellizzer (2015) however has some restrictions. For instance, some points worth mentioning are: (i) the model is only valid for the analysis of frames; (ii)

the plastic strains in unloading situations are neglected; (iii) the unilateral behaviour of the concrete, which is the stiffness recovery caused by the cracking closure, is not considered, once the Mazars model is formulated only for increasing loads. Such aspects could not be taken into consideration due to the intrinsic limitations of the adopted damage model.

Still regarding the corrosion problem, Coelho (2017) proposed a model for evaluating the mechanical degradation of the same kind of structures. Unlike Pellizzer (2015), corrosion by carbonation is also considered in this work. In addition, the Lumped Damage Mechanics (LDM) model rather than the Mazars model describes the process of structural deterioration. The LDM presents fewer restrictions when compared to the Mazars model. For instance, the model has several advantages, such as the consideration of inelastic hinges, the ability to describe plastic strains during unloading situations, and the inclusion of the cracking closure effect.

In this sense, to better describe the corrosive process, the lumped damage law is modified in this work to include a state variable of corrosion. Thus, a corrosion evolution law is given, based on semi-empirical equations, available in the literature. The results indicate that, when corrosion is considered, the structure's critical failure values alter significantly. The strength is penalized by the damage evolution as well. Similarly as demonstrated in Pellizzer (2015), when a structure's stiffness is reduced, the strain values increase. Also, alike Pellizzer (2015), the model proposed by Coelho (2017) is also restricted to the analysis of frames.

A subsequent damage work is proposed by Silva (2023), where a three-dimensional multiphysics model is developed to evaluate the mechanical behaviour of reinforced concrete structures subjected to corrosion. The model is based on the Finite Element Method (FEM) as well, and it considers the chloride penetration in concrete. Similar to Pellizzer (2015), the Mazars damage model is adopted to describe the mechanical behaviour in a positional formulation of the FEM. One limitation of this study lies in the challenge of achieving objectivity in the solution, primarily attributed to the strain localization phenomenon. To address this issue, the author employed a regularization technique for fracture energy, a widely accepted approach in the literature.

Mentioning at this point the current contributions in the team research, parallel to this dissertation, the continuation of Teles (2022) is being developed. Differently from Pellizzer (2015) and Coelho (2017), the work of Teles (2022) addresses two-dimensional problems. The author advanced with XLDM formulations, by introducing a nonlinear damage law in the element proposed by Amorim (2016), improving the representation of material behaviour after the elastic regime. A great advantage of using the LDM model is that it circunvents the strain localization problem, which is a common issue in most damage models. In this sense, the work from Teles (2022) is the main used to contrast with the results provided via FEM. Also, as the proposed nonlinear damage law given

by the author shows promising results and solution objectivity, the dissertation herein developed makes use of this law for describing the cracking evolution.

1.2   Objectives and Contributions

The main objective of the present work is to implement the Extended Lumped Damage Mechanics (XLDM) within Boundary Element Method (BEM) framework, for obtaining the representation of the mechanical behaviour of quasi-brittle materials, such as concrete.

As specific objectives, it is aimed to:

- Develop a nonlinear IGABEM formulation based on the XLDM theory and propose a predictor-corrector algorithm for solving the nonlinear algebraic system;
- Implement quadrileteral cells for capturing the nonlinear behaviour via the initial stress field approach;
- Obtain results that allow the evaluation of the mechanical behaviour of selected examples (damage evolution, stiffness reduction, force-displacement relationship, and others);
- Carry out a comparative analysis, evaluating the potential of the implemented numerical method, contrasting with XLDM via FEM formulations that are available in the literature.

1.3   Methodology

This master's dissertation contributes to the development of the research group on damage models of the Department of Structural Engineering from the São Carlos School of Engineering at the University of São Paulo, under the supervision of Dr. Edson Denner Leonel. As previously specified, the present study is the pioneer involving BEM and damage mechanics in the research group.

Firstly, a literature review using the main available databases (ScienceDirect, Scopus and Web of Science, for example) is carried out to provide a strong theoretical foundation, clearly explaining the main issues that drive the present research.

In parallel to it, the construction of BEM strategies for coupling the XLDM theory is performed. For this, an isogeometric formulation is implemented, along with extra numerical tools that broaden the applicability of the BEM. Non-homegenous and body forces effects, for instance, are considered. A refinement strategy is also implemented, which is based on the knot-insertion technique. Linear problems are addressed, for assesing the accuracy of the numerical implementation. In sequence, via a nonlinear analysis, it is expected to evaluate the mechanical behaviour of quasi-brittle materials by a stress field correction. For such purposes, an in-house code is implemented in FORTRAN 90 language.

After the selection of examples of interest for showing the potential of the new formulation, the numerical results are contrasted with the ones given by the FEM available in the literature. Computational efforts and the results accuracy, when compared to the structure's experimental response, are highlighted. The main contributions are then pointed out and suggestions for future works are made.

1.4   Layout of the Dissertation

The present dissertation is organized as follows: at first, the theoretical basis of the adopted numerical method, the Boundary Element Method (BEM), is presented in Chapter 2. The main concepts of the method are introduced, as well as the main formulations and the numerical discretization procedure. In this topic, the isogeometric analysis (IGA) concept is also presented, as it is the basis for the numerical implementation. Extra techniques that broaden the applicability of the BEM are also examined: the Galerkin Vector Approach approximates body forces, the subregions technique handles non-homogeneous materials, and the knot-insertion strategy refines the the isogeometric boundary mesh.

In sequence, in Chapter 3, introduces BEM strategies for solving nonlinear problems. In this work, the initial stress field approach is adopted. The integral representation as well as the algebraic system are presented. Insights on coupling a constitutive model into the BEM framework are also given. As the material nonlinear behavior requires a domain discretization, the cells formulation is also discussed. The adopted numerical integration techniques for eliminating the singularities are also presented.

Afterwards, the Lumped Damage Mechanics (LDM) and the Extended Lumped Damage Mechanics (XLDM) theories are presented in Chapter 4. The main concepts of the theories are introduced, as well as the numerical discretization procedure. Additionally, the nonlinear damage law proposed by Teles (2022), serving as the foundation for the numerical implementation, is discussed. The numerical implementation is then described, highlighting the main aspects of the Algorithm.

Finally, in Chapter 5, five numerical examples are presented and discussed. The first and second examples are linear elastic problems, which are used to verify the accuracy of the IGABEM implementation. The subsequent examples are nonlinear problems, which evaluate the potential of implemeting the XLDM into IGABEM. Computational efforts and the accuracy of the results, when compared to the structure's experimental response, are highlighted. The main contributions are then pointed out and suggestions for future works are made.

2 THE BOUNDARY ELEMENT METHOD (BEM)

Engineering problems have been represented by physical laws which can be mathematically described by differential equations and boundary conditions (BCs). For solving these boundary value problems, it is aimed to determine a response to given BCs. In general, analytical solutions of boundary value problems satisfying both the differential equations and the BCs can only be obtained for a few range of problems, usually with simple geometry and BCs. Hence, approximation solutions are required. For this, one needs to decide between satisfying only the differential equation or the BCs, i.e, it is necessary to choose one of the two and minimize the error of the other one. For example, if the BCs are chosen to be exactly satisfied, the error in satisfying the differential equation is then required to be minimized. This is the purpose of weigthed residue and Ritz methods, which are the basis of the Finite Element Method (FEM).

Notwithstanding, it is known that in some cases, the physical laws representing real problems can be described in terms of integral equations as well. Thus, the most general and most commonly used method for solving such integral equations is the Boundary Element Method (BEM). Similarly, in this case, the functions used for approximating the solution inside the domain are chosen to be those which exactly satisfy the governing differential equations, then the error in satisfying the boundary conditions is minimized and this involves a boundary integral (ALIABADI, 2002; BEER; SMITH; DUENSER, 2008).

According to Leonel (2006), Abel in 1823 was the first to apply integral equations to solve an isochronous pendulum problem. Following Cheng and Cheng (2005), Green in the year 1828 formulated for the first time an integral equation for solving problems of electrostatics and magnetism. In addition to them, other authors such as Euler, Lagrange, Laplace, Fourier, and Poisson also formulated works which have been fundamental for the development of differential and integral equations.

In the field of structural analysis, boundary integral methods were introduced by Russian authors such as Muskelishvili, Mikhlin and Kupradze and the methods at that time were considered difficult to be implement numerically. By using Betti's and Somiglina's equation, Rizzo presented the direct formulation for elastostatic problems (ALIABADI; BREBBIA, 1970).

At the beginning of the twentieth century, the introduction of variational methods for partial differential equations led to a loss of importance of integral equations for the area under analysis. That happened due to the difficulty of formulating precise results on existence and uniqueness employing classical integral equations. However, along with

the advancement of scientific computing in the middle of the twentieth century, the need for numerical methods for solving boundary value problems began to grow (SAUTER; SCHWAB, 2010). The method presents some particularities concerning other numerical methods and some advantages that it has over such methods, especially over the domains ones, are:

- The resolution of boundary value problems for domains defined over geometricaly complex domains is simpler in terms of mesh generation, i.e., spatial discretization, since only contour meshes are needed, as opposed to an entire volume mesh (see Figure 2). This leads to a consequent reduction in model preparation time;

- For some parameter-dependent boundary value problems, such as problems in the area of electromagnetism under high frequencies, numerical methods based on integral boundary equations remain more stable for extreme parameter values when compared to domain discretization methods;

- The approach uses high-quality solutions (fundamental solutions), and it treats singularities more appropriately;

- The primary challenges of the method, such as the efficient resolution of fully populated systems of equations and numerical integration of improper integrals, are being overcome by means of sophisticated formulations that have been under continuous improvement since the 1980s.

Figure 2 – The domain method (FEM) and the boundary method (BEM).

FEM

BEM

The whole domain is discretized.

Only boundary is discretized.
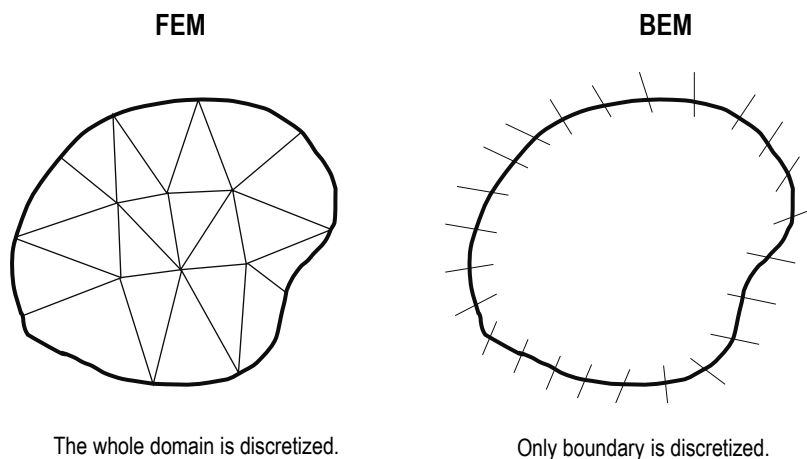
Source: Adapted from Tonyali and Ates (2018)

In this sense, traditional numerical solution techniques for integral equations include the Nyström or quadrature formula methods and the BEM collocation approach. Since approximately the 1980s to 1990s, the BEM Galerkin method has been increasingly important for discretizing boundary integral equations in practical applications (SAUTER;

SCHWAB, 2010). The reciprocal theorem, the weighted residual idea, and the variational approach are a few ways to derive the BEM formulations (ALIABADI, 2002). The first one (reciprocal theorem) is herein used to derive boundary integral equations.

2.1 Boundary Element Formulation for Linear Elasticity

The main concepts of the Theory of Linear Elasticity used for the boundary integral equations are presented in Appendix A. It is important to mention that more in-depth concepts of the Theory of Linear Elasticity are available in Timoshenko and Goodier (1934). The index notation (Einstein summation convention) is herein adopted.

2.1.1 Boundary Integral Equations

The formulation of the elastic problem requires the determination of the fundamental solution. This solution considers an infinite domain under the action of a singular load. In other words, the fundamental solution for displacements is then an expression which provides the displacements in any part of the domain due to the presence of a concentrated force acting at a certain point of a homogeneous solid of infinite dimensions. This concetrated force has its intensity described the Delta Dirac function. According to Brebbia and Walker (2016), the solution given in the following text is called the Kelvin solution. Thus, for obtaining such a solution, the concepts given in Aliabadi (2002) are herein followed and described in the sequence.

From the equilibrium equation and by means of the weighted residual method, the weak form of the problem is written as:

$$\int_\Omega \left(\sigma_{ij,j} + b_i \right) u_i^* d\Omega = 0 \tag{2.1}$$

where u_i^* is the weighting function corresponding to a displacement field from a self-equilibrated state. The integral related to $\sigma_{ij,j} u_i^*$ can be written according to:

$$\int_\Omega \sigma_{ij,j} u_i^* d\Omega = \int_\Omega \left(\sigma_{ij} u_i^* \right)_{,j} d\Omega - \int_\Omega \sigma_{ij} \varepsilon_{ij}^* d\Omega \tag{2.2}$$

once the following equality is valid:

$$\begin{aligned} \sigma_{ij} \varepsilon_{ij}^* &= \frac{1}{2} \left(\sigma_{ij} u_{i,j}^* + \sigma_{ij} u_{j,i}^* \right) \\ &= \frac{1}{2} \left(\sigma_{ij} u_{i,j}^* + \sigma_{ji} u_{j,i}^* \right) \\ &= \sigma_{ij} u_{i,j}^* \end{aligned} \tag{2.3}$$

The Divergence theorem (Gauss theorem), defines the relationship between the integrals of certain tensor operations in the domain of a field with operations on its boundary, by the following:

$$\int_\Omega f_{i,i} d\Omega = \int_\Gamma f_i n_i d\Gamma \tag{2.4}$$

where n_i denotes the outward unit normal vector. Thus, applying such theorem in the first integral of the right-hand side of Eq. (2.2), one obtains:

$$\int_\Omega \left(\sigma_{ij} u_i^*\right)_{,j} d\Omega = \int_\Gamma \sigma_{ij} n_j u_i^* d\Gamma = \int_\Gamma t_i u_i^* d\Gamma \tag{2.5}$$

where the last relation comes from Cauchy's formula given in (A.4).

Therefore, Eq. (2.2) is rewritten as:

$$\int_\Omega \sigma_{ij,j} u_i^* d\Omega = \int_\Gamma t_i u_i^* d\Gamma - \int_\Omega \sigma_{ij} \varepsilon_{ij}^* d\Omega \tag{2.6}$$

Replacing now Eq. (2.6) in Eq. (2.1), the following relationship is given:

$$\int_\Gamma t_i u_i^* d\Gamma + \int_\Omega b_i u_i^* d\Omega = \int_\Omega \sigma_{ij} \varepsilon_{ij}^* d\Omega \tag{2.7}$$

Remembering the Hooke's Law in Eq. (A.6), the equation on the right hand side can still be rewritten according to:

$$\int_\Omega \sigma_{ij} \varepsilon_{ij}^* d\Omega = \int_\Omega c_{ijkl} \varepsilon_{kl} \varepsilon_{ij}^* d\Omega = \int_\Omega \sigma_{ij}^* \varepsilon_{ij} d\Omega \tag{2.8}$$

Similar to the relation shown in Eq. (2.2), one has that $\sigma_{ij}^* \varepsilon_{ij} = \sigma_{ij}^* u_{i,j}$. Thus, Eq. (2.8) becomes:

$$\int_\Omega \sigma_{ij}^* \varepsilon_{ij} d\Omega = \int_\Omega \sigma_{ij}^* u_{i,j} d\Omega = \int_\Omega \left(\sigma_{ij}^* u_i\right)_{,j} d\Omega - \int_\Omega \left(\sigma_{ij}^*\right)_{,j} u_i d\Omega \tag{2.9}$$

which is equivalent to:

$$\int_\Omega \sigma_{ij}^* \varepsilon_{ij} d\Omega = \int_\Gamma \sigma_{ij}^* n_j u_i d\Gamma - \int_\Omega \left(\sigma_{ij}^*\right)_{,j} u_i d\Omega \tag{2.10}$$

Therefore, by recalling the equilibrium relationship with respect to the fundamental problem (similar to Eq. (A.3)), Eq. (2.7) is finally rewritten and the Betti's reciprocal work theorem for two equilibrated elastic states is finally obtained:

$$\int_\Gamma t_i u_i^* d\Gamma + \int_\Omega b_i u_i^* d\Omega = \int_\Gamma t_i^* u_i d\Gamma + \int_\Omega b_i^* u_i d\Omega \tag{2.11}$$

Consider now that the body force b_i^* corresponds to a point force represented by the Dirac delta function $\Delta(\mathbf{x}', \mathbf{x})$:

$$b_i^* = \Delta(\mathbf{x}', \mathbf{x}) e_i \tag{2.12}$$

in which $\mathbf{x}'$ is the point where the force is applied and e_i is a unit positive force vector in x_i direction. For the two-dimensional problems herein studied, e_i is a force per unit thickness. The Delta Dirac function has the property

$$\int_\Omega g(\mathbf{x})\Delta(\mathbf{x} - \mathbf{x}') d\Omega = g(\mathbf{x}') \tag{2.13}$$

which allows the domain term in the right hand side of Eq. (2.12) to be rewritten as

$$\int_\Omega b_i^* u_i d\Omega = \int_\Omega \Delta(\mathbf{x} - \mathbf{x}') e_i u_i d\Omega = u_i(\mathbf{x}') e_i \tag{2.14}$$

The displacement and the traction fields of where the point load is applied are given by

$$u_i^* = U_{ij}^*(\mathbf{x}', \mathbf{x}) e_j$$
$$t_i^* = T_{ij}^*(\mathbf{x}', \mathbf{x}) e_j \tag{2.15}$$

where U_{ij}^* and T_{ij}^* are, respectively, the displacement and the traction fundamental solutions. Appendix A presents the development for obtaining their expressions.

Replacing Eqs. (2.14) and (2.15) into Eq. (2.11), and then applying the property shown in (2.13), the Somegliana's identity is obtained:

$$u_i(\mathbf{x}') + \int_\Gamma T_{ij}^*(\mathbf{x}', \mathbf{x}) u_j(\mathbf{x}) d\Gamma = \int_\Gamma U_{ij}^*(\mathbf{x}', \mathbf{x}) t_j(\mathbf{x}) d\Gamma + \int_\Omega U_{ij}^*(\mathbf{x}', \mathbf{x}) b_j(\mathbf{x}) d\Omega \tag{2.16}$$

Such identity allows the determination of the internal displacement fields from the magnitudes known at the boundary. Differentiating the displacements in this equation with respect to the source point $\mathbf{x}$' gives

$$u_{i,k}(\mathbf{x}') + \int_\Gamma T_{ij,k}^*(\mathbf{x}', \mathbf{x}) u_j(\mathbf{x}) d\Gamma = \int_\Gamma U_{ij,k}^*(\mathbf{x}', \mathbf{x}) t_j(\mathbf{x}) d\Gamma + \int_\Omega U_{ij,k}^*(\mathbf{x}', \mathbf{x}) b_j(\mathbf{x}) d\Omega \tag{2.17}$$

Once Eq. (2.17) represents an integral equation written in terms of displacement gradients, by applying the strain-displacement relationship given in Eq. (A.5) and then by applying the Hooke's law, an integral representation for the stresses is obtained:

$$\sigma_{ij}\left(\mathbf{x}'\right) + \int_{\Gamma} S_{kij}^{*}\left(\mathbf{x}',\mathbf{x}\right) u_k(\mathbf{x}) d\Gamma = \int_{\Gamma} D_{kij}^{*}\left(\mathbf{x}',\mathbf{x}\right) t_k(\mathbf{x}) d\Gamma + \int_{\Omega} D_{kij}^{*}\left(\mathbf{x}',\mathbf{x}\right) b_k(\mathbf{x}) d\Omega \quad (2.18)$$

where D_{kij}^{*} and S_{kij}^{*} are obtained from $U_{ij,k}^{*}$ and $T_{ij,k}^{*}$, respectively. Their expressions are detailed in Appendix A as well.

2.1.2 Boundary Integral Equations for Points on the Boundary

The Somigliana's identity given in Eq. (2.16) is valid for any source point located inside the domain Ω. In order to resolve the boundary value problem, a limit analysis must be carried out to bring the source point to the boundary, i.e, it is necessary to consider the limit as $\mathbf{X}' \to \mathbf{x}' \in \Gamma$. Such a situation results in singular problems, once improper values are obtained in the integral formulations when this analysis is carried out $(r \mapsto 0)$.

For evaluating the source point on the boundary, consider that the domain is increased by a circular region of radius ε centred at $\mathbf{x}'$, as shown in Figure 3.

Figure 3 – Source point over the boundary.
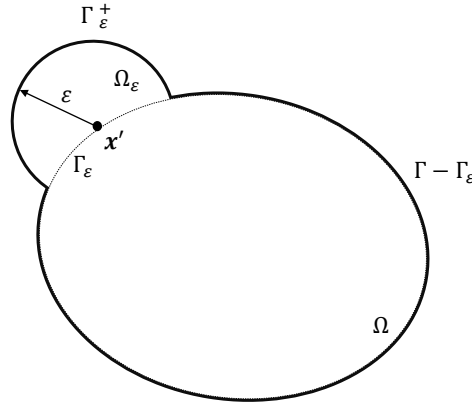
Source: Adapted from Aliabadi (2002).

The Somigliana's identity is then rewritten as:

$$u_i\left(\mathbf{x}'\right) + \int_{\Gamma-\Gamma_\varepsilon+\Gamma_\varepsilon^+} T_{ij}^{*}\left(\mathbf{x}',\mathbf{x}\right) u_j(\mathbf{x}) d\Gamma = \int_{\Gamma-\Gamma_\varepsilon+\Gamma_\varepsilon^+} U_{ij}^{*}\left(\mathbf{x}',\mathbf{x}\right) t_j(\mathbf{x}) d\Gamma + \int_{\Omega+\Omega_\varepsilon} U_{ij}^{*}\left(\mathbf{x}',\mathbf{x}\right) b_j(\mathbf{x}) d\Omega$$
$$(2.19)$$

where the following limit must be operated:

Figure 4 – Illustration of (a) the derivative of the distance r and of (b) a smooth boundary.

(a)

(b)
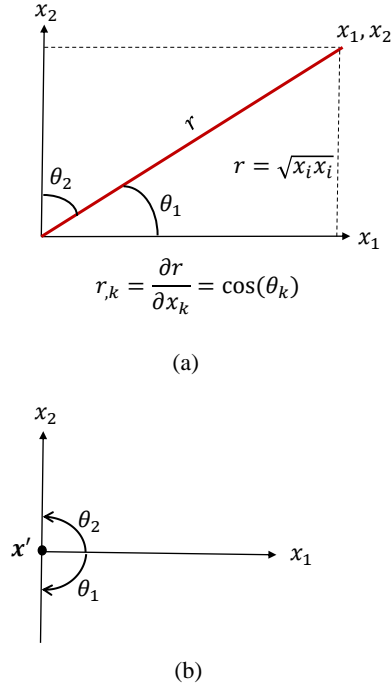
Source: The author.

$$\Gamma = \lim_{\varepsilon \to 0} \left(\Gamma - \Gamma_\varepsilon + \Gamma_\varepsilon^+ \right)$$
$$\Omega = \lim_{\varepsilon \to 0} (\Omega + \Omega_\varepsilon) \qquad (2.20)$$

Each term of the Eq. (2.19) is analyzed separately. The geometric relation shown in Figure 4a is considered for the development of the limits herein presented. Firstly, consider the domain integral given by:

$$\int_{\Omega+\Omega_\varepsilon} U_{ij}^* \left(\mathbf{x}', \mathbf{x} \right) b_j(\mathbf{x}) d\Omega = \int_\Omega U_{ij}^* \left(\mathbf{x}', \mathbf{x} \right) b_j(\mathbf{x}) d\Omega + \int_{\Omega_\varepsilon} U_{ij}^* \left(\mathbf{x}', \mathbf{x} \right) b_j(\mathbf{x}) d\Omega_\varepsilon \qquad (2.21)$$

Since the first term of the second member of the Equation (2.21) does not depend on ε, only the second term of the second member is studied. Considering the fundamental solution for the displacements as given in (B.10) and that $d\Omega_\varepsilon = \varepsilon d\varepsilon d\theta$, is results:

$$I = \lim_{\varepsilon \to 0} \left\{ \frac{-(3-4\nu)\delta_{lk}}{8_\pi\mu(1-v)} \int_{\theta_1}^{\theta_2} \int_0^\varepsilon \ln(\varepsilon)\varepsilon d\varepsilon d\theta + \frac{1}{8\pi\mu(1-v)} \int_{\theta_1}^{\theta_2} \int_0^\varepsilon r_{,l}r_{,k}\varepsilon d\varepsilon d\theta \right\} \qquad (2.22)$$

in which θ_1 and θ_2 are the angles illustrated in 4. After some manipulations, the first part of the limit shown above is rewritten as

$$I_1 = \lim_{\varepsilon \to 0} \left[\frac{-(3-4v)\delta_{lk}}{8\pi\mu(1-v)} \left(\frac{\varepsilon^2 \ln(\varepsilon)}{2} - \frac{\varepsilon^2}{4} \right) (\theta_2 - \theta_1) \right] \tag{2.23}$$

relation that vanishes to zero when L'Hôpital's rule is applied in the indeterminate form $\varepsilon^2 \ln(\varepsilon)$. Thus, the second part of the limit gives:

$$I_2 = \lim_{\varepsilon \to \infty} \left[\frac{1}{8\pi\mu(1-v)} \int_{\theta_1}^{\theta_2} \int_0^\varepsilon r_{,l} r_{,k} \varepsilon d\varepsilon d\theta \right] \tag{2.24}$$

which after several manipulations vanishes to zero as well. Hence, it is concluded that:

$$\lim_{\varepsilon \to 0} \int_{\Omega + \Omega_\varepsilon} U_{ij}^* \left(\mathbf{x}', \mathbf{x} \right) b_j(\mathbf{x}) d\Omega = \int_\Omega U_{ij}^* \left(\mathbf{x}', \mathbf{x} \right) b_j(\mathbf{x}) d\Omega \tag{2.25}$$

Analyzing now the first term on the right-hand side of Eq. (2.19), it is given that:

$$\int_{\Gamma - \Gamma_\varepsilon + \Gamma_\varepsilon^+} U_{ij}^* \left(\mathbf{x}', \mathbf{x} \right) t_j(\mathbf{x}) d\Gamma = \int_{\Gamma - \Gamma_\varepsilon} U_{ij}^* \left(\mathbf{x}', \mathbf{x} \right) t_j(\mathbf{x}) d\Gamma + \int_{\Gamma_\varepsilon^+} U_{ij}^* \left(\mathbf{x}', \mathbf{x} \right) t_j(\mathbf{x}) d\Gamma \tag{2.26}$$

Once again, the first term of Eq. (2.26) does not depend upon the external radius ε, which implies that only the second integral is of interest. Therefore, taking the limit

$$I = \lim_{\varepsilon \to 0} \int_{\Gamma_\varepsilon^+} U_{ij}^* \left(\mathbf{x}', \mathbf{x} \right) t_j(\mathbf{x}) d\Gamma \tag{2.27}$$

gives that

$$I = \lim_{\varepsilon \to 0} \left\{ \frac{-(3-4\nu)\delta_{lk}}{8\pi\mu(1-v)} \int_{\theta_1}^{\theta_2} \ln(\varepsilon)\varepsilon d\theta + \frac{1}{8\pi\mu(1-\nu)} \int_{\theta_1}^{\theta_2} r_{,l} r_{,k} \varepsilon d\theta \right\} \tag{2.28}$$

where the first limit goes to zero, similarly to the previous analysis, once L'Hôpital's rule is applied. Regarding the second part of the limit, after several mathematical manipulations, one obtains that $I = 0$, giving then that:

$$\lim_{\varepsilon \to 0} \int_{\Gamma_\varepsilon^+} U_{ij}^* \left(\mathbf{x}', \mathbf{x} \right) t_j(\mathbf{x}) d\Gamma = \int_\Gamma U_{ij}^* \left(\mathbf{x}', \mathbf{x} \right) t_j(\mathbf{x}) d\Gamma \tag{2.29}$$

Analogously, the term present on the left-hand side of Eq. (2.19) is written as:

$$\int_{\Gamma - \Gamma_\varepsilon + \Gamma_\varepsilon^+} T_{ij}^* \left(\mathbf{x}', \mathbf{x} \right) u_j(\mathbf{x}) d\Gamma = \int_{\Gamma - \Gamma_\varepsilon} T_{ij}^* \left(\mathbf{x}', \mathbf{x} \right) u_j(\mathbf{x}) d\Gamma + \int_{\Gamma_\varepsilon^+} T_{ij}^* \left(\mathbf{x}', \mathbf{x} \right) u_j(\mathbf{x}) d\Gamma \tag{2.30}$$

where the first integral is independent of ε, which implies that only the following limit should be taken

$$I = \lim_{\varepsilon \to 0} \int_{\Gamma_\varepsilon^+} T_{ij}^* \left(\mathbf{x}', \mathbf{x} \right) u_j(\mathbf{x}) d\Gamma \tag{2.31}$$

Once the displacement field is continuous in the boundary, the following limit is obtained:

$$I = u_j(\mathrm{x}') \lim_{\varepsilon \to 0} \int_{\Gamma_\varepsilon^+} T_{ij}^* (\mathrm{x}', \mathrm{x}) \, d\Gamma \tag{2.32}$$

Considering the traction fundamental solution presented in (B.13), the above limit can be operated as:

$$I = \lim_{\varepsilon \to 0} \int_{\Gamma_\varepsilon^+} -\frac{1}{4\pi(1-\nu)r} \left\{ \frac{\partial r}{\partial n} \left[(1-2\nu)\delta_{lk} + 2r_{,l}r_{,k} \right] + (1-2\nu)\left(n_{,l}r_{,k} - n_{,k}r_{,l} \right) \right\} u_j(\mathrm{x}') \tag{2.33}$$

As $d\Gamma_\varepsilon^+ = \varepsilon d\theta$, and as $\vec{r} \perp \vec{n}$ (which gives $\frac{\partial r}{\partial n} = 1$), Eq. (2.33) can be rewrriten as:

$$I = \lim_{\varepsilon \to 0} \left\{ \int_{\Gamma_\varepsilon} \frac{-(1-2\nu)}{4\pi(1-\nu)} \left[\frac{\delta_{lk} + n_l r_{,k} - n_k r_{,l}}{r} \right] d\Gamma + \int_{\Gamma_\varepsilon} \frac{-2}{4\pi(1-\nu)} \frac{r_{,l}r_{,k}}{r} d\Gamma \right\} u_j(\mathrm{x}') \tag{2.34}$$

Taking $l = k = 1$, and remembering the relations shown in Figure 4a, Eq. (2.34) becomes:

$$I = \left\{ \frac{\theta_1 - \theta_2}{2\pi} - \frac{1}{4\pi(1-\nu)} \left[\sin(\theta_2)\cos(\theta_2) - \sin(\theta_1)\cos(\theta_1) \right] \right\} u_j(\mathrm{x}') \tag{2.35}$$

Taking now $l = k = 2$, Eq. (2.34) gives:

$$I = \left\{ \frac{\theta_1 - \theta_2}{2\pi} + \frac{1}{4\pi(1-\nu)} \left[\sin(\theta_2)\cos(\theta_2) - \sin(\theta_1)\cos(\theta_1) \right] \right\} u_j(\mathrm{x}') \tag{2.36}$$

Finally, for $l = 1$ and $k = 2$ or $l = 2$ and $k = 1$, the limit goes to:

$$I = -\frac{1}{4\pi(1-\nu)} \left(\frac{-\cos(2\theta_2) + \cos(2\theta_1)}{2} \right) u_j(\mathrm{x}') \tag{2.37}$$

Such values (2.35-2.37) are defined for a general condition, i.e, for cases where the source point is localized in boundaries with discontinuous derivatives. However, for source points located in smooth boundaries, $\theta_1 = -\frac{\pi}{2}$ and $\theta_2 = \frac{\pi}{2}$ (see Figure 4b), resulting in

$$I = \begin{bmatrix} -\frac{1}{2} & 0 \\ 0 & -\frac{1}{2} \end{bmatrix} u_j(\mathbf{x}') \tag{2.38}$$

Thus, the integral equation of the elastic problem results in:

$$-\frac{1}{2}u_i\left(\mathbf{x}'\right) + u_i\left(\mathbf{x}'\right) + \int_\Gamma T^*_{ij}\left(\mathbf{x}',\mathbf{x}\right)u_j(\mathbf{x})d\Gamma = \int_\Gamma U^*_{ij}\left(\mathbf{x}',\mathbf{x}\right)t_j(\mathbf{x})d\Gamma + \int_\Omega U^*_{ij}\left(\mathbf{x}',\mathbf{x}\right)b_j(\mathbf{x})d\Omega$$

(2.39)

or better writing,

$$\frac{1}{2}u_i\left(\mathbf{x}'\right) + \int_\Gamma T^*_{ij}\left(\mathbf{x}',\mathbf{x}\right)u_j(\mathbf{x})d\Gamma = \int_\Gamma U^*_{ij}\left(\mathbf{x}',\mathbf{x}\right)t_j(\mathbf{x})d\Gamma + \int_\Omega U^*_{ij}\left(\mathbf{x}',\mathbf{x}\right)b_j(\mathbf{x})d\Omega \quad (2.40)$$

2.2 Numerical Discretization

As previously mentioned, the Boundary Element Method is a numerical method for solution of boundary integral equations, based on a discretization procedure (ALIABADI, 2002). Then, a boundary discretization for a finite number of elements is carried out (Figure 5), where for each element e, both the displacements and the tractions are approximated with interpolation functions and nodal values.

Figure 5 – Discretization of the boundary into elements.
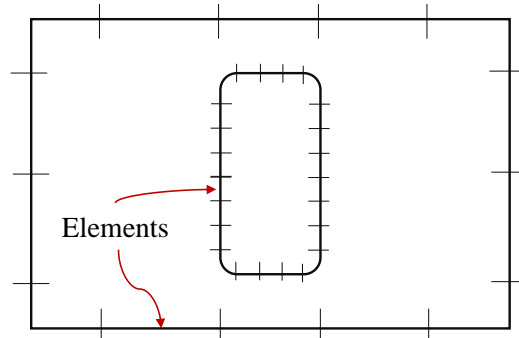
Source: Adapted from Aliabadi (2002).

In the following text, [] indicate matrices, while {} indicate vectors. The isoparametric formulation is herein considered, where the boundary coordinates $\mathbf{x}$, the displacement fields $\mathbf{u}(\mathbf{x})$ and the traction fields $\mathbf{t}(\mathbf{x})$ are approximated by the following interpolation functions, as shown:

$$\begin{aligned}
\mathbf{x}^e &= \sum_{\alpha=1}^{m} N_\alpha(\xi)\mathbf{x}_\alpha \\
\mathbf{u}^e &= \sum_{\alpha=1}^{m} N_\alpha(\xi)\mathbf{u}_\alpha \\
\mathbf{t}^e &= \sum_{\alpha=1}^{m} N_\alpha(\xi)\mathbf{t}_\alpha
\end{aligned}$$

(2.41)

where N_α are the shape functions defined in terms of non-dimensional coordinates ξ $(-1 \le \xi \le 1)$, as represented in Figure 6, and $\mathbf{x}_\alpha$, $\mathbf{u}_\alpha$ and $\mathbf{t}_\alpha$ are the values of the functions

Figure 6 – Boundary elements in the isoparametric space.
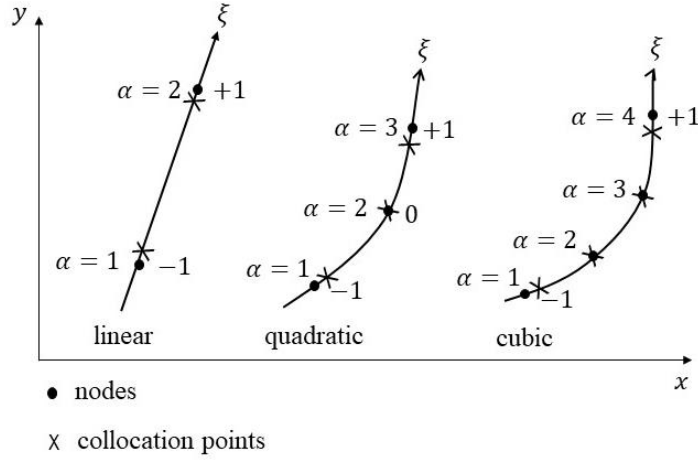
at node α. The interpolatory shape functions are derived from the Lagrangian polynomials, presented in 2.42.

$$N_\alpha(\xi) = \prod_{i=0, i \neq \alpha}^{m} \frac{\xi - \xi_i}{\xi_\alpha - \xi_i} \tag{2.42}$$

where its degree is $m - 1$, in which m is the total number of nodes, and they assume the value 1 at node α and zero at all other nodes. The sum of all shape functions must equal to 1 while the sum of its first derivative assumes the value of zero.

In matrix form, the kernels $T^*(\mathbf{x'},\mathbf{x})$ and $U^*(\mathbf{x'},\mathbf{x})$ can be presented as:

$$\boldsymbol{T}^* = \begin{bmatrix} t_{11}^* & t_{12}^* \\ t_{21}^* & t_{22}^* \end{bmatrix} \tag{2.43}$$

$$\boldsymbol{U}^* = \begin{bmatrix} u_{11}^* & u_{12}^* \\ u_{21}^* & u_{22}^* \end{bmatrix} \tag{2.44}$$

where the subindices i and j of t_{ij} and u_{ij} are the resulting tractions and displacements, respectively, in j direction due to the application of a unitary force in i direction.

By disregarding the presence of the body forces and by discretizing the problem into N elements, Eq. (2.40) leads to the following:

$$C_{ij}\left(\mathbf{x'}\right) u_j\left(\mathbf{x'}\right) + \sum_{n=1}^{N} \int_{\Gamma_n} T_{ij}^*\left(\mathbf{x'}, \mathbf{x}\right) u_j(\mathbf{x}) d\Gamma = \sum_{n=1}^{N} \int_{\Gamma_n} U_{ij}^*\left(\mathbf{x'}, \mathbf{x}\right) t_j(\mathbf{x}) d\Gamma \tag{2.45}$$

where $\Gamma = \sum_{n=1}^{N} \Gamma_n$ and $C_{ij}(\mathbf{x}') = 1/2\delta_{ij}$.

After substituting the expressions given in Eq. (2.41) into the integral equation (2.45), one obtains

$$C_{ij}(\mathbf{x}') u_j(\mathbf{x}') + \sum_{n=1}^{N}\sum_{\alpha=1}^{m}[DH]_{ij}^{n\alpha} u_j^{n\alpha} = \sum_{n=1}^{N}\sum_{\alpha=1}^{m}[DG]_{ij}^{n\alpha} t_j^{n\alpha} \quad i,j = 1,2 \qquad (2.46)$$

where

$$
\begin{aligned}
[DH]_{ij}^{n\alpha} &= \int_{-1}^{1} N_\alpha(\xi) T_{ij}^*(\mathbf{x}', \mathbf{x}(\xi)) J^n(\xi) d\xi \\
[DG]_{ij}^{n\alpha} &= \int_{-1}^{1} N_\alpha(\xi) U_{ij}^*(\mathbf{x}', \mathbf{x}(\xi)) J^n(\xi) d\xi
\end{aligned}
\qquad (2.47)
$$

where the Jacobian of transformation $J(\xi)$ is given by:

$$J(\xi) = \sqrt{\left(\frac{dx_1}{d\xi}\right)^2 + \left(\frac{dx_2}{d\xi}\right)^2} \qquad (2.48)$$

From Eq. (2.46), a system of equations can be assembled for solving the problem:

$$[\boldsymbol{H}]\{\boldsymbol{u}\} = [\boldsymbol{G}]\{\boldsymbol{t}\} \qquad (2.49)$$

where the square matrix $[\boldsymbol{H}]$ contains all the influence terms associated to $T^*(\mathbf{x}',\mathbf{x})$ kernel and $[\boldsymbol{G}]$ of the $U^*(\mathbf{x}',\mathbf{x})$ one. Both are fully populated and non-symmetric matrices. The vectors $\{\boldsymbol{u}\}$ and $\{\boldsymbol{t}\}$ contain the nodal displacements and the tractions. After prescribing the boundary conditions, Eq. (2.18) is rearranged according to the following system:

$$[\boldsymbol{A}]\{\boldsymbol{x}\} = \{\boldsymbol{f}\} \qquad (2.50)$$

where $\{x\}$ corresponds to the vector of unknown degrees of freedom and $\mathbf{f}$ to the indepedent vector.

2.2.1   The Isogeometric Boundary Element Method (IGABEM)

Usually, in numerical analysis, Lagrangian polynomial functions are used to describe the geometry and unknown fields, while in CAD software, the geometries are most commonly described using the so-called Non-Uniform Rotational B-splines (NURBS). Consequently, there is a mismatch between these two tools. In contrast, the isogeometric analysis (IGA) uses the same functions used in CAD software, provinding thus a direct link between the CAD and the numerical analysis (SIMPSON *et al.*, 2012). Thus, in the IGABEM, the Lagrangian polynomials are replaced by the NURBS basis functions.

Figure 7 – Exemplification of the interpolatory property of the B-Spline function.
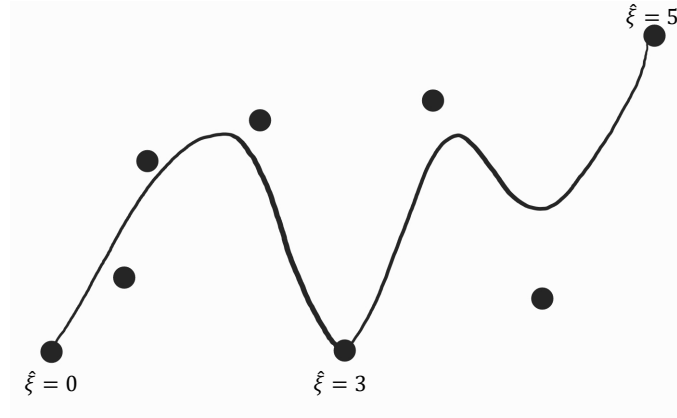
Source: Adapted from Beer, Smith and Duenser (2008).

Once the NURBS are built from the B-splines, their construction is first addressed. The primary distinction between the two lies in the fact that NURBS employ a projection technique on B-splines during assembly. This enables the creation of intricate geometries, as B-splines are parametric functions that can map curves within the geometric space.

In this sense, the following concepts herein described are based in Cottrell, Hughes and Bazilevs (2009), Simpson *et al.* (2012) and in Simpson *et al.* (2013). Thus, it is known that one of the most essential elements of such type of functions is the *knot vector*, which is a non-decreasing set of coordinates in the parametric space given by $\Xi = \{\xi_1, \xi_2, \ldots, \xi_{n+p+1}\}$, where i is the knot index, ξ_i is the ith knot, p is the polynomial order and n is the number of basis functions used to form the B-Spline curves. A knot vector is said to be open if its first and last knot values appear $p+1$ times. The number of basis functions is given by the number of control points, which are similar to the nodes in conventional BEM (Lagrangian). Also, the curve order p is equivalent to the degree of the polynomial used in the isoparametric formulation.

In the present work, the knot spans are considered elements once the numerical quadrature is carried out at the knot span level. If a knot is repeated k times, then the B-spline curve's continuity at the point is C^{p-k} and if the curve is C^0 continuous at a point, then the curve is interpolatory at this location. Figure 7 shows as an example such property for a knot vector $KV = [0,0,0,1,2,3,3,4,5,5,5]$ and $p = 2$, where the curve is interpolatory at $\xi = 3$ (C^0) and at the extremities with $\xi = 0$ and $\xi = 5$ (C^{-1}).

The parametrization of a B-spline curve in terms of its basis functions and control points $\mathbf{p}_a$ is given by:

$$\mathbf{c}(\xi) = \sum_{a=1}^{n} N_{a,p}(\xi)\mathbf{p}_a \tag{2.51}$$

where $\mathbf{c}(\xi)$ is a vector containing the Cartesian coordinates of the location described by the parametric coordinate ξ, and $N_{a,p}$ stands for the set of B-spline basis functions of degree p. The basis functions are defined recursively starting with piecewise constants for $p = 0$, with $1 \leqslant a \leqslant n$:

$$N_{a,0} = \begin{cases} 1 & \text{if } \xi_a \leqslant \xi < \xi_{a+1} \\ 0 & \text{otherwise} \end{cases} \tag{2.52}$$

For $p = 1, 2, 3...$, the recursive Cox-de Boor formula (COX, 1972; BOOR, 1972) is used:

$$N_{i,p}(\xi) = \frac{\xi - \xi_i}{\xi_{i+p} - \xi_i} N_{i,p-1}(\xi) + \frac{\xi_{i+p+1} - \xi}{\xi_{i+p+1} - \xi_{i+1}} N_{i+1,p-1}(\xi) \tag{2.53}$$

It is important to mention that the basis functions are non-negative at every point and they constitute a partition of unity, that is:

$$\sum_{i=1}^{n} N_{i,p}(\xi) = 1 \quad \forall \xi \tag{2.54}$$

The first-order derivatives of a B-spline function can be obtained through:

$$\frac{d}{d\xi} N_{i,p}(\xi) = \frac{p}{\xi_{i+p} - \xi_i} N_{i,p-1}(\xi) - \frac{p}{\xi_{i+p+1} - \xi_{i+1}} N_{i+1,p-1}(\xi) \tag{2.55}$$

While the B-splines only approximate circular shapes, the NURBS can reproduce their exact form (SIMPSON *et al.*, 2013). For that, such functions are generated from a projection of higher dimentional B-splines, and the additional coordinate is understood as a weight. The interpolation via NURBS is given by:

$$\mathbf{c}(\xi) = \sum_{a=1}^{n} R_{a,p}(\xi)\mathbf{p}_a \tag{2.56}$$

where

$$R_{a,p} = \frac{N_{a,p}(\xi)w_a}{\sum_{\hat{a}=1}^{m} N_{\hat{a},p}(\xi)w_{\hat{a}}} \tag{2.57}$$

Note that in the case where the weights are equal to one (i.e., $w_a = 1 \ \forall$a), Eq. (2.57) returns the B-spline functions.

The first-order derivatives of the NURBS are obtained by:

$$\frac{d}{d\xi} R_{a,p}(\xi) = w_a \frac{W(\xi)N'_{a,p} - W'(\xi)N_{a,p}(\xi)}{W(\xi)^2} \tag{2.58}$$

in which

$$W(\xi) = \sum_{\hat{a}=1}^{n} N_{\hat{a},p}(\xi) w_a, \tag{2.59}$$

$$N'_{a,p} \equiv \frac{d}{d\xi} N_{a,p} \tag{2.60}$$

and

$$W'(\xi) = \sum_{\hat{a}=1}^{n} N'_{\hat{a},p}(\xi) w_a. \tag{2.61}$$

For the numerical implementations, once the integration is carried out into the knot spans and not directly in the NURB, an additional transformation Jacobian must be considered. In a knot span $[\xi_1, \xi_2]$, for example, the parametric coordinate is defined according to:

$$\xi = \frac{(\xi_2 - \xi_1)\,\hat{\xi} + (\xi_2 + \xi_1)}{2} \tag{2.62}$$

where $\hat{\xi}$ is the Gauss coordinate. Hence, the Jacobian is given by:

$$\frac{\partial \xi}{\partial \hat{\xi}} = \frac{\xi_2 - \xi_1}{2} \tag{2.63}$$

An important difference between IGABEM and the conventional BEM that should be mentioned relies on the location of the collocation points. As not all the control points are on the boundary, the Greville abscissae (GREVILLE, 1964; JOHNSON, 2005) definition is used to overcome such a problem. For each control point, there is an associated collocation point. For the control points situated in each curve end, the collocation points should be discontinuous. For the remaining ones, the collocations can be positioned at the Greville abscissae, given by:

$$\xi'_a = \frac{\xi_{a+1} + \xi_{a+2} + \cdots + \xi_{a+p}}{p} \quad a = 1, 2, \ldots, n \tag{2.64}$$

where p is the curve order and n is the number of control points.

2.3 Singularity Subtraction - Regularization of Kernels U_{ij}^* and T_{ij}^*

The kernels U_{ij}^* and T_{ij}^* presented in Eq. (2.40) are singular when the source point $\mathbf{x}'$ is located on the boundary Γ. Regular numerical integration cannot be uniquely applied as the kernels are improper. Hence, in order to solve this problem, principles of integral regularization are applied, which consist in subtracting the singular part of the kernel

from the integral equation. For in deep detailes about the regularization process, see Kzam (2009).

In this sense, the first integral on the right-hand side of Eq. (2.40) can be written as:

$$\int_\Gamma U_{ij}^*\left(\mathbf{x}', \mathbf{x}\right) t_j(\mathbf{x}) d\Gamma = \int_\Gamma U_{ij}^*\left(\mathbf{x}', \mathbf{x}\right) t_j(\mathbf{x}) d\Gamma - \int_\Gamma \bar{U}_{ij}^*\left(\mathbf{x}', \mathbf{x}\right) t_j(\mathbf{x}) d\bar{\Gamma} + \int_\Gamma \bar{U}_{ij}^*\left(\mathbf{x}', \mathbf{x}\right) t_j(\mathbf{x}) d\bar{\Gamma}$$
(2.65)

in which,

$$\bar{U}_{ij}^*\left(\mathbf{x}', \mathbf{x}\right) = \frac{1}{8\pi G(1-v)}\left[-\left(3-4\nu\right)\ln\left(|r^*|\right)\delta_{ij}\right]$$
(2.66)

where $r^*\left(\xi_0, \xi\right) = J\left(\xi_0\right)|\xi - \xi_0|$, where ξ_0 is the parametric coordinate of the source point; ξ is the parametric coordinate of the field point and $J\left(\xi_0\right)$ is the Jacobian of the transformation evaluated at ξ_0. This relation comes from a Taylor series expansion of the field coordinates written in terms of the source coordinates. It is important to mention that the term $\frac{r_i r_j}{8\pi\mu(1-\nu)}$ presented in Eq. (B.10) is not considered in the regularization process, since it is not singular.

Thus, U_{ij}^* and $\bar{U}_{ij}^*$ present the same singularity intensity. The two first integrals in the right-hand side of Eq. (2.65) can be evaluated numerically, while the last one can be analytically solved, in the Principal Cauchy Value (PCV) sense. The numerical part is evaluated via Gauss-Legendre quadrature, according to:

$$\int_\Gamma U_{ij}^*\left(\mathbf{x}', \mathbf{x}\right) t_j(\mathbf{x}) d\Gamma - \int_\Gamma \bar{U}_{ij}^*\left(\mathbf{x}', \mathbf{x}\right) t_j(\mathbf{x}) d\Gamma =$$
$$\int_{-1}^{1} \frac{1}{8\pi(1-v)}\left[-(3-4v)\ln(r)\delta_{ij} + r_{,i}(\xi)r_{,j}(\xi)\right] J\left(\xi_0\right)\phi\left(\xi_0\right) d\xi$$
$$-\int_{-1}^{1} \frac{1}{8\pi(1-v)}\left[-(3-4v)\ln\left(|r^*|\right)\delta_{ij}\right] J\left(\xi_0\right)\phi\left(\xi_0\right) d\xi$$
(2.67)

where ϕ is the basis function. In sequence, the PCV is defined as:

$$PCV = \frac{-(3-4\nu)\delta_{ij}}{8\pi G(1-\nu)} J(\xi_0) \int_{-1}^{1} \ln(|r^*|) d\xi.$$
(2.68)

The above integral can be evaluated according to the following limit:

$$PCV = \lim_{\varepsilon\to 0}\left\{ \frac{-(3-4\nu)\,\delta_{ij} J\left(\xi_0\right)}{8\pi G(1-\nu)}\left[\int_{-1-\xi_0}^{-\xi}\ln\left(|J\left(\xi_0\right)\xi|\right) d\xi + \int_{\xi}^{1-\xi_0}\ln\left(|J(\xi_0)\xi|\right)\right) d\xi\right]\right\}$$
(2.69)

which results in:

$$PCV = \frac{-(3-4v)\delta_{ij}J(\xi_0)}{8\pi G(1-\nu)}\left[(1+\xi_0)\ln\left(|J(\xi_0)(1+\xi_0)|\right) + (1-\xi_0)\ln\left(|\,J(\xi_0)(1-\xi_0\,|)\right) - 2\right]$$
$$(2.70)$$

The above relationship is valid only when $\xi_0 \neq \pm 1$, i.e, only for discontinuous elements. Thus, for the remaining for cases where $\xi_0 = \pm 1$, the following expression is valid:

$$PCV = \frac{-(3-4v)\delta_{ij}J(\xi_0)}{8\pi G(1-\nu)}\left[2\ln\left(|2J(\xi_0)| - 2\right)\right] \qquad (2.71)$$

For eliminating the singularity present on the kernel T_{ij}^*, the same procedure is applied to the second integral of the right-hand side of Eq. (2.40), which can be rewritten in terms of:

$$\int_{\Gamma} T_{ij}^*\left(\mathbf{x}',\mathbf{x}\right)u_j(\mathbf{x})d\Gamma = \int_{\Gamma} T_{ij}^*\left(\mathbf{x}',\mathbf{x}\right)u_j(\mathbf{x})d\Gamma - \int_{\Gamma} \bar{T}_{ij}^*\left(\mathbf{x}',\mathbf{x}\right)u_j(\mathbf{x})d\bar{\Gamma} + \int_{\Gamma} \bar{T}_{ij}^*\left(\mathbf{x}',\mathbf{x}\right)u_j(\mathbf{x})d\bar{\Gamma}$$
$$(2.72)$$

Similarly, Tij^* and $\bar{T}ij^*$ exhibit the same level of singularity intensity. The first two integrals on the right-hand side of Eq. (2.72) can be numerically evaluated using Gauss-Legendre quadrature, as outlined below:

$$\int_{\Gamma} T_{ij}^*\left(\mathbf{x}',\mathbf{x}\right)u_j(\mathbf{x})d\Gamma - \int_{\Gamma} \bar{T}_{ij}^*\left(\mathbf{x}',\mathbf{x}\right)u_j(\mathbf{x})d\Gamma =$$
$$\int_{-1}^{1} \frac{-1}{4\pi(1-v)r}\left\{\frac{\partial r}{\partial n}\left[(1-2v)\delta_{ij} + 2r_{,i}r_{,j}\right] + (1-2v)\left(n_i r_{,j} - n_j r_{,i}\right)\right\} J(\xi_0)\phi(\xi_0)d\xi$$
$$-\int_{-1}^{1} \frac{-1}{4\pi(1-v)r^*}\left[(1-2v)\left(n_i(\xi_0)r_{,j}^* - n_j(\xi_0)r_{,i}^*\right)\right] J(\xi_0)\phi(\xi_0)d\xi$$
$$(2.73)$$

The term $\frac{1}{r}\frac{\partial r}{\partial n}$ is not singular, thereby it is not considered in the regularization process. The PCV of the second integral of the right-hand side of Eq. (2.72) is defined as:

$$PCV = \lim_{\xi \to 0}\left\{-\frac{\left[(1-2v)\left(n_i(\xi_0)r_{,j}^* - n_j(\xi_0)r_{,i}^*\right)\right]}{4\pi(1-v)}\left[\int_{-1-\xi_0}^{-\xi}\frac{1}{\xi}d\xi + \int_{\xi}^{1-\xi_0}\frac{1}{\xi}d\xi\right]\right\} \qquad (2.74)$$

limit that results in:

$$PCV = \frac{-\left[(1-2v)\left(n_i(\xi_0)r_{,j}^* - n_j(\xi_0)r_{,i}^*\right)\right]}{4\pi(1-v)}\left[\ln(1-\xi_0) - \ln(1+\xi_0)\right] \qquad (2.75)$$

Once again, this relationship holds true exclusively when $\xi_0 \neq \pm 1$. Therefore, for instances where this equality is satisfied, the following expression can be applied:

$$
\begin{aligned}
PCV &= \frac{-\left[(1-2v)\left(n_i\left(\xi_0\right)r_{,j}^* - n_j\left(\xi_0\right)r_{,i}^*\right)\right]}{4\pi(1-v)}\ln(2) \text{ if } \xi_0 = -1 \\
PCV &= \frac{-\left[(1-2v)\left(n_i\left(\xi_0\right)r_{,j}^* - n_j\left(\xi_0\right)r_{,i}^*\right)\right]}{4\pi(1-v)}\ln(-2) \text{ if } \xi_0 = 1
\end{aligned}
\tag{2.76}
$$

2.4   Knot Insertion: h-refinement

Refinement of NURBS may be necessary or desired in certain situations. For instance, the most common reason is to better represent the underlying geometry. Notwithstanding, it can be required to achieve higher levels of accuracy in numerical analysis: in nonlinear problems such as damage analysis, NURBS refinement can be necessary to achieve higher levels of accuracy in predicting the behaviour of the damaged structure. According to Piegl and Tiller (1996), numerous strategies can be employed to enhance the precision and adaptability of the NURBS representation of a surface or curve, such as knot insertion, knot removal, degree elevation, degree reduction, and others. In this work, the knot insertion technique is utilized, which is a type of h-refinement. It involves increasing the total number of elements (knot spans in the case of IGABEM) without changing the order of interpolation functions. New control points are then introduced, and the weights of existing control points are adjusted.

In this sense, consider the following generic knot vector $\Xi = \{\xi_1, \xi_2, \ldots, \xi_{n+p+1}\}$ where $\bar{\xi} \in [\xi_a, \xi_{a+1}[$ is the desired new knot. The new knot vector is then given by $\bar{\Xi} = \left\{\xi_1, \xi_2, \ldots, \xi_a, \bar{\xi}, \xi_{a+1}, \ldots \xi_{n+p+1}\right\}$ and the rational basis functions relative to the new knot span are constructed according to the conventional way presented in Eq. (2.57). The relationship for defining the new coordinates (x_i, y_i) and weights w_i of control points can be found in Piegl and Tiller (1996), which are presented as follows:

$$
\mathbf{Q}_i = \alpha_i \mathbf{P}_i + (1 - \alpha_i)\mathbf{P}_{i-1}
\tag{2.77}
$$

where $\mathbf{Q}_i = (\bar{x}_i w_i, \bar{y}_i w_i, w_i)$ are the new coordinates of control point i and $\mathbf{P}_i = (x_i w_i, y_i w_i, w_i)$ are the coordinates of the existing control point i. The coefficient α_i is given by:

$$
\alpha_i = \begin{cases} 1, & 1 \leq i \leq a - p \\ \frac{\bar{\xi} - \xi_i}{\xi_{i+p} - \xi_i}, & a - p + 1 \leq i \leq a \\ 0, & i \geq a + 1 \end{cases}
\tag{2.78}
$$

Figure 8 – Multi-regions.
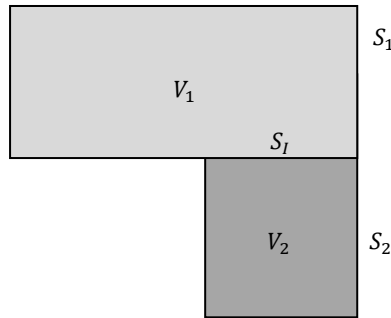
Source: Adapted from Aliabadi (2002).

2.5 Subregion Technique

Non-homogenous structures can be characterized by the presence of more than one region. The integral formulation presented herein can be applied to such problem types. For this, each homogenous portion is individually moldeled and then compatibility of displacements and equilibrium of tractions are imposed along the materials interface. Consider a domain V assembled by two different materials, as shown in Figure 8, where V_1 and V_2 are two different subregions of the domain which have boundaries S_1 and S_2 and are connected by an interface S_I.

The nodal displacements and tractions at the external boundary S_1 is defined by $\boldsymbol{U}^1$ and $\boldsymbol{T}^1$, respectively; similarly, $\boldsymbol{U}^2$ and $\boldsymbol{T}^2$ are defined for boundary S_2 and $\boldsymbol{U}_I^1$, $\boldsymbol{U}_I^2$, $\boldsymbol{T}_I^1$ and $\boldsymbol{T}_I^2$ are displacements and tractions at the interface S_I. Thus, the system of equations for the subregion V_1 can be written as:

$$\begin{bmatrix} \mathbf{H}^1 & \mathbf{H}_I^1 \end{bmatrix} \left\{ \begin{array}{c} \mathbf{U}^1 \\ \mathbf{U}_I^1 \end{array} \right\} = \begin{bmatrix} \mathbf{G}^1 & \mathbf{G}_I^1 \end{bmatrix} \left\{ \begin{array}{c} \mathbf{T}^1 \\ \mathbf{T}_I^1 \end{array} \right\} \tag{2.79}$$

Similarly for V_2, there is:

$$\begin{bmatrix} \mathbf{H}^2 & \mathbf{H}_I^2 \end{bmatrix} \left\{ \begin{array}{c} \mathbf{U}^2 \\ \mathbf{U}^2 \end{array} \right\} = \begin{bmatrix} \mathbf{G}^2 & \mathbf{G}_I^2 \end{bmatrix} \left\{ \begin{array}{c} \mathbf{T}^2 \\ \mathbf{T}_I^2 \end{array} \right\} \tag{2.80}$$

The compatibility and the equilibrium conditions at the interface S_I are

$$\begin{aligned} \mathbf{U}_I^1 &= +\mathbf{U}_I^2 \equiv \mathbf{U}_I \\ \mathbf{T}_I^1 &= -\mathbf{T}_I^2 \equiv \mathbf{T}_I \end{aligned} \tag{2.81}$$

Combining Eq. (2.79) to Eq. (2.80) and applying the relations shown in (2.81), the following expression is obtained:

$$
\begin{bmatrix}
\mathbf{H}^1 & \mathbf{H}^1_I & 0 & 0 \\
0 & 0 & \mathbf{H}^2 & \mathbf{H}^2_I \\
0 & 1 & 0 & -1 \\
0 & 0 & 0 & 0
\end{bmatrix}
\begin{Bmatrix}
\mathbf{U}^1 \\
\mathbf{U}^1_I \\
\mathbf{U}^2 \\
\mathbf{U}^2_I
\end{Bmatrix}
=
\begin{bmatrix}
\mathbf{G}^1 & \mathbf{G}^1_I & 0 & 0 \\
0 & 0 & \mathbf{G}^2 & \mathbf{G}^2_I \\
0 & 0 & 0 & 0 \\
0 & 1 & 0 & 1
\end{bmatrix}
\begin{Bmatrix}
\mathbf{T}^1 \\
\mathbf{T}^1_I \\
\mathbf{T}^2 \\
\mathbf{T}^2_I
\end{Bmatrix}
\tag{2.82}
$$

Rearranging the given system in terms of U_I and T_I, one gets

$$
\begin{bmatrix}
\mathbf{H}^1 & \mathbf{H}^1_I & -\mathbf{G}^1_I & 0 \\
0 & \mathbf{H}^2_I & -\mathbf{G}^2_I & \mathbf{H}^2
\end{bmatrix}
\begin{Bmatrix}
\mathbf{U}^1 \\
\mathbf{U}_I \\
\mathbf{T}_I \\
\mathbf{U}^2
\end{Bmatrix}
=
\begin{bmatrix}
\mathbf{G}^1 & 0 \\
0 & \mathbf{G}^2
\end{bmatrix}
\begin{Bmatrix}
\mathbf{T}^1 \\
\mathbf{T}^2
\end{Bmatrix}
\tag{2.83}
$$

Hence, after applying the boundary conditions, the resulting system of equations is given by

$$
\begin{bmatrix}
\mathbf{A}^1 & \mathbf{H}^1_I & -\mathbf{G}^1_I & 0 \\
0 & -\mathbf{H}^2_I & -\mathbf{G}^2_I & \mathbf{A}^2
\end{bmatrix}
\begin{Bmatrix}
\mathbf{X}^1 \\
\mathbf{U}_{12} \\
\mathbf{T}_{12} \\
\mathbf{X}^2
\end{Bmatrix}
=
\begin{Bmatrix}
\mathbf{f}^1 \\
\mathbf{f}^2
\end{Bmatrix}
\tag{2.84}
$$

where $\mathbf{f}^1$ and $\mathbf{f}^2$ are vectors that raise from prescribed values from boundaries S_1 and S_2.

3 BEM SOLUTION STRATEGIES FOR NONLINEAR PROBLEMS

This chapter addresses a manner for handling physical nonlinear problems through the BEM. According to Brebbia, Telles and Wrobel (2012), the first publication involving such type of problem was presented by Swedlow and Cruse (1971), where a generalization of the strain hardening elastoplastic constitutive equations was carried out. Thereafter, Riccardella (1973) implemented the Von Mises yield criterion (isotropic hardening) for two-dimensional problems by means of piece-wise constant interpolation for the plastic strains. Around the same period, Mendelson (1973) presented different integral formulations for elastoplastic problems. In 1975, this work was extended to a torsion problem of a bar involving the deformation theory of plasticity. Two years later, Mukherjee (1977) gave modified versions for the kernels of the plastic strain integral. Another important work came out by Telles and Brebbia (1979), in which the complete boundary element formulation for three- and two-dimensional plasticity problems were presented. Already in the 80s, willing to solve elastoplastic problems in two dimensions, Telles and Brebbia (1981) presented an *"initial strain"* form of the inelastic term along with a formulation that handled incompressible plastic strains using the isotropic von Mises yield criterion with strain hardening, ideal plasticity, and strain softening behaviour.

Different nonlinear material behaviours are of concern as well. For instance, it is known that problems where the formation of micro-cracks results in the loss of strength and rigidity of the structural members can be addressed by damage mechanics. However, so far, only limited applications of BEM to damage mechanics have been reported in the literature. Works from Herding and Kuhn (1996), Garcia, Florez-Lopez and Cerrolaza (1999), Botta, Venturini and Benallal (2005), Junior (2011) and Li *et al.* (2023) can be mentioned as examples.

Thus, with the aim to treat nonlinear damage mechanics problems, the following sections present the BEM formulation considering initial fields as well as a form of domain discretization via cells. The discretization using cell elements is a technique employed in the literature to address nonlinear effects, as they are mathematically represented by domain integrals, requiring the generation of a domain mesh (TELLES; BREBBIA, 1979; BOTTA; VENTURINI; BENALLAL, 2005; RIBEIRO; BEER; DÜNSER, 2008; TELLES, 2012; BEER *et al.*, 2016; BEER; DUENSER, 2023).

3.1 Integral Representations and the BEM for Problems with Initial Fields

Following Botta (2003), initial strain or stress fields are notary essential in problems where domain variables are indispensable to the description of the mechanical problem. For materials with nonlinear behavior, the incremental procedure for solving the problem

makes use of such a technique. Therefore, the components of the strain tensor in the source $\mathbf{x}'$ point are given by:

$$\varepsilon_{ij}(\mathbf{x}') = \varepsilon_{ij}^{e}(\mathbf{x}') + \varepsilon_{ij}^{0}(\mathbf{x}') \tag{3.1}$$

where ε^{e} is the elastic strain tensor and ε^{0} is the initial one. Similarly, the components of the stress tensor are decomposed as

$$\sigma_{ij}(\mathbf{x}') = \sigma_{ij}^{e}(\mathbf{x}') + \sigma_{ij}^{0}(\mathbf{x}') \tag{3.2}$$

In this way, Eq. (A.6) can be rewritten as:

$$\sigma_{ij}(\mathbf{x}') = \lambda\delta_{ij}\left[\varepsilon_{kk}(\mathbf{x}') - \varepsilon_{ll}^{0}(\mathbf{x}')\right] + 2\mu\left[\varepsilon_{ij}(\mathbf{x}') - \varepsilon_{ij}^{0}(\mathbf{x}')\right] \tag{3.3}$$

or, similar to the expression given in Eq. (B.1), in terms of displacements the relationship is expressed as:

$$\sigma_{ij}(\mathbf{x}') = \lambda u_{l,l}(\mathbf{x}')\delta_{ij} + \mu\left[u_{i,j}(\mathbf{x}') + u_{j,i}(\mathbf{x}')\right] - \lambda\varepsilon_{kk}^{0}(\mathbf{x}')\delta_{ij} - 2\mu\varepsilon_{ij}^{0}(\mathbf{x}') \tag{3.4}$$

Hence, with the same Kelvin's fundamental solution, the integral equation of the elastic problem is increased by an integral with initial stress terms, i.e.:

$$
\begin{aligned}
\frac{1}{2}u_i(\mathbf{x}') + \int_{\Gamma} T_{ij}^*(\mathbf{x}',\mathbf{x})\,u_j(\mathbf{x})d\Gamma &= \int_{\Gamma} U_{ij}^*(\mathbf{x}',\mathbf{x})\,t_j(\mathbf{x})d\Gamma + \int_{\Omega} U_{ij}^*(\mathbf{x}',\mathbf{x})\,b_j(\mathbf{x})d\Omega \\
&+ \int_{\Omega}\varepsilon_{ijk}^*(\mathbf{x}',\mathbf{x})\sigma_{jk}^{0}(\mathbf{x})d\Omega
\end{aligned}
\tag{3.5}
$$

where the fundamental solution for strains, which can be derived from the fundamental solution of displacements, $\varepsilon_{ijk}^*(\mathbf{x}',\mathbf{x})$, is given by:

$$\varepsilon_{ijk}^*(\mathbf{x}',\mathbf{x}) = \frac{-1}{8\pi(1-v)\mu r}\left[(1-2\nu)\left(r_{,k}\delta_{ij} + r_{,j}\delta_{ik}\right) - r_{,i}\delta_{jk} + 2r_{,i}r_{,j}r_{,k}\right] \tag{3.6}$$

In Eq. (3.5), the term $\sigma_{jk}^{0}(\mathbf{x})$ refers to the initial stress tensor, which depends on the adopted constitutive model (PEIXOTO; RIBEIRO; PITANGUEIRA, 2018). The nonlinear equilibrium equation is general for any nonlinear constitutive law. This makes the formulation unique and applicable to a wide range of nonlinear models (BOTTA, 2003). In this work, the Extended Lumped Damage Model is adopted, where a comprehensive explanation is given in Chapter 4.

3.2 Algebraic Equations for Problems with Initial Fields

For the sake of simplicity, the body forces from this point on will be disregarded. Hence, in the discretized form, Somigliana's identity equals an algebraic equation as shown below:

$$[\mathbf{H}]\{\mathbf{u}\} = [\mathbf{G}]\{\mathbf{t}\} + [\mathbf{Q}]\{\sigma^{\mathbf{0}}\} \tag{3.7}$$

where $[\mathbf{H}]$, $[\mathbf{G}]$ and $[\mathbf{Q}]$ are fully populated and nonsymmetric matrices with the influence terms arising from the integration of T_{ij}^*, U_{ij}^* and ε_{ijk}^*, respectively; $\{\mathbf{u}\}$, $\{\mathbf{t}\}$ and $\{\sigma^{\mathbf{0}}\}$ are the vectors with the nodal displacements, the tractions and the domain initial stresses, respectively. Therefore, still following Botta (2003) and considering the relations given in Venturini and Brebbia (1984), for a known initial stress field $\{\sigma^{\mathbf{0}}\}$ applied into the domain, the displacement and traction fields on the boundary can be obtained through Eq. (3.7).

For computing the internal displacements, as the source point is inside the domain, the displacement and traction kernels are nonsingular. Thus, the internal displacements $\{\mathbf{u}\}_{int}$ are obtained via:

$$\{\mathbf{u}\}_{int} = -[\mathbf{H}]'\{\mathbf{u}\} + [\mathbf{G}]'\{\mathbf{t}\} + [\mathbf{Q}]'\{\sigma^{\mathbf{0}}\} \tag{3.8}$$

The method proposed by Venturini and Brebbia (1984) offers a means to transform the algebraic systems outlined in Eqs. (3.7) and (3.8) into a more convenient form. This transformation is particularly advantageous for implementing the initial stress field required in nonlinear analysis. The authors reorganize the terms considering the stress integral equation for internal points. In this study, where the adopted constitutive model is the Extended Lumped Damage Model (XLDM), we suggest a similar approach. Instead of using the stress integral equation for internal points, the displacement integral equation for internal points is considered, aligning with the nature of the chosen model. The XLDM incorporates nonlinear effects by considering the increase in band thickness, an effect that is indirectly influenced by the displacement field. Further details are presented in Chapter 4.

Hence, by rearranging the terms from Eq. (3.7), where all unknowns are left on the left-hand side, one obtains:

$$[\mathbf{A}]\{\mathbf{x}\} = \{\mathbf{f}\} + [\mathbf{Q}]\{\sigma^{\mathbf{0}}\} \tag{3.9}$$

After multiplying both sides of the above relation by the inverse of the matrix $[\mathbf{A}]$, the following equation is obtained:

$$\{\mathbf{x}\} = [\mathbf{R}]\{\sigma^\mathbf{0}\} + \{\mathbf{m}\} \tag{3.10}$$

where

$$[\mathbf{R}] = [\mathbf{A}]^{-\mathbf{1}}[\mathbf{Q}]$$
$$\{\mathbf{m}\} = [\mathbf{A}]^{-1}\{\mathbf{f}\} \tag{3.11}$$

In a similar way, Eq. (3.8) can be rewritten as:

$$\{\mathbf{u}\}_{int} = -[\mathbf{A}]'\{\mathbf{x}\} + \{\mathbf{f}\}' + [\mathbf{Q}]'\{\sigma^\mathbf{0}\} \tag{3.12}$$

that can be rearrenged according to:

$$\{\mathbf{u}\}_{int} = [\mathbf{S}]\{\sigma^\mathbf{0}\} + \{\mathbf{n}\} \tag{3.13}$$

where

$$[\mathbf{S}] = [\mathbf{Q}]' - [\mathbf{A}]'[\mathbf{R}]$$
$$\{\mathbf{n}\} = \{\mathbf{f}\}' - [\mathbf{A}]'\{\mathbf{m}\} \tag{3.14}$$

As pointed out by Venturini and Brebbia (1984), the vectors $\{\mathbf{m}\}$ and $\{\mathbf{n}\}$ represent the elastic solution resulting from the application of any prescribed load or displacement on the boundary. In the same way, the nonlinear effects are represented by the matrices $[\mathbf{R}]$ and $[\mathbf{S}]$. These matrices are used in the iterative solution technique to model nonlinear responses.

Considering all the above relations, a predictor-corrector algorithm can be implemented. In the predictor stage, the nonlinear effects are assumed to be null. However, before introducing the predictor algorithm, it is necessary to introduce domain discretization via cells, since the nonlinear effects due to the application of $\{\sigma^\mathbf{0}\}$ are represented by a domain integral, as previously presented in Eq. 3.5. This is the subject of the next section.

3.3 Domain Discretization via Cells

There are several methodologies for treating domain integrals in BEM. For instance, when the fields are known, which is the case of constat body forces, the effect of the domain integral can be transformed into a boundary one, as shown in Appendix C. In the case of nonlinear problems, the initial stress field is initially unknown and vary along the structural domain. Works from Venturini and Brebbia (1984), Barbirato *et al.* (1999), Botta (2003), Junior (2006), Peixoto (2016) are examples where the domain is discretized into cells. The effects resulting from the application of $\{\sigma^\mathbf{0}\}$ are captured through this discretization process.

Figure 9 – Domain discretization into cells and the corresponding coordinates mapping to the bivariate parametric space.
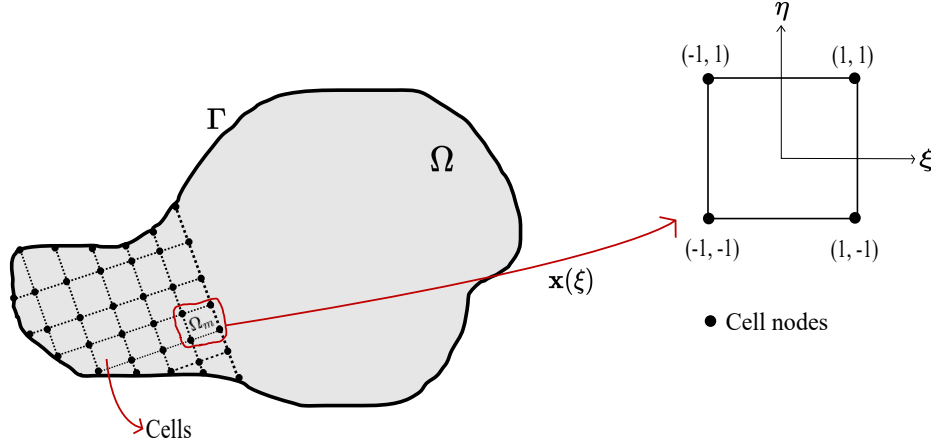
Source: The author.

The domain Ω is discretized into M cells of Ω_m domain, as shown in Figure (9). In two-dimensional problems, such Ω_m domains are plane surfaces. In this work, linear quadrilateral elements are considered, as illustrated in Figure (9) as well.

The adopted bivariate shape functions for the quadratic elements are linear bivariate Lagrangian polynomials, according to the following:

$$
\begin{aligned}
N_1(\xi, \eta) &= \frac{1-\xi}{2}\frac{1-\eta}{2} \\
N_2(\xi, \eta) &= \frac{1+\xi}{2}\frac{1-\eta}{2} \\
N_3(\xi, \eta) &= \frac{1+\xi}{2}\frac{1+\eta}{2} \\
N_4(\xi, \eta) &= \frac{1-\xi}{2}\frac{1+\eta}{2}
\end{aligned}
\tag{3.15}
$$

Note that with such sequence the functions assume a unity value at its own node and zero on the others, respecting the Kronecker delta property, as shown in Figure (10). Once the shape functions are known, the geometry of each cell can be approximated by the following interpolation:

$$
\mathbf{x} = \sum_{i=1}^{4} N_i(\xi, \eta)\mathbf{x}_i
\tag{3.16}
$$

where $\mathbf{x}_i$ refers to the x_i and y_i coordinates for each local node of the quadrilateral element.

The bivariate first order derivatives with respect to ξ of the shape functions given in Eq. (3.15) are defined by:

Figure 10 – Bivariate shape function evaluated at node 1.
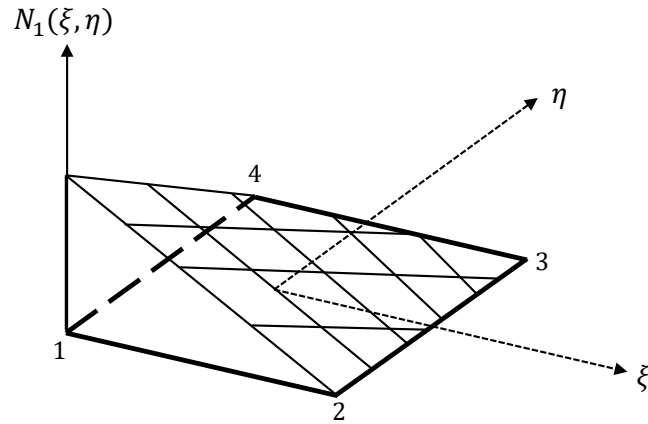
Source: Adapted from Beer, Smith and Duenser (2008).

$$\frac{\partial N_1}{\partial \xi} = \frac{-1}{4} + \frac{\eta}{4}$$
$$\frac{\partial N_2}{\partial \xi} = \frac{1}{4} - \frac{\eta}{4}$$
$$\frac{\partial N_3}{\partial \xi} = \frac{1}{4} + \frac{\eta}{4} \qquad (3.17)$$
$$\frac{\partial N_4}{\partial \xi} = -\frac{1}{4} - \frac{\eta}{4}$$

Deriving the same shape functions now with respect to η, one obtains:

$$\frac{\partial N_1}{\partial \eta} = \frac{-1}{4} + \frac{\xi}{4}$$
$$\frac{\partial N_2}{\partial \eta} = -\frac{1}{4} - \frac{\xi}{4}$$
$$\frac{\partial N_3}{\partial \eta} = \frac{1}{4} + \frac{\xi}{4} \qquad (3.18)$$
$$\frac{\partial N_4}{\partial \eta} = \frac{1}{4} - \frac{\xi}{4}$$

With the first-order derivatives, the Jacobian of transformation for the bivariate space can be obtained through the following:

$$J = J_\xi J_\eta \qquad (3.19)$$

where $J_\xi = \partial \mathbf{x}/\xi$ and $J_\eta = \partial \mathbf{x}/\eta$.

Finally, to account for the initial stress field effects, the domain integral with the new kernel $\varepsilon_{ijk}^*(\mathbf{x}', \mathbf{x})$ given in Eq. (3.6) is approximated by:

$$\int_\Omega \varepsilon_{ijk}^* \left(\mathbf{x}', \mathbf{x}\right) \sigma_{jk}^0(\mathbf{x}) \mathrm{d}\Omega = \sum_{m=1}^M \int_{\Omega_m} \varepsilon_{ijk}^* \left(\mathbf{x}', \mathbf{x}\right) \sigma_{jk}^0(\mathbf{x}) \mathrm{d}\Omega_m \qquad (3.20)$$

As mentioned in Aliabadi (2002), the kernel $\varepsilon_{ijk}^*(\mathbf{x}', \mathbf{x})$ exhibits a weakly singular or nearly singular behavior, depending on the position of the collocation point under analysis. The nearly singular case arises when the collocation point does not lie on the integration cell. In contrast, a weakly singular case occurs when the collocation point lies on a cell node, as the kernel contains a singularity of order 1 for 2D problems. Therefore, these circumstances imply that the integral given in Eq. (3.20) is improper, and additional techniques for eliminating the singularity become necessary. The techniques adopted in this work are addressed in the subsequent subsection.

3.4 Numerical Integration for Weakly and Nearly Singular Domain Integrals

Based on the nature of the kernel and the collocation point's relative position within the cell, integrals can exhibit nearly, weakly, or strongly singular behavior. In this study, the first and the second are of concern. These are defined by Aliabadi (2002) as follows:

- Nearly singular: the collocation node does not lie on the integration cell. Consequently, the integrands exhibit sharp variations as the source point approaches the integration cell. These integrals can be computed using standard Gauss quadrature with a cell subdivision technique.

- Weakly singular: these integrals are defined by a singular kernel of order $1/r$, where the collocation node lies on the integration cell. The integrals can be approximated by employing a variable transformation technique in order to cancel the singularity.

In this sense, for illustrative purposes, consider a hypothetical rectangular region with boundary Γ and domain Ω, as shown in Figure 11. 4 linear NURBS, totalling 12 control points are used to discretize the problem. The nonlinear effects are approximated by only a single cell of domain Ω_m. The control points are shown in grey and cell nodes in black. Control points $2, 3, 8$ and 9 coincide with cell nodes a, b, c and d. Thus, a weakly singular behavior is observed for these collocation points, as they lie on the cell nodes. The remaining ones exhibit a nearly singular behavior.

The transformation technique adopted herein for eliminating the singular behavior is a change of variables to polar coordinates. The works from Botta (2003) and Cordeiro (2018) are examples where this technique is employed. Through this transformation, the singularity $1/r$ is canceled by the appearence of a new jacobian of transformation ρ. All

Figure 11 – Hypothetical retangular element, its colocation points and the corresponding cell.
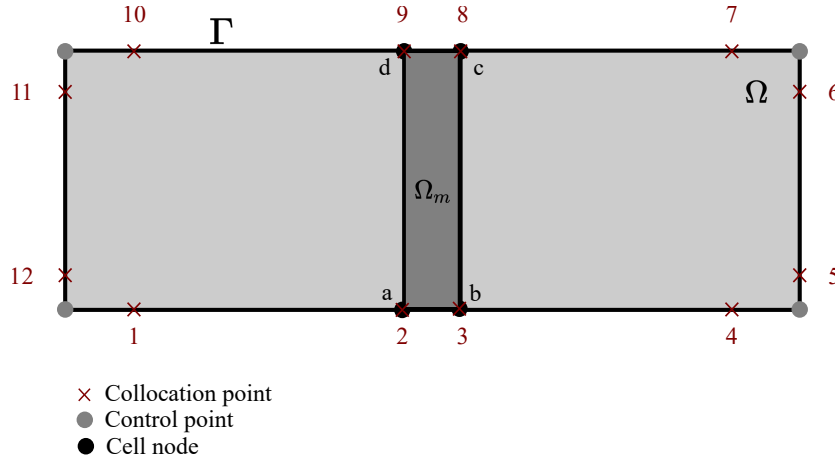
Source: The author.

the subsequent approaches are adapted from Cordeiro (2018). Hence, the integral which contains the kernel $\varepsilon_{\text{ijk}}^*(\mathbf{x}', \mathbf{x})$ given in Eq. (3.6) is expressed in the parametric as:

$$\int_\Omega \varepsilon_{ijk}^* \left(\mathbf{x}', \mathbf{x}(\xi, \eta)\right) \sigma_{\text{jk}}^0(\mathbf{x}) d\Omega = \int_{-1}^{1} \int_{-1}^{1} \varepsilon_{ijk}^* \left(\mathbf{x}', \mathbf{x}(\xi, \eta)\right) \phi_l(\mathbf{x}(\xi, \eta)) J(\xi, \eta) \sigma_{\text{jk}}^0 d\xi d\eta \quad (3.21)$$

where $J(\xi, \eta)$ is the Jacobian of transformation from the physical to the bivariate space, $\phi_l(\mathbf{x}(\xi, \eta))$ is the shape function related to node l, and $\sigma_{\text{jk}}^0(\mathbf{x})^l$ is the initial stress field at the node l.

Expressing coordinates in the parametric space is also possible by means of polar coordinates ρ and θ. As illustrated in Figure 12, the transformation from Cartesian parametric coordinates to polar coordinates can be described by:

$$\left\{ \begin{array}{c} \xi \\ \eta \end{array} \right\} = \left\{ \begin{array}{c} \rho \cos(\theta) \\ \rho \sin(\theta) \end{array} \right\} + \left\{ \begin{array}{c} \xi_0 \\ \eta_0 \end{array} \right\} \quad (3.22)$$

Hence, the relationships between the differentials of area are expressed as $d\xi d\eta = \rho d\rho d\theta$, where ρ represents the scalar Jacobian of the transformation. Once the relationships between the differentials of area from the physical space to Cartesian parametric coordinates and from the latter to parametric space with polar coordinates are established, the integral presented in Equation (3.21) can be reformulated as follows:

$$\int_\Omega \varepsilon_{ijk}^* \left(\mathbf{x}', \mathbf{x}(\xi, \eta)\right) \sigma_{\text{jk}}^0(\mathbf{x}) d\Omega = \int_{\theta_i}^{\theta_f} \int_0^{\hat{\rho}(\theta)} \varepsilon_{ijk}^* \left(\mathbf{x}', \mathbf{x}(\xi, \eta)\right) \phi_l(\mathbf{x}(\xi, \eta)) J(\xi, \eta) \sigma_{\text{jk}}^0 \rho d\rho d\theta \quad (3.23)$$

in which $\hat{\rho}(\theta)$ is a distance from a point to a line, which corresponds to the maximum value of ρ for a given θ and θ_i and θ_f are the initial and final angles, respectively.

Figure 12 – Parametric space of a retangular element in polar coordinates ρ and θ.
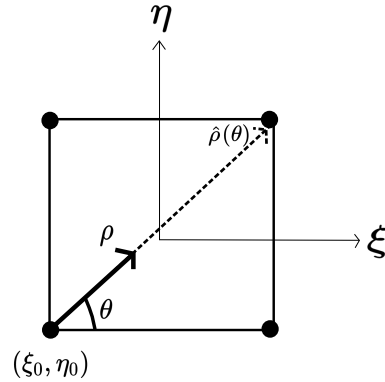
Source: The author.

Figure 13 – Polar coordinates mapped to an auxiliary parametric space $\xi^* \times \eta^*$.
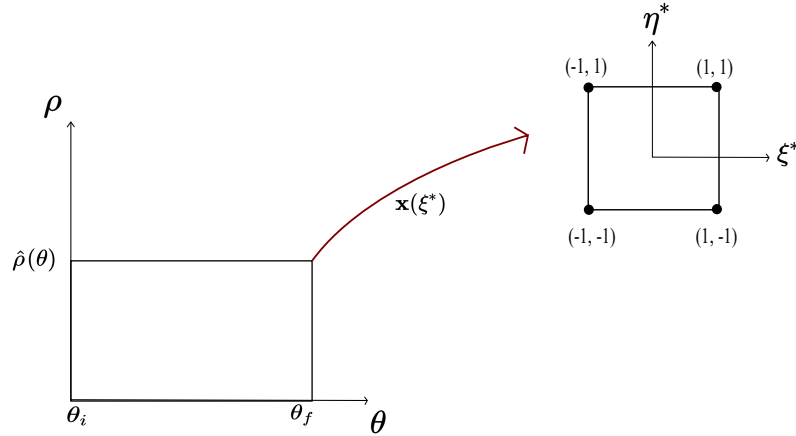
Source: The author.

In order to proceed with standard Gauss quadrature, the polar coordinates can be related to auxiliary parametric coordinates denoted as ξ^* and η^* (see Figure 13), as follows:

$$\rho = \frac{\eta^* \hat{\rho}(\theta)}{2} + \frac{\hat{\rho}(\theta)}{2} \tag{3.24}$$

$$\theta = \xi^* \left(\frac{\theta_f - \theta_i}{2} \right) + \left(\frac{\theta_f + \theta_i}{2} \right) \tag{3.25}$$

The differentials $d\rho$ and $d\theta$ can be calculated as:

$$d\rho = \frac{\xi^* \hat{\rho}(\theta)}{2} \tag{3.26}$$

Figure 14 – Values of θ_i and θ_f for cases where the collocation point is located on a corner.
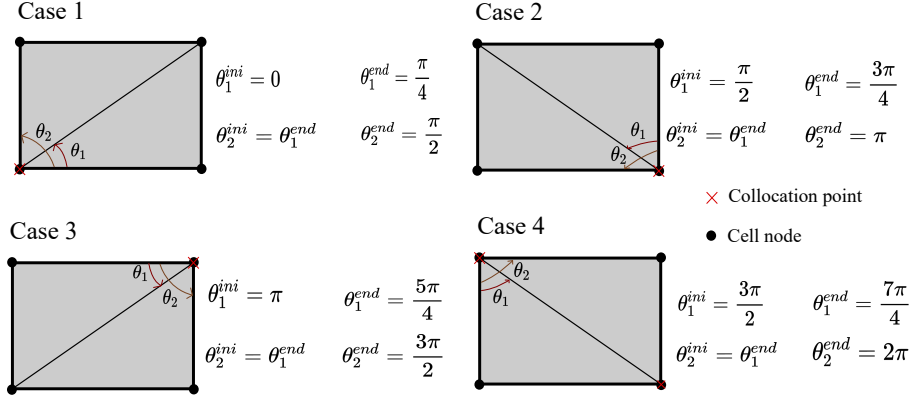
Source: The author.

$$dθ = \frac{\eta^* \pi}{4} \tag{3.27}$$

The integral presented in Eq. (3.23) can be rewritten in terms of the auxiliary parametric coordinates as:

$$\int_\Omega \varepsilon_{ijk}^* \left(\mathbf{x}', \mathbf{x}(\xi, \eta) \right) \sigma_{jk}^0(\mathbf{x}) d\Omega$$
$$= \int_{-1}^1 \int_{-1}^1 \varepsilon_{ijk}^* \left(\mathbf{x}', \mathbf{x} \left(\xi^*, \eta^* \right) \right) \phi_l \left(\xi \left(\xi^*, \eta^* \right), \eta \left(\xi^*, \eta^* \right) \right) J \left(\xi \left(\xi^*, \eta^* \right), \eta \left(\xi^*, \eta^* \right) \right) \sigma_{jk}^0 \rho d\rho d\theta \tag{3.28}$$

Numerically, the above integral can be approximated by:

$$\int_{-1}^1 \int_{-1}^1 \varepsilon_{ijk}^* \left(\mathbf{x}', \mathbf{x} \left(\xi^*, \eta^* \right) \right) \phi_l \left(\xi \left(\xi^*, \eta^* \right), \eta \left(\xi^*, \eta^* \right) \right) J \left(\xi \left(\xi^*, \eta^* \right), \eta \left(\xi^*, \eta^* \right) \right) \sigma_{jk}^0 \rho d\rho d\theta =$$
$$\sum_{i=1}^{NG\xi^*} \sum_{j=1}^{NG\eta\eta^*} \varepsilon_{ijk}^* \left(\mathbf{x}', \mathbf{x} \left(\xi^*, \eta^* \right) \right) \phi_l \left(\xi^*, \eta^* \right) J \left(\xi^*, \eta^* \right) \left(\frac{\theta_f - \theta_i}{4} \frac{\hat{\rho} \left(\theta \left(\eta_j^* \right) \right)}{2} \right) \rho w \left(\xi_i^* \right) w \left(\eta_j^* \right) \sigma_{jk}^0 \tag{3.29}$$

where NG_{ξ^*} and NG_{η^*} are the number of Gauss points in the ξ^* and η^* directions, respectively; $w \left(\xi_i^* \right)$ and $w \left(\eta_j^* \right)$ are the Gauss weights in the ξ^* and η^* directions, respectively. The values of θ_i and θ_f depend on which edge the collocation point under analysis lies on. The four possible cases are shown in Figure 14.

Finally, one can observe in Eq. (3.29) that the appearence of the new jacobian of transformation ρ cancels the term $1/r$ from the kernel $\varepsilon_{ijk}^*(\mathbf{x}', \mathbf{x})$ given in Eq. (3.6). Therefore, the weakly singular behavior is eliminated.

Figure 15 – Values of θ for cases where the collocation point is not in a cell corner.

Case 1

$$\theta_1^{\text{ini}} = 0 \qquad \theta_1^{\text{end}} = \operatorname{atan}\left(\frac{2}{\|1-\xi_0\|}\right)$$
$$\theta_2^{\text{ini}} = \theta_1^{\text{end}} \qquad \theta_2^{\text{end}} = \pi - \operatorname{atan}\left(\frac{2}{\|-1-\xi_0\|}\right)$$
$$\theta_3^{\text{ini}} = \theta_2^{\text{end}} \qquad \theta_2^{\text{end}} = \pi$$

Case 2

$$\theta_1^{\text{ini}} = \frac{\pi}{2} \qquad \theta_1^{\text{end}} = \frac{\pi}{2} + \operatorname{atan}\left(\frac{2}{\|1-\eta_0\|}\right)$$
$$\theta_2^{\text{ini}} = \theta_1^{\text{end}} \qquad \theta_2^{\text{end}} = \frac{3\pi}{2} - \operatorname{atan}\left(\frac{2}{\|-1-\eta_0\|}\right)$$
$$\theta_3^{\text{ini}} = \theta_2^{\text{end}} \qquad \theta_2^{\text{end}} = \frac{3\pi}{2}$$

$\times$ Collocation point

$\bullet$ Cell node

Case 3

$$\theta_1^{\text{ini}} = \pi \qquad \theta_1^{\text{end}} = \pi + \operatorname{atan}\left(\frac{2}{\|-1-\xi_0\|}\right)$$
$$\theta_2^{\text{ini}} = \theta_1^{\text{end}} \qquad \theta_2^{\text{end}} = 2\pi - \operatorname{atan}\left(\frac{2}{\|1-\xi_0\|}\right)$$
$$\theta_3^{\text{ini}} = \theta_2^{\text{end}} \qquad \theta_2^{\text{end}} = 2\pi$$

Case 4

$$\theta_1^{\text{ini}} = \frac{3\pi}{2} \qquad \theta_1^{\text{end}} = \frac{3\pi}{2} + \operatorname{atan}\left(\frac{2}{\|-1-\eta_0\|}\right)$$
$$\theta_2^{\text{ini}} = \theta_1^{\text{end}} \qquad \theta_2^{\text{end}} = \frac{5\pi}{2} - \operatorname{atan}\left(\frac{2}{\|1-\eta_0\|}\right)$$
$$\theta_3^{\text{ini}} = \theta_2^{\text{end}} \qquad \theta_2^{\text{end}} = \frac{5\pi}{2}$$
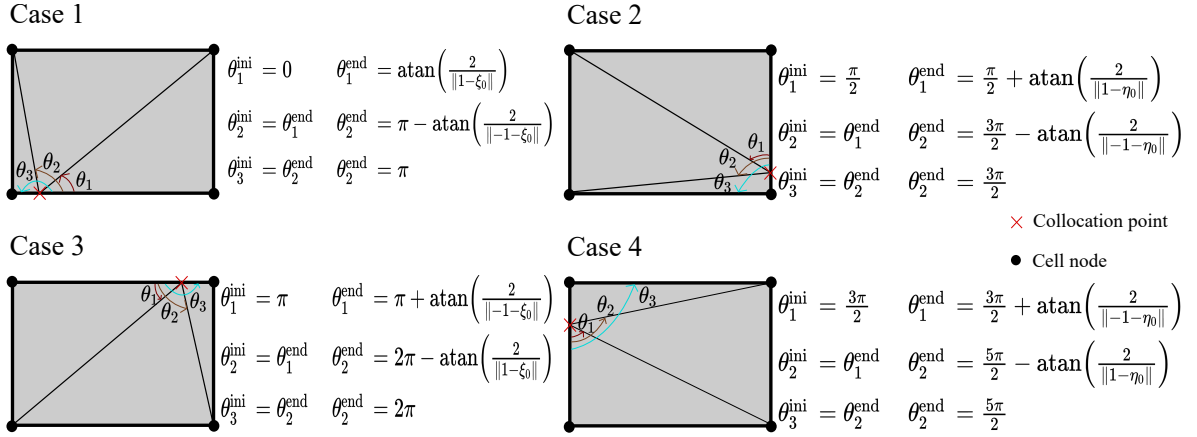
Source: The author.

Similarly, when the collocation point is not specifically situated on a cell corner, the singular behavior can be canceled by using the same transformation technique. The key distinction lies in subdividing the parametric space into three subelements, as illustrated in Figure 15. The corresponding values of θ_i and θ_f are depicted in the same figure for reference.

In order to show the effectivity of the proposed technique, the kernel $\varepsilon_{\text{ijk}}^*(\mathbf{x}', \mathbf{x})$ given in Eq. (3.6) is evaluated for the collocation point $cp = 2$ from Figure 11 before and after the transformation. As clearly seen in Figure 16a, the function exhibits a singular variation as the field point approaches the source one. After the transformation, the singular behavior is eliminated, as shown in Figure 16b.

To illustrate a scenario where the collocation point is displaced from the cell corner, a case analogous to the hypothetical one depicted in Figure 11 is examined. In this case, the collocation points $2, 3, 8$, and 9 are shifted from the corners by $1/4$ of the cell side length. The kernel $\varepsilon_{\text{ijk}}^*(\mathbf{x}', \mathbf{x})$ exhibits a singular behavior before the transformation to polar coordinates, as depicted in Figure 17a. After the transformation, the singular behavior is eliminated, as illustrated in Figure 17b. Finally, in Figure 17c a 2D view of the subelementation of the parametric space can be observed.

Figure 16 –   Comparison of the kernel $\varepsilon^*(\mathbf{x}', \mathbf{x})$ for a collocation point situated in a cell corner
(a) before and (b) after the transformation.

(a)   (b)
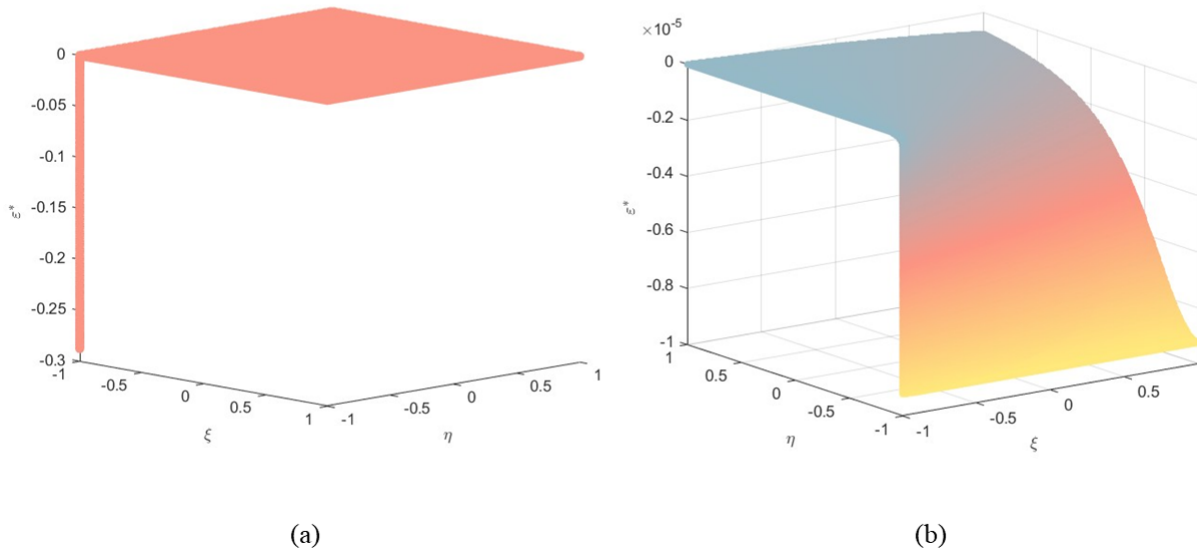
Source: The author.

Figure 17 –   Comparison of the kernel $\varepsilon^*(\mathbf{x}', \mathbf{x})$ for a collocation point shifted from the cell corner
(a) before (b) after the transformation and (c) 2D view of the subelementation of
the parametric space.
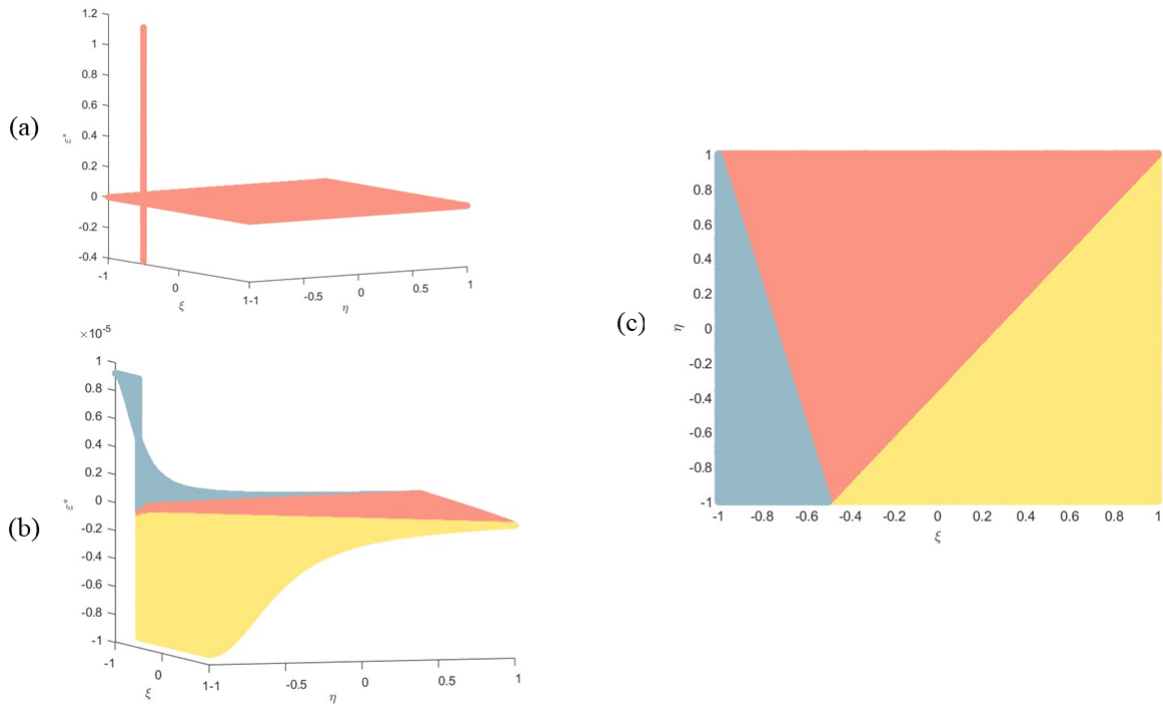
Source: The author.

4 LUMPED DAMAGE MECHANICS (LDM)

In this chapter the main concepts concerning the Lumped Damage Mechanics (LDM) are presented. The theory has its roots well consolidated in Flórez-López (1993) and Cipollina, López-Inojosa and Flórez-López (1995), and has been used in several works for the study of material failure in engineering structures (MARANTE; FLÓREZ-LÓPEZ, 2002; AMORIM; PROENÇA; FLÓREZ-LÓPEZ, 2013; BAI *et al.*, 2016; BAZÁN; BECK; FLÓREZ-LÓPEZ, 2019; BAI *et al.*, 2021; ZHOU *et al.*, 2022). The process of structural deterioration is captured through the incorporation of the internal damage variable, initially formulated for one-dimensional problems in the earlier literature. The damage variable is coupled into plastic hinges and its evolution law depend on thermodynamic forces associated to damage. The extension for two-dimensional problems was first addressed in Amorim (2016). In the following, the main concepts of the LDM are presented, with emphasis on the formulation for two-dimensional problems, since the present work is based on this formulation.

4.1 Lumped Damage Mechanics (LMD) - 1D problems

Lemaitre and Chaboche (1994) are pioneers in the field of continuum damage mechanics. Their theory is based on the thermodynamics of irreversible processes and draws from concepts introduced and established in earlier works, such as those by Kachanov (1958) and Rabotnov (1969). According to the authors, the damage theory describes the evolution of the phenomena between the unaltered state and the macroscopic crack initiation. The alteration of the material is represented by a scalar variable, called damage variable. This variable is a measurement of the material degradation. By considering a uniform damage distribution in every material's direction, the scalar damage variable ω is defined as the ratio between the damaged area A_d and the total area of the material A, as follows:

$$\omega = \frac{A_d}{A} \tag{4.1}$$

Thus, mathematically, ω assumes values from 0 to 1, where 0 represents the undamaged state and 1 represents the fully damaged state. In addition to the concept of damage variable, the authors also introduce the concept of effective stress, which is the stress which effectively resistis the acting forces once the damage is considered. The effective stress $\bar{\sigma}$ is defined as:

$$\bar{\sigma} = \frac{P}{A - A_d} \tag{4.2}$$

Figure 18 – Frame element as a combination of an elastic beam and inelastic hinges.
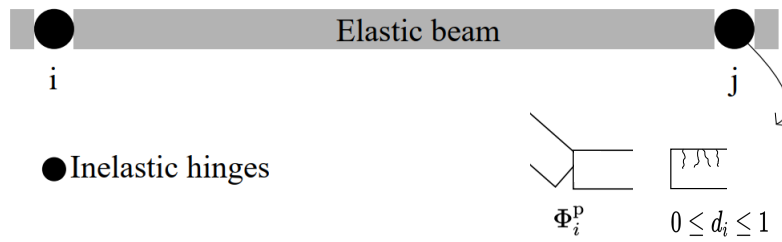
Source: The author.

where P is a unixal force acting on the material. This relation is rewritten in terms of the damage variable, by substituting the damaged area A_d into Eq. (4.2), as follows:

$$\bar{\sigma} = \frac{P}{A - A\omega} = \frac{P}{A(1 - \omega)} \Rightarrow \bar{\sigma} = \frac{\sigma}{1 - \omega} \tag{4.3}$$

The effective stress tends to infinity when the damage variable tends to one, and it assumes the normal stress value when the damage variable is equal to zero.

Therefore, with the aim to broader the applicability of the damage theory, Flórez-López (1993) first formulated LDM for the analysis of framed structures. By considering fracture mechanics concepts and the classic damage theory, a finite element for the inelastic analysis of frames considering elasto-plastic effects and damage is proposed. The general idea was to consider the inelastic effect due to damage coupled into plastic hinges. It enables the quantification of structural damage and represents the mechanical behaviour by considering the internal variable of damage $(D)_b = (d_i, d_j)$ coupled into plastic hinges. These hinges are then inelastic hinges (Figure 18). This consideration enables the simulation of material degradation phenomena caused by crack growth. The strain localization effect is lumped into a region with a very small thickness when compared to the element size, while the rest of the element remains elastic (FLÓREZ-LÓPEZ; MARANTE; PICÓN, 2015).

The model also includes linear kinematic hardening for reinforcements, which accounts for the Bauschinger effect in the formulation. This refinement of the basic relationships between material microstructure and plastic behavior allows for a better interpretation of the internal stresses on the hardening, as stated by Bate and Wilson (1986). This effect influences the decrease of the yield stress of the material due to the process of loading until the plastic limit, unloading and then loading it again with opposite values of loads (ZHONGHUA; HAICHENG, 1990). Such phenomenon has been ignored in models that consider plastic strains, such as in the perfect plasticity and isotropic hardening models (ARMSTRONG; FREDERICK *et al.*, 1966).

In fracture mechanics, the Griffith criterion is used to evaluate the fracture process from an energy criterion. Similarly, the propagation simulation in LDM respects the same criterion, i.e., the energy release rate is set to be equal to the resistance to cracking, otherwise the damage value is equal to zero. From this perspective, a damage evolution law is settled:

$$\begin{cases} \dot{d} = 0 \text{ if } y < R \\ y = R \text{ if } \dot{d} > 0 \end{cases} \qquad (4.4)$$

where the dot over the variable d indicates a variation. Hence, the damage $\dot{d}$ is equal to zero while the energy release y rate assumes a value less than the resistance to cracking R, and in case this value is reached, the damage starts to evolve.

Important to mention is that the mesh-independency is an important characteristic of LDM in front of the classical continuous damage theory. In the classical hypothesis, the structure response force-displacement remains the same until the moment when the strain localization begins to exist. This problem represents a physical phenomenon characterized by the appearence of the localization bands and it leads to ill-posed mathematical problems, since the solution is not unique (FLÓREZ-LÓPEZ; MARANTE; PICÓN, 2015). Hence, as explained in Amorim (2016), the term *localization* refers to two distinct situations: (i) in experimental mechanics, where localization defines the formation of shear bands with strain discontinuities, for example; (ii) in structural mechanics, where localization is related to the mathematical analysis of classic damage models, being observed in cases with loss of ellipticity leading to ill-posed and mesh-dependent problems.

Thus, in order to illustrate the mesh-dependence in classic damage mechanics, Flórez-López, Marante and Picón (2015) and Amorim (2016) consider a uniaxial case, where the displacement is prescribed at both ends, as shown in Figure 19a. The total element of length l is divided into two parts of length l_1 and l_2. According to Amorim (2016), the local damage constitutive equation is defined by:

$$\sigma = (1 - \omega)E\varepsilon \qquad (4.5)$$

where σ is the stress, ω is the damage variable, E is the Young's modulus ε is the strain. The damage evolution law is given by:

$$G^\omega(\varepsilon) - R^\omega(\omega) \leq 0 \quad \therefore \begin{cases} G^\omega(\varepsilon) = |\varepsilon| \\ R^\omega(\omega) = \frac{\varepsilon_{cr}\varepsilon_u}{\varepsilon_u + \omega(\varepsilon_{cr} - \varepsilon_u)} \end{cases} \qquad (4.6)$$

in which $G^\omega(\varepsilon)$ is the energy release rate, $R^\omega(\omega)$ is the resistance to cracking, ε_{cr} and ε_u are the critical and ultimate strain, respectively, as shown in Figure 19b. A two-node finite element with linear displacement can be obtained by conventional procedures. In such

Figure 19 – (a) Uniaxial bar (b) stress-strain relationship in the local damage model and (c) force-displacement relationship for different l_1 values.

(a) (b) (c)
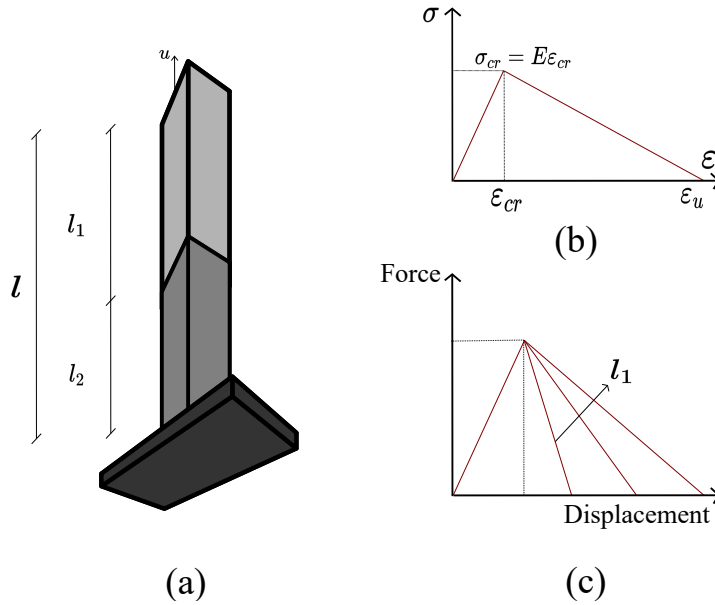
Source: Adapted from Amorim (2016).

case, an exact solution is known. The mesh-dependence of the numerical response can ben seen in Figure 19c, where the force-displacement curve is shown for different l_1 values. The response starts to depend on the chosen length of the element under analysis, when solutions localizing in only one element are chosen (AMORIM, 2016).

The mesh-dependece is not observed when LDM is used. The replacement of the kinematic variable is the main point for this to happen: the elongation is used instead of the strain. Similar to the strain equivalence hypothesis defined by Lemaitre and Chaboche (1994), as presented in Eq. (4.7) - where the strain is decomposed into an elastic term ε_e and a damage-related term ε_d - Amorim *et al.* (2018) introduces the elongation equivalence hypothesis, as provided in Eq. (4.8).

$$\varepsilon = \frac{\sigma}{(1-\omega)E}; \quad \Leftrightarrow \quad \varepsilon = \varepsilon^e + \varepsilon^\omega \tag{4.7}$$

$$\delta = \delta^e + \delta^d; \quad \delta^e = \frac{L}{E}\sigma \tag{4.8}$$

where δ is the total elongation, δ^e is the elastic part, δ^d is a measure of deformation for the localization band and L is the length of the element. The localization band is the region where the damage is concentrated.

By considering the strain equivalence hypothesis, the constitutive equations shown in Eqs. (4.5) and (4.6) can be rewritten as:

$$\varepsilon = \frac{1}{E}\sigma + \varepsilon^\omega; \quad g = \sigma - \sigma_{cr}\left(1 - \frac{\varepsilon^\omega}{\varepsilon_u}\right) \le 0 \tag{4.9}$$

Therefore, anagously, the elongation equivalence hypothesis can be used to rewrite the damage function according to:

$$g = \sigma - \sigma_{cr}\left(1 - \frac{\delta^d}{\delta_u}\right) \le 0 \tag{4.10}$$

where σ_{cr} and δ_u are the critical stress and ultimate elongation, respectively, being material parameters. Amorim *et al.* (2018) compare Eq. (4.10) with the tension-softening law in the Fracture Process Zone (FPZ), from fracture mechanics, where the damage-related elongation is analogous to the crack-opening displacement.

For concluding, still following Amorim *et al.* (2018), it is possible to observe that in the classic damage model, when the material is fully damaged, meaning the damage variable reaches a value of one, the stress is reduced to zero. This implies that the elastic strain is likewise reduced to zero, leaving only the strain associated to damage. Looking at Eq. (4.9), if the stress value is equal to zero, $\varepsilon_w = \varepsilon_u$, i.e, there is a mesh-dependence, since the ultimate displacement is equal to the ultimate strain times the length of the element. On the other hand, as the lumped damage model considers the elongations instead of the strains, the elongation of the localization band is equal to δ_u when damage is equal to one and the stress is equal to zero. This gives a mesh-independent solution, as shown in Figure 19e, since the ultimate displacement does not depend on the length of the element.

4.2   Extended Lumped Damage Mechanics (XLMD) - 2D Problems

As the LDM is limited for the study of arches and frames, Amorim (2016) proposed an extension of the theory for the analysis of two-dimensional continuous media. The formulation is based on the same principles of the conventional LDM. However, adaptations are necessary to consider the two-dimensional discretization. For instance, in this case, the inelastic effect is no longer coupled into hinges: there are now inelastic lines. Thus, such inelastic lines are localization bands concentrating material nonlinear phenomena while the rest of the element remains elastic. Figure 20 shows as an example the idealisation of the lumped damage model for a two-dimensional element.

The first idealization of XLDM considers a conventional four-node quadrilateral element. Figure 21a shows this element in the cartesian space and 21c presents the element representation in the parametric (reference) space. Through the conventional shape functions for a quadrilateral element, the strains can be obtained via Eq. 4.11.

$$\{\boldsymbol{\varepsilon}\}_b = [\mathbf{B}]_b\{\mathbf{q}\}_b \tag{4.11}$$

Figure 20 – Inelastic lines in the XLDM.
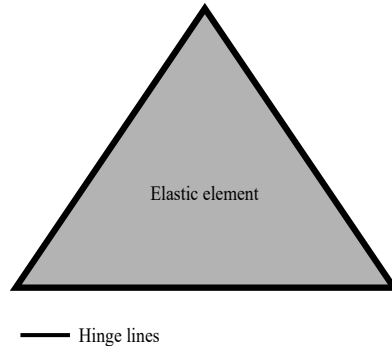
Source: Adapted from Amorim (2016).

where $\{\boldsymbol{\varepsilon}\}_b$ is the vector of nodal strains and $\{\mathbf{q}\}_b$ is the vector of nodal displacements b. The matrix $[\mathbf{B}]_b$ is the kinematic transformation matrix for the element b, presented in Appendix D.

Hence, as can be seen in Figure 21b, Amorim (2016) introduces the idealisation of an equivalent five-bar truss. These bars are considered numerical extensometers, then called "*numexes*", and the generalized deformation where the total elongations of the bars are represented by the expression given below:

$$\{\boldsymbol{\delta}\}^T = [\delta_{ij}, \delta_{ik}, \delta_{il}, \delta_{jk}, \delta_{kl}] \tag{4.12}$$

where δ_{ij} represents the elongation of the bar defined by nodes i and j; δ_{ik} of the bar defined by nodes i and k and so on. Any combination of five *numexes* could be assumed to define the deformed state of the element, in other words, the diagonal bar *j-l* could be replaced by any other bar. Hence, the elongations and the displacements of an element b can be related according to:

$$\{\boldsymbol{\delta}\}_b = [\mathbf{b}]_b\{\mathbf{q}\}_b \tag{4.13}$$

where $\{\mathbf{q}\}_b$ is the vector of generalized displacements b and $[\mathbf{b}]_b$ is the kinematic transformation of the *numexes*, which is also presented in Appendix D.

The strain tensor in any point of the conventional element depends on five constants and can be written as a function of the elongations, as follows:

$$\{\varepsilon\}_b = [\boldsymbol{T}]_b\{\boldsymbol{\delta}\}_b \tag{4.14}$$

where $[\boldsymbol{T}]$ is the kinematic transformation matrix in cartesian coordinates relating the numexes and the strains. For obtaining the matrix $[\boldsymbol{T}]$, Eqs. (4.11) and (4.14) are combined, resulting in:

Figure 21 – (a) Conventional four-node quadrilateral element; (b) equivalent truss and (c) parametric space.

(a)   (b)   (c)
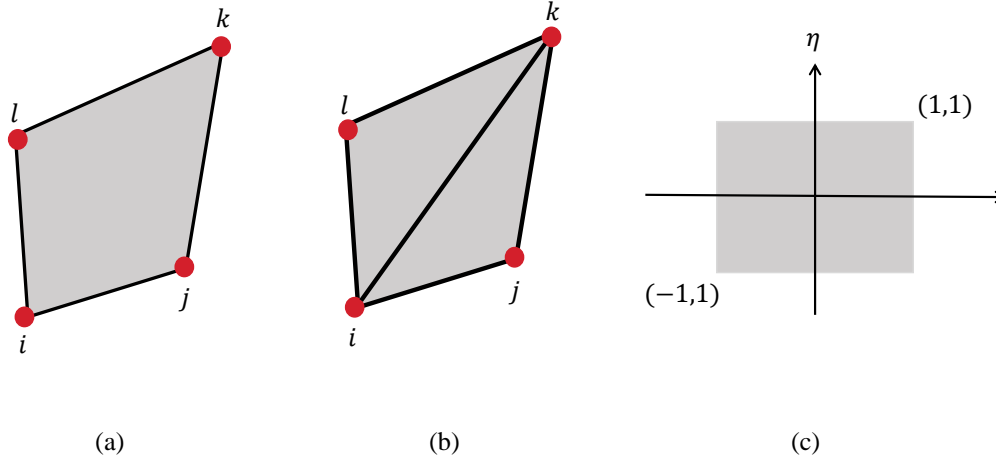
Source: Adapted from Amorim (2016).

$$[\boldsymbol{T}]_b = \left([\boldsymbol{B}]_b[\boldsymbol{b}]_b^T\right)\left([\boldsymbol{b}]_b[\boldsymbol{b}]_b^T\right)^{-1} \tag{4.15}$$

Therefore, the stress matrix is then expressed as:

$$\{\boldsymbol{\sigma}\}_b = [\boldsymbol{H}]_b[\boldsymbol{T}]_b\{\boldsymbol{\delta}\}_b \tag{4.16}$$

where $[\boldsymbol{H}]_b$ is the matrix of elastic coefficients. It is important to remember that for a pure elastic analysis, $\{\boldsymbol{\delta}\}_b = \{\boldsymbol{\delta^e}\}_b$.

Up to this point, all relationships have solely taken into account the elastic part of the analysis. The localization bands are the location where the material's deterioration process is inserted. Initially, the bands have zero thickness. During the analysis, the elongations associated to the lumped damage are added. The relationship between the damage elongations and the band's thickness, in the reference space, is given by:

$$\left\{\boldsymbol{\delta^d}\right\}_b = \left\{\begin{array}{c} 0 \\ \epsilon_{i\eta}\sqrt{2}/2 \\ \epsilon_{i\eta} \\ \epsilon_{j\eta} \\ 0 \end{array}\right\} + \left\{\begin{array}{c} \epsilon_{j\xi} \\ \epsilon_{k\xi}\sqrt{2}/2 \\ 0 \\ 0 \\ \epsilon_{i\xi} \end{array}\right\} + \left\{\begin{array}{c} 0 \\ \epsilon_{k\xi}\sqrt{2}/2 \\ \epsilon_{l\eta} \\ \epsilon_{k\eta} \\ 0 \end{array}\right\} + \left\{\begin{array}{c} \epsilon_{i\xi} \\ \epsilon_{i\xi}\sqrt{2}/2 \\ 0 \\ 0 \\ \epsilon_{l\xi} \end{array}\right\} \tag{4.17}$$

where the thicknesses of the bands, $\epsilon_{i\xi}$, $\epsilon_{j\xi}$, $\epsilon_{k\xi}$, $\epsilon_{l\xi}$, $\epsilon_{k\eta}$ and $\epsilon_{i\eta}$ in each correspondent node are shown in Figure 22. Furthermore, it can be observed that a linear variation in these

Figure 22 – Representation of the (a) localization bands and of (b) the thickness of each localization band.

(a) (b)
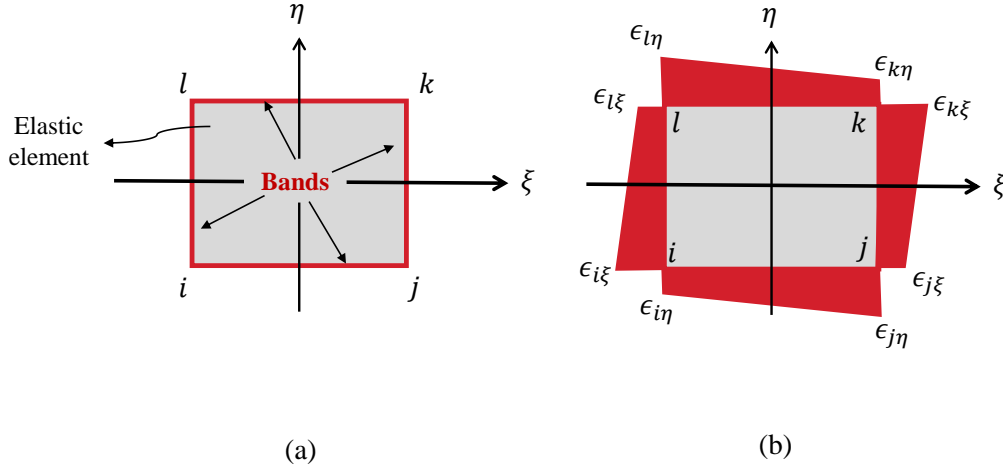
Source: Adapted from Amorim (2016).

thicknesses is assumed due to the nature of the shape functions of the element. The $\left\{ \boldsymbol{\delta}^d \right\}$ in cartesian coordinates is presented in Appendix D as well.

In this sense, the additive strain decomposition - valid only for small strains - sets that the elongations can be written as a sum of the elastic elongations $\{\boldsymbol{\delta}^e\}$ and the ones that come from the localization bands $\left\{ \boldsymbol{\delta}^d \right\}$, as shown below:

$$\{\boldsymbol{\delta}\} = \{\boldsymbol{\delta}^e\} + \left\{ \boldsymbol{\delta}^d \right\} \tag{4.18}$$

The material behaviour is then described when the set of constitutive equations is completed by the introduction of a damage law for each band thickness. For an element with four localization bands, the damage laws in each node of the element for each band are the nonlinear ones proposed by Teles (2022), as follows:

$$
\begin{aligned}
g_i^{ij} &= \sigma_i^{ij} - \sigma_{cr_i}^{ij} \exp\left(q\delta_i^{ij} \right) \leq 0; \, g_j^{ij} = \sigma_j^{ij} - \sigma_{cr_j}^{ij} \exp\left(q\delta_j^{ij} \right) \leq 0; \\
g_i^{il} &= \sigma_i^{il} - \sigma_{cr_i}^{il} \exp\left(q\delta_i^{il} \right) \leq 0; \, g_l^{il} = \sigma_l^{il} - \sigma_{cr_j}^{il} \exp\left(q\delta_l^{il} \right) \leq 0; \\
g_j^{jk} &= \sigma_j^{jk} - \sigma_{cr_j}^{jk} \exp\left(q\delta_j^{jk} \right) \leq 0; \, g_k^{jk} = \sigma_k^{jk} - \sigma_{cr_k}^{jk} \exp\left(q\delta_k^{jk} \right) \leq 0; \\
g_l^{jk} &= \sigma_l^{jk} - \sigma_{cr_l}^{lk} \exp\left(q\delta_j^{lk} \right) \leq 0; \, g_k^{lk} = \sigma_k^{lk} - \sigma_{cr_k}^{lk} \exp\left(q\delta_k^{lk} \right) \leq 0;
\end{aligned}
\tag{4.19}
$$

where g_i^{ij}, σ_i^{ij}, $\sigma_{cr_i}^{ij}$, and δ_i^{ij} are, respectively, the damage law, the perpendicular stress value at the node, critical stress and the band thickness referent to node i at the ij band, and so on for the other indices; q is a parameter of the model.

The damage laws provided in Teles (2022) differ from those presented in Amorim (2016), as they exhibit exponential behavior. The parameter q is introduced into the

new exponential functions, presenting an interesting aspect. According to Teles (2022), the parameter is related to the concept of fracture energy addressed in classic fracture mechanics. Fracture energy refers to the work required to rupture a notched cross-section and is calculated as follows:

$$G_f = \int_0^{\delta_c} \sigma\left(\delta^d\right) d\delta^d \tag{4.20}$$

in which δ_c is the critical band thickness that leads to the rupture of the material and $\sigma\left(\delta^d\right)$ is the stress as a function of the band thickness opening due to damage, as given by:

$$\sigma\left(\delta^d\right) = \sigma_{cr} \exp\left(q\delta^d\right) \tag{4.21}$$

which is nothing but the general form of the damage law given in Eq. (4.19). Integrating Eq. (4.20) from zero to δ_c, one obtains:

$$Gf = \frac{\sigma_{cr}\left(\exp^{q\delta_c} - 1\right)}{q} \tag{4.22}$$

Note that in Eq. (4.21) as σ approaches to zero, regardless of the σ_{cr} value, δ_c assumes a negative value divided by q. Taking this information into Eq. (4.22) leads to the following:

$$G_f = -\frac{\sigma_{cr}}{q} \tag{4.23}$$

Hence, by analyzing the units of the terms in Eq. (4.23), it becomes evident that the parameter q assumes units inversely proportional to length measurements (e.g., m^{-1}, mm^{-1}, etc.). This parameter is then adjusted by each material through experimental studies, as given in Teles (2022). Therefore, in the following subsection, a solution procedure for solving the nonlinear equations of the XLDM constitutive model is presented.

4.2.1 Solution of the Constitutive Nonlinear System of Equations

For the local solution, the calculation of variables related to the *numexes* and band thickness is performed. Given the interdependence between stress node values and band thickness - where stress node values rely on the band thickness, and the band thickness is influenced by the stress node values - the constitutive system of equations is nonlinear. To solve this system, the Newton-Raphson method is employed.

As discussed in Teles (2022), from the plane state relationships, the stresses acting on the plane perpendicular to the localization band are obtained through the rotation of the stress tensor components to the local coordinate system, i.e:

$$[\boldsymbol{\sigma'}] = [\boldsymbol{R}]^T[\boldsymbol{\sigma}][\boldsymbol{R}] \tag{4.24}$$

where $[\boldsymbol{R}]$ is the rotation matrix, which is defined as:

$$\left[\boldsymbol{R}\right]^T = \begin{bmatrix} \cos(\theta) & \sin(\theta) \\ -\sin(\theta) & \cos(\theta) \end{bmatrix} \tag{4.25}$$

in which θ is the angle the angle between the x_1 direction and the direction normal to the localization band. For instance, for the stress value at node i on the plane normal to the localization band ik, one obtains:

$$\sigma_i^{ik} = \sigma_{11}cos(\theta)_{ik}^2 + \sigma_{22}sin(\theta)_{ik}^2 + \tau_{12}cos(\theta)_{ik}sin(\theta)_{ik} \tag{4.26}$$

In the analysis, an incremental procedure is employed, where displacements are progressively incremented at each load step. The elastic prediction step is performed by assuming that the damage is equal to zero. Then, with the perpendicular stress values, the damage criterion given in Eq. (4.19) is verified. If the damage law is satisfied, i.e, if $g \leq 0$, a new load step is performed. Otherwise, the corrector algorithm is called to solve the nonlinear constitutive equations and, consequently, to obtain the new values of stresses and band thicknesses.

For each cell element, there are five elasticity laws, i.e, an elastic law for each *numex* that must be satisfied, as follows:

$$\{\boldsymbol{\sigma}\}_b - [\boldsymbol{H}]_b[\boldsymbol{T}]_b\{\boldsymbol{\delta}^e\}_b = \boldsymbol{0} \tag{4.27}$$

in which $\{\boldsymbol{\delta}^e\}_b = \{\boldsymbol{\delta}\}_b - \{\boldsymbol{\delta}^d\}_b$.

Additionally to the five elasticity laws, there are eight damage evolution laws, given in Eq. (4.19). Therefore, the system of equations to be solved is equal to:

$$\begin{aligned} \boldsymbol{R}\left(\{\boldsymbol{\sigma}\}_b + \{\boldsymbol{\Delta\sigma}\}_b, \{\boldsymbol{\delta}\}_b + \{\boldsymbol{\Delta\delta}\}_b\right) &= \{\boldsymbol{\sigma}\}_b - [\boldsymbol{H}]_b[\boldsymbol{T}]_b\left\{\boldsymbol{\delta}^e\right\}_b = \boldsymbol{0} \\ \boldsymbol{g}\left(\{\boldsymbol{\sigma}\}_b + \{\boldsymbol{\Delta\sigma}\}_b, \{\boldsymbol{\delta}\}_b + \{\boldsymbol{\Delta\delta}\}_b\right) &= \boldsymbol{0} \end{aligned} \tag{4.28}$$

where R represents the elasticity law and g the damage one. The system is linearized and solved through an iterative process based on the Newton-Raphson method. Hence, expanding in Taylor series and truncating at the linear term, the following is obtained:

$$\begin{aligned} \boldsymbol{R}_0(\boldsymbol{\sigma},\boldsymbol{\delta}) + \frac{\partial \boldsymbol{R}(\boldsymbol{\sigma},\boldsymbol{\delta})}{\partial \boldsymbol{\sigma}}\Delta\boldsymbol{\sigma} + \frac{\partial \boldsymbol{R}(\boldsymbol{\sigma},\boldsymbol{\delta})}{\partial \boldsymbol{\delta}}\Delta\boldsymbol{\delta} &= \boldsymbol{0} \\ \boldsymbol{g}_0(\boldsymbol{\sigma},\boldsymbol{\delta}) + \frac{\partial \boldsymbol{g}(\boldsymbol{\sigma},\boldsymbol{\delta})}{\partial \boldsymbol{\sigma}}\Delta\boldsymbol{\sigma} + \frac{\partial \boldsymbol{g}(\boldsymbol{\sigma},\boldsymbol{\delta})}{\partial \boldsymbol{\delta}}\Delta\boldsymbol{\delta} &= \boldsymbol{0} \end{aligned} \tag{4.29}$$

which in matrix form is given by:

Figure 23 – Flowchart of the corrector algorithm.
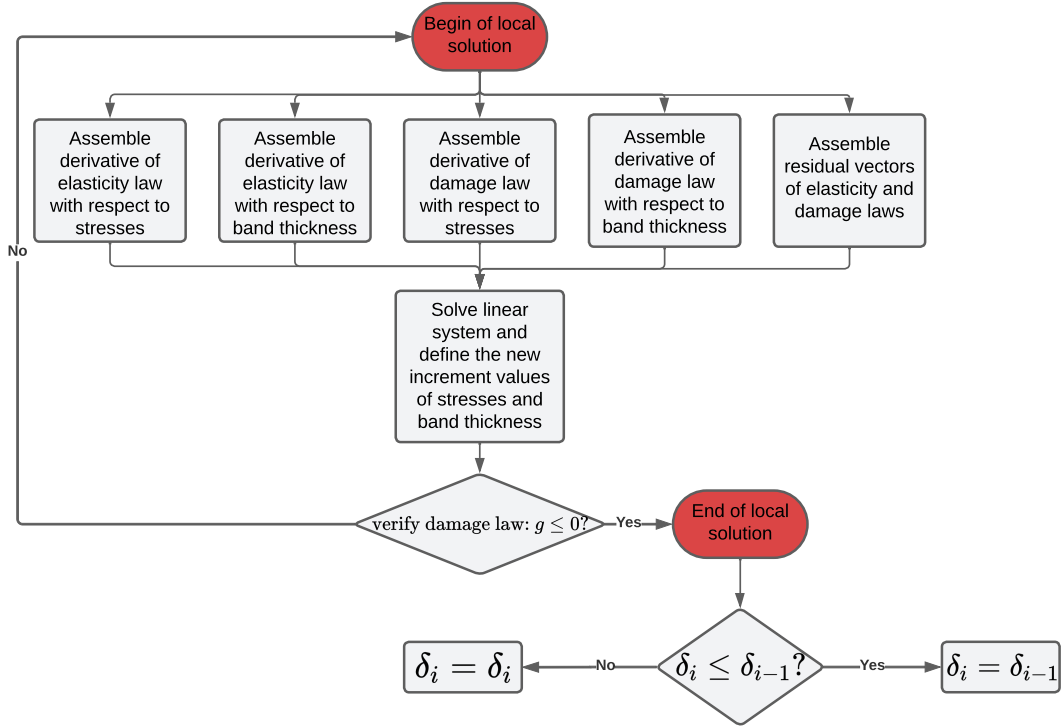
The author.

$$
\begin{bmatrix} \frac{\partial \boldsymbol{R}}{\partial \boldsymbol{\sigma}} & \frac{\partial \boldsymbol{R}}{\partial \boldsymbol{\delta}} \\ \frac{\partial \boldsymbol{g}}{\partial \boldsymbol{\sigma}} & \frac{\partial \boldsymbol{g}}{\partial \boldsymbol{\delta}} \end{bmatrix} \left\{ \begin{array}{c} \Delta \boldsymbol{\sigma} \\ \Delta \boldsymbol{\delta} \end{array} \right\} = \left\{ \begin{array}{c} -\boldsymbol{R}_0 \\ -\boldsymbol{g}_0 \end{array} \right\} \tag{4.30}
$$

or better writting in order to explicit the size of each matrix:

$$
\begin{bmatrix} \left[\frac{\partial \boldsymbol{R}}{\partial \boldsymbol{\sigma}}\right]_{12\times12} & \left[\frac{\partial \boldsymbol{R}}{\partial \boldsymbol{\delta}}\right]_{12\times8} \\ \left[\frac{\partial \boldsymbol{g}}{\partial \boldsymbol{\sigma}}\right]_{8\times12} & \left[\frac{\partial \boldsymbol{g}}{\partial \boldsymbol{\delta}}\right]_{8\times8} \end{bmatrix} \left\{ \begin{array}{c} \{\Delta \boldsymbol{\sigma}\}_{12\times1} \\ \{\Delta \boldsymbol{\delta}\}_{8\times1} \end{array} \right\} = \left\{ \begin{array}{c} \{\boldsymbol{R}_0\}_{12\times1} \\ \{\boldsymbol{g}_0\}_{8\times1} \end{array} \right\} \tag{4.31}
$$

in which $\Delta \boldsymbol{\sigma}$ is the vector of increments of the stress components, $\Delta \boldsymbol{\delta}$ is the vector of increments of the elongation components, $\boldsymbol{R_0}$ and $\boldsymbol{g_0}$ are the residual vectors of the elasticity and damage laws, respectively.

The matrices given in Eq. (4.31) are detailed in Appendix D. Hence, when the adopted damage tolerance is achieved, the solution is obtained. Therefore, the corrector algorithm for the local problem is illustrated in Figure (23) and explicited in Algorithm 1. Note that the convergence is achieved when the adopted damage tolerance is respected for every cell. Moreover, a final assessment of the band thickness is conducted to ensure that the updated values accurately reflect the physical reality of problem, i.e, if it indeed demonstrates the proper evolution of material failure mechanisms.

Therefore, with the defined constitutive damage model and with the discretization via cells to represent the initial stress fields, the solution to the global equilibrium equations

---

Algorithm 1: Corrector Algorithm

---

1 **foreach** *cell* **do**
2   **while** *damage criterion is TRUE* **do**
3   **call** *subroutine assemble XLDM matrices* - In this subroutine the following
             matrices and vectors are assembled:

4
$$\begin{bmatrix} \left[\dfrac{\partial \boldsymbol{R}}{\partial \boldsymbol{\sigma}}\right]_{12\times12} & \left[\dfrac{\partial \boldsymbol{R}}{\partial e}\right]_{12\times8} \\ \left[\dfrac{\partial \boldsymbol{g}}{\partial \boldsymbol{\sigma}}\right]_{8\times12} & \left[\dfrac{\partial \boldsymbol{g}}{\partial e}\right]_{8\times8} \end{bmatrix} \tag{4.32}$$

5   and

6
$$\left\{ \begin{array}{c} \{\boldsymbol{R_0}\}_{12\times1} \\ \{\boldsymbol{g_0}\}_{8\times1} \end{array} \right\} \tag{4.33}$$

7   **call** *subroutine solve linear system* - This subroutine provides the solution of the
             system of equations, where the new values of $\{\boldsymbol{\Delta\sigma}\}$ and $\{\boldsymbol{\Delta\delta}\}$ are obtained.
8   **if** *damage law is verified* **then**
9   damage criterion = .FALSE. **else**
10   damage criterion = .TRUE.
11   **end**
12   **end**
13   **end**
14 **end**
15 **if** *band thickness(i).LE.band thickness(i-1)* **then**
16   band thickness(i) = band thickness(i-1) **else**
17   band thickness(i) = band thickness(i)
18   **end**
19 **end**

---

can be obtained by the implementation of a predictor-corrector algorithm. Through the relations presented in section 3.2, the global solution is obtained by the steps shown in Algorithm 2. Note that in this last Algorithm, a subroutine named *cell nodes ID* is called for determining cell nodes position by verifying whether each node is located within the domain or on the boundary. If a node is on the boundary, the subroutine further checks whether it coincides with a control point or a collocation point. This is necessary for correctly defining the term positions in vectors $\{\boldsymbol{x}\}_i$ and $\{\boldsymbol{u}_{\mathrm{int}}\}_i$. In addition, the tensor of initial stresses is assigned to the vector $\Delta\boldsymbol{\sigma}$ provenient from the corrector algorithm. Hence, the stresses are reapplied on the body and the global solution is sought.

Algorithm 2: Predictor-corrector algorithm

---

1 Assembling constant BEM matrices and vectors of the problem, given in section 3.2:

$$[\boldsymbol{A}], [\boldsymbol{A'}], \left[\boldsymbol{A^{-1}}\right], \{\boldsymbol{f}\}, \{\boldsymbol{f'}\} \rightarrow [\boldsymbol{R}], [\boldsymbol{S}], \{\boldsymbol{m}\} \text{ and } \{\boldsymbol{n}\}$$

2 **call** *subroutine cell nodes ID*

3 PREDICTOR STAGE:

4 **foreach** *increment* **do**

5
$$\{\Delta\mathbf{x}\} = \{\Delta\boldsymbol{m}\}$$
$$\{\Delta\boldsymbol{u}\} = \{\Delta\boldsymbol{n}\}$$
$$\{\Delta\mathbf{x}\}_i = \{\Delta\mathbf{x}\}_i + \{\Delta\mathbf{x}\}$$
$$\{\boldsymbol{u}_{\text{int}}\}_i = \{\boldsymbol{u}_{\text{int}}\}_i + \{\Delta\boldsymbol{m}\}$$

6   **foreach** *cell* **do**

7
$$\{\boldsymbol{\delta}\} = \left\{\boldsymbol{\delta^e} + \boldsymbol{\delta^d}\right\} \rightarrow \boldsymbol{\delta^d} = \{\mathbf{0}\}$$
$$\{\boldsymbol{\Delta\varepsilon}\} = [\boldsymbol{T}]\{\boldsymbol{\Delta\delta^e}\}$$
$$\{\boldsymbol{\varepsilon}\} = \{\boldsymbol{\varepsilon}\} + \{\boldsymbol{\Delta\varepsilon}\}$$
$$\{\boldsymbol{\Delta\sigma}\} = [\boldsymbol{H}][\boldsymbol{T}]\{\boldsymbol{\delta^e}\}$$
$$\{\boldsymbol{\sigma}\} = \{\boldsymbol{\sigma}\} + \{\boldsymbol{\Delta\sigma}\}$$

8   **end**

9   CORRECTOR STAGE:

10   **if** *damage criterion = .TRUE.* **then**

11   **foreach** *violated cell node* **do**

12   **call** *corrector subroutine* given in Algorithm 1.

13   **end**

14 $\{\Delta\boldsymbol{\sigma_0}\} = \{\Delta\boldsymbol{\sigma}\}$ from the corrector Algorithm. This is reapplied on the boundary.

$$\{\Delta\mathbf{x}\} = [\boldsymbol{R}]\{\Delta\boldsymbol{\sigma_0}\}$$
$$\{\Delta\boldsymbol{u}_{\text{int}}\} = [\boldsymbol{S}]\{\Delta\boldsymbol{\sigma_0}\}$$
$$\{\mathbf{x}\}_i = \{\mathbf{x}\}_i + \{\Delta\mathbf{x}\}$$
$$\{\boldsymbol{u}_{\text{int}}\}_i = \{\boldsymbol{u}_{\text{int}}\}_i + \{\Delta\boldsymbol{u}_{\text{int}}\}$$

15   **call** *elasticity law subroutine* - With the new displacements, the elasticity law is called, and the new stress values are computed via:

$$\{\Delta\boldsymbol{\sigma}\} = [\boldsymbol{H}][\boldsymbol{T}]\{\Delta\boldsymbol{\delta^e}\}$$
$$\{\boldsymbol{\sigma}\} = \{\boldsymbol{\sigma}\} + \{\Delta\boldsymbol{\sigma}\}$$

16   Compute $\frac{\|\boldsymbol{\Delta u}_{\text{int }i}\|}{\|\boldsymbol{u}_{\text{ini}}\|}$

17   **if** $\frac{\|\boldsymbol{\Delta u}_{int\,i}\|}{\|\boldsymbol{u}_{ini}\|} > global\ tolerance$ **then**

18   **call** *corrector subroutine*

19   **else**

20   go to a new increment.

21   **end**

22   **end**

23   **end**

24 **end**

---

5 RESULTS AND DISCUSSIONS

In this chapter, the BEM is applied to study both linear and nonlinear problems. The unknown functions of displacements and tractions are obtained via such numerical method. All the techniques and methodologies presented in this work are implemented in an in-house code written in FORTRAN 90. The numerical discretization considers the isogeometric approach with h-refinement. Additional techniques have been incorporated to address a wider range of problems, including the subregions technique and the application of the Galerkin vector methodology for handling body forces (C).

To assess the accuracy of the implementations developed so far, the following numerical examples are presented: in the first section, two linear problems are solved, namely, a dam with three different materials and concrete tunnel under uniform pressure. The problems serve to assess the accuracy of the implementations regarding pure linear problems. Comprehensive results of these two problems are given in Nardi and Leonel (2023). On the other hand, in the second section, three nonlinear problems are solved: a square plate under uniform displacement, a L-shaped plate and a three-point bending beam.

The results provided by the proposed BEM approach have been compared to numerical and experimental responses available in the literature. For the linear ones, the results are contrasted with those obtained via the well-known FEM ANSYS © software. Meanwhile, for the nonlinear scenarios, the results of the first two problems are compared against the findings from a FEM analysis presented in Teles (2022) and experimental responses available in the literature. The three point bending beam is a showcase example, with the outcomes compared with the ones provided by Saleh *et al.* (1997). The nonlinear problems section presents the effectiveness of the initial stress field approach via BEM with the adopted constitutive model, the XLMD.

5.1 Linear Problems

The two problems presented here in are given in Nardi and Leonel (2023). In this work, besides the elastic analysis, a reliability approach is also performed. However, for sake of simplicity, only the deterministic analysis is presented herein. The first problem is a dam with three different materials, while the second one is a concrete tunnel under uniform pressure. The results are compared with those obtained by the ANSYS © software.

Figure 24 – (a)Dam composed of three different materials: transition, clay and rockfill and (b) FEM mesh in Ansys©.


(a)

(b)
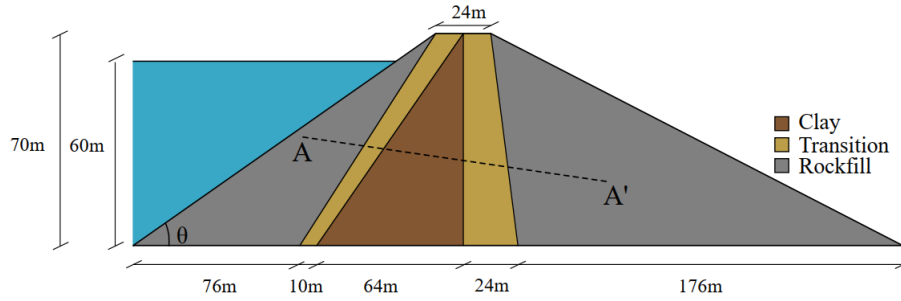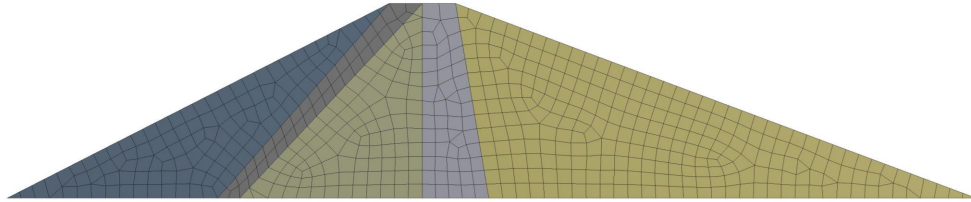
Source: Nardi and Leonel (2023).

5.1.1   Multi-material dam

The dam draws inspiration from the original section K of the Itaipu Binational Dam (ITAIPU, 2023). It comprises three distinct materials distributed across five subregions: rockfill, clay, and a transitional zone, as illustrated in Figure 24a. The dam section stands at a height of 70 meters and extends for a length of 350 meters, facing a water level of $H = 60$ meters. The material properties include: transition material, $E = 240MPa$, $\nu = 0.375$, $\gamma = 1800kg/m^3$; for the clay, $E = 50MPa$, $\nu = 0.35$, $\gamma = 1500kg/m^3$; and for the rockfill, $E = 35000MPa$, $\nu = 0.2$, $\gamma = 2000kg/m^3$. The dam is subjected to the following hydrostatic pressure:

$$\begin{bmatrix} \rho g h & 0 \\ 0 & \rho g h \end{bmatrix} \begin{Bmatrix} n_x \\ n_y \end{Bmatrix} = \begin{Bmatrix} t_x \\ t_y \end{Bmatrix} \tag{5.1}$$

in which $\rho = 1000kg/m^3$ is the water density, $g = 9.81m/s^2$ is the gravity acceleration, h is the water level, n_x and n_y are the components of the normal vector to the boundary and t_x and t_y are the tractions components. The water level, denoted as h, varies depending on the collocation point position. Consequently, a pre-processing step is necessary for applying boundary conditions. The definition of the water level is defined as follows:

Figure 25 – Principal stress and strain along the path $A - A'$.
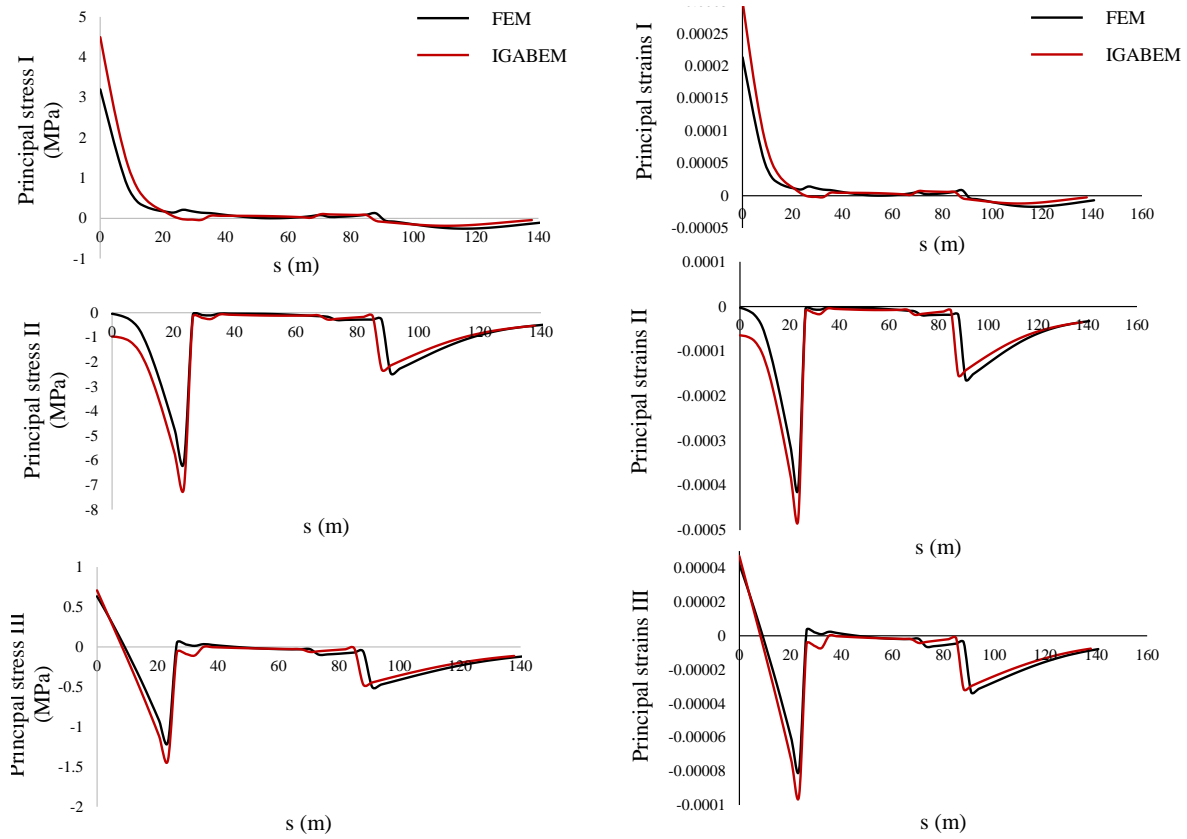
Source: Nardi and Leonel (2023).

$$h = H - y(\xi) \tag{5.2}$$

where H is the water level, y is the collocation point position that depends on the parametric coordinate ξ.

The dam is discretized with 18 linear NURBS, with a total of 510 control points. For comparative purposes, the dam is modeled in ANSYS© with 571 elements of $PLANE - 183$ type, with a total of 1842 nodes. The FEM mesh is presented in Figure 24b. A plane strain state is considered, and mesh convergence studies were carried out for both IGABEM and FEM models.

Figure 26 illustrates the deformed configuration. The obtained results demonstrate a satisfactory alignment between the two numerical approaches. Furthermore, the zones displaying maximum displacements precisely align with areas primarily composed of clay material, which possesses the lowest elasticity modulus among the constituents, as expected.

A chosen internal path $A - A'$ is considered to evaluate the principal stress and

Figure 26 – Defomed configuration via FEM versus IGABEM.
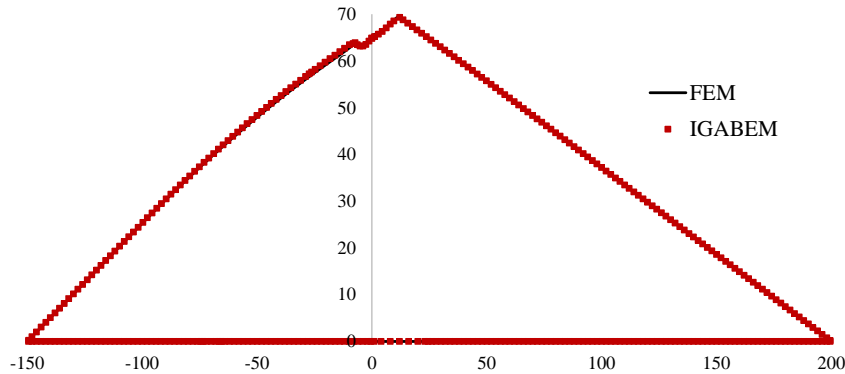
Source: Nardi and Leonel (2023).

strains. The path is presented in Figure 24, starting at $A = (-70, 35)m$ and ending at $A' = (70, 20)m)$. The results are presented in Figure 25.

Concerning the principal stresses, the IGABEM analysis yields a maximum principal stress value of $\sigma_I = 4.4979MPa$, and a minimum of $\sigma_{II} = -7.1206MPa$. In the FEM analysis, the corresponding values are $\sigma_I = 3.2002MPa$ and $\sigma_{II} = -6.0714MPa$. A relative difference of 33.71% is observed for the maximum principal stress, and 15.904% for the minimum stress. The disparity can be attributed to the more effective representation of stress fields in IGABEM within discontinuity regions. This advantage stems from IGABEM's independence from a mesh domain, a feature not shared by FEM. Thus, for approximating the results between the two methods, a more refined mesh for the FEM analysis would be required.

5.1.2 Concrete tunnel under uniform pressure

This example refers to a tunnel excavated within a rock mass, depicted in Figure 27a. The tunnel, constituting the first subregion, measures 10 meters in width and 5 meters in height, situated 25 meters below the ground (second subregion). It features an external radius, r_e, of 6 meters and an internal radius, r_i, of 5 meters. The concrete tunnel possesses a Young's modulus of 15 GPa and a Poisson ratio of 0.3. The surrounding rock soil mass has a Young's modulus of 13 GPa and a Poisson ratio of 0.12. The tunnel is subjected to a uniform pressure of $q = 1kPa$.

For the analysis, a plane strain state is considered. In IGABEM, 15 NURBS are used to discretize the tunnel, where 13 are linear and 2 are quadratic. A total of 237 control points are used. Again, for comparative reasons, the tunnel is modeled in ANSYS© with 8638 $PLANE - 183$ elements, totaling 26317 nodes. The FEM mesh is presented in

Figure 27 – (a) Concrete tunnel in an elastic medium and (b) BEM boundary conditions representation.

(a)   (b)
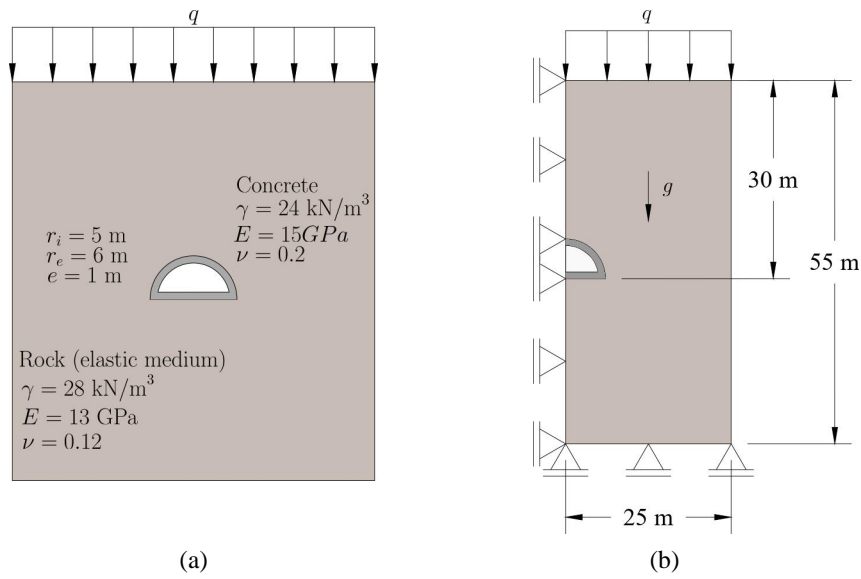
Source: Nardi and Leonel (2023).

Figure 28 – (a) Comparative displacements values in x and y direction and (b) tunnel deformed configuration via FEM and IGABEM.

(a)   (b)
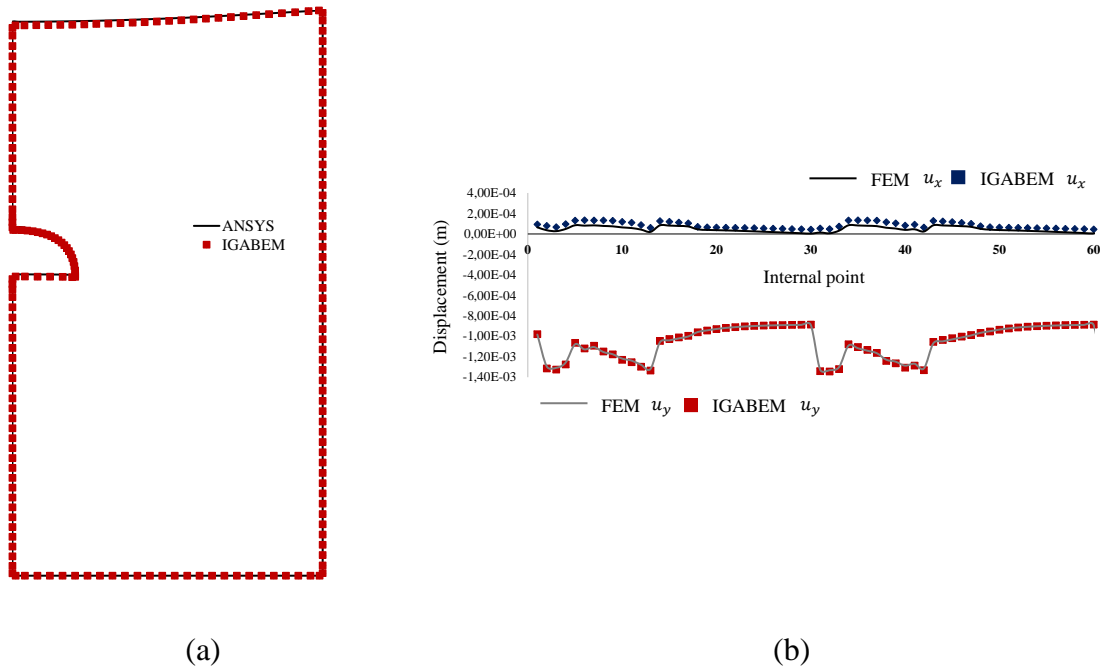
Source: Nardi and Leonel (2023).

Figure 29a.

Figure 29 – (a) FEM mesh and (b) internal path for the concrete tunnel.

(a)   (b)

Source: Nardi and Leonel (2023).

An internal path crossing through the tunnel is selected for evaluating displacements in both directions, as presented in Figure 29b. The path encompasses 62 points, starting at coordinates $(0.3935m, 5.2907m)$ and ending at coordinates $(0.3937m, -0.6691m)$. The deformed configuration is il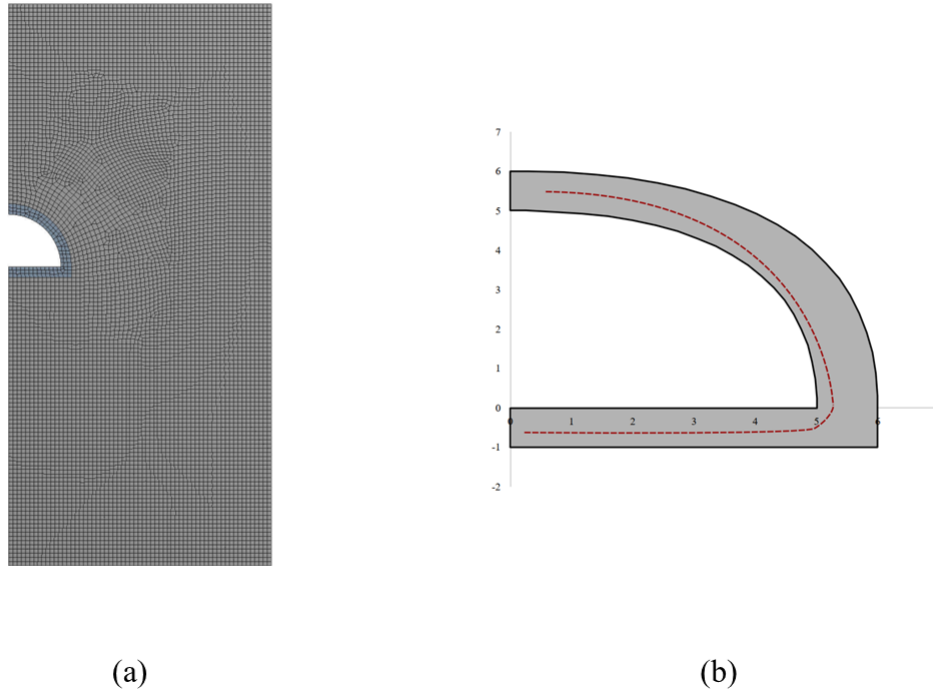lustrated in Figure 28a. The displacement results are presented in Figure 28b. Therefore, similar to the preceding example, the results indicate a strong agreement between the two methods.

Therefore, the achieved results for both illustrative examples underscore the efficacy of IGABEM and the extra employed numerical techniques. This allows a step forward in advancing the applicability of BEM to a broader range of problems, including nonlinear ones. With the linear stage well-consolidated, the next section presents the results of three nonlinear problems, showcasing the outcomes of coupling XLDM with IGABEM.

5.2   Nonlinear Problems

The problems presented in this section form the central focus of this dissertation. Here, the set of tools and techniques developed in the previous chapters are applied to solve three nonlinear problems, where the damaging process as well as the softening phase of each problem are observed through the adopted constitutive model, the XLDM.

The outcomes highlight the effectiveness of two primary challenges tackled in this work: evaluating the accuracy of the cells and the regularized kernels containing the domain effects, and assessing the effectiveness of the implemented predictor-corrector algorithm outlined in Algorithm 2.

An AMD Ryzen 9 7950X with 64GB RAM computer performs the numerical simulations with OpenMP directive for its parallelization. The parallelized subroutines involve the assembly of the following matrices: firstly, the matrix $\mathbf{Q}$ (refer to Eq. (3.7)) is assembled, incorporating influence terms arising from the integration of the kernel ε_{ijk}^*; following, the assembly includes $[\mathbf{H}]'$ and $[\mathbf{G}]'$ for calculating internal displacements; finally, the last matrix, $[\mathbf{Q}]'$, is also assembled to the posterior calculation of the internal displacement field (see Eq. (3.8)).

In this way, the first example, a square plate under uniform displacement, is the initial test for the proposed methodology. The second example, an L-shaped plate, is a benchmark test since there are numerical results considering the XLDM approach in the literature. Moving on to the third problem, a three-point bending beam, it stands as a classical benchmark test for fracture mechanics problems. The results of the first two problems are compared against the findings from FEM analysis presented in Teles (2022), as well as the experimental responses available in the literature. The three point bending beam serves as a showcase example, with outcomes compared to those provided by Saleh *et al.* (1997). Finally, for exploring the advantages of the Isogeometric approach, the last example addresses a problem involving a curved geometry, with results compared with those obtained by Lu *et al.* (2021).

For all the problems, the global criteria for convergence is:

$$\frac{\left\|\vec{\Delta u}_{\text{int }i}\right\|}{\|\vec{u}_{\text{ini}}\|} \leq tol \tag{5.3}$$

where $\|\vec{\Delta u}_{\text{int }i}\|$ is the norm of the internal displacement in the load step i, $\|\vec{u}_{\text{ini}}\|$ is norm of the initial displacement vector and *tol* is the tolerance value, defined in each case. The damage tolerance is settled to be equal to 10^{-8} for all the cases.

5.2.1 Square Under Uniform Displacement

This first illustrative example refers to a 250x250mm square plate under a prescribed uniform displacement field. The results are compared with those obtained by the FEM methodology provided in Teles (2022). In order to test the accuracy of the implemented cells, a domain evolutive convergence analysis is carried out. For this, the mesh is refined, starting with 1 cell covering the entire domain and then doubling the number of cells in each analysis. This refinement is essential to assess the accuracy of the new kernels related to the domain integral, which includes the initial stress field term. The consideration of

Figure 30 – Square plate under uniform displacement: meshes and boundary conditions.
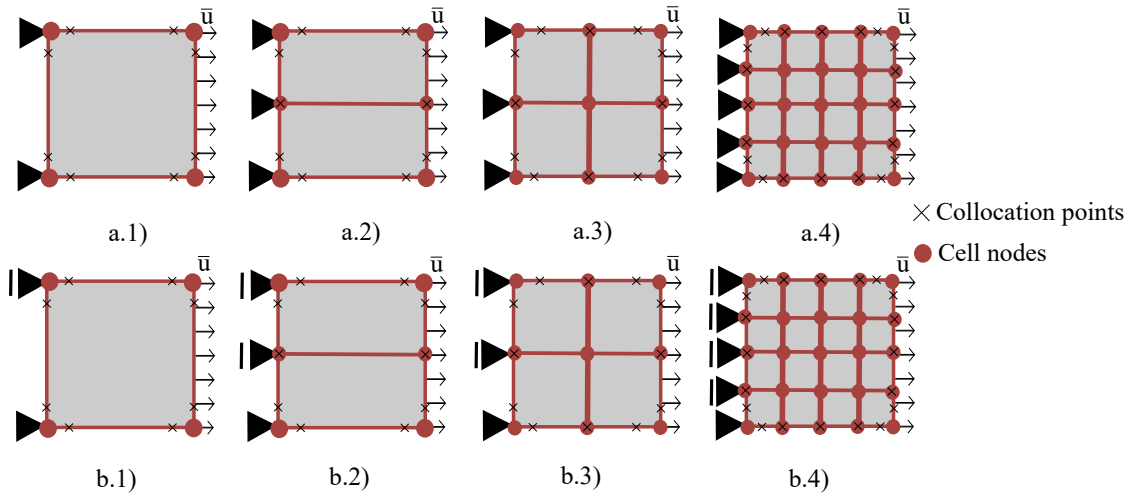
Source: The author.

the initial stress field allows the nonlinear behaviour of the material to be captured, as the damage propagates.

Therefore, Figure 30 shows the meshes used in the analysis, with 1, 2, 4 and 16 cells, respectively. The considered material properties are $E = 25850MPa$, $\sigma_{cr} = 2.7MPa$ and $q = -5mm^{-1}$. The analysis is performed for both Poisson values equal to $\nu = 0.0$ and $\nu = 0.3$. The prescribed displacement value is $\bar{u} = 1mm$. The boundary conditions are shown in Figure 30.

The implemented code initially identifies each cell node is situated on the boundary as well as those within the domain. For those nodes on the boundary, the code verifies if it coincides with a collocation point. If so, the collocation point displacement value is assigned to the cell node displacement. Otherwise, in case the node lies on the boundary and it does not coincide with a collocation point, as in an edge, for example, the displacement value is obtained by interpolation of the nearest collocation point values. For those inside the domain, the relation shown in Eq. (3.13) is used to obtain the internal displacement value.

In sequence, an incremental procedure is performed. The predictor corrector algorithm shown in Algorithm 2 is used to obtain the unknown fields. The global tolerance adopted for this example is 10^{-6}. Given that in BEM these unknown fields represent both traction and displacement, a post-processing step is undertaken upon algorithm convergence. This post-processing involves obtaining the resulting force in each case, as determined by the following relationship:

$$R = \int_\Gamma t_k d\Gamma \tag{5.4}$$

where R is the resultant force, t_k is the traction field in direction k and Γ is the boundary of the domain. Numerically, the above integral is approximated by:

$$R = \sum_{i=1}^{ng} \phi_i\left(\xi_i\right) t_k^i J\left(\xi_i\right) w_i \tag{5.5}$$

in which n_g is the number of Gauss points, ϕ_i is the shape function, ξ_i is the Gauss point position, t_k^i is the traction field in direction k at the Gauss point i, $J\left(\xi_i\right)$ is the Jacobian of transformation and w_i is the Gauss weight.

Therefore, the force-displacement relationship is shown in Figures 31 and 32. The results are compared to those obtained by a FEM analysis (Teles (2022) methodology), using the same mesh. Additionaly, the band thickness opening for each case is presented in Figures 33 and 34. One can observe that when $v = 0.3$ and the boundary condition is fixed-fixed, the damage tends to concentrate near the supports, as expected. In other cases, however, the damage is more uniformly distributed. Although XLDM treats concentrated damage, this outcome is expected due to the cells positioned throughout the domain, allowing for damage to be distributed across different regions, particularly in this pure traction case.

The results show a good agreement between the two methods. Notably, in both FEM and IGABEM analyses, the bands exhibit consistent thickness. This thickness decreases as the number of cells increases. Moreover, for the meshes where the boundary condition is fixed-fixed and $\nu = 0.3$, the bands tend to concentrate near the supports, assuming a maximum value of 0.99. Hence, the nonlinear effect due to damage propagation is effectively captured via the XLDM-IGABEM approach.

In conclusion, although this problem is quite simple and with a purely academic character, it has an exploratory nature, as the entire domain is discretized using cells. This enables the exploration of various cell sizes and different positions for cell nodes, offering the flexibility to match with a collocation point, an internal point, or not to match at all. In the subsequent examples, the focus is to discretize the domain in a minimal manner, where only the crack path is known in advance. This approach is feasible for a BEM analysis, as it avoids the need to discretize the entire domain, reducing significantly the computational cost. For instance, for the $a.4$ mesh with $\nu = 0.3$, the processing time is 13.5 seconds, while for the $b.4$ mesh $\nu = 0.3$, the processing time is 11.47 seconds.

Figure 31 – Force vs. displacement curves for the square plate under uniform displacement, for meshes a.1, a.2, b.1 and b.2, with $\nu = 0.0$ and $\nu = 0.3$.
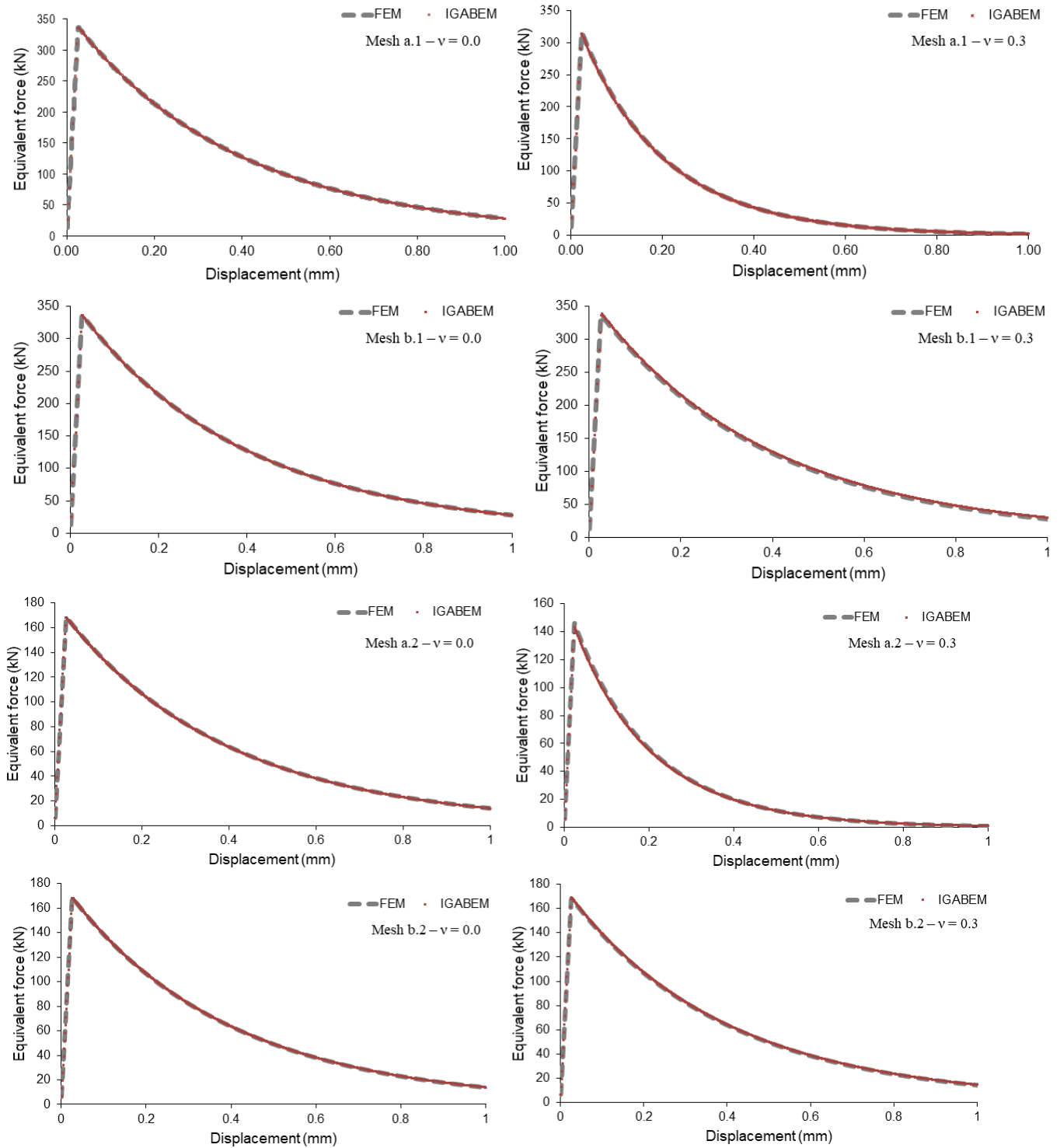
Figure 32 – Force vs. displacement curves for the square plate under uniform displacement, for meshes a.3, a.4, b.3 and b.4, with $\nu = 0.0$ and $\nu = 0.3$.
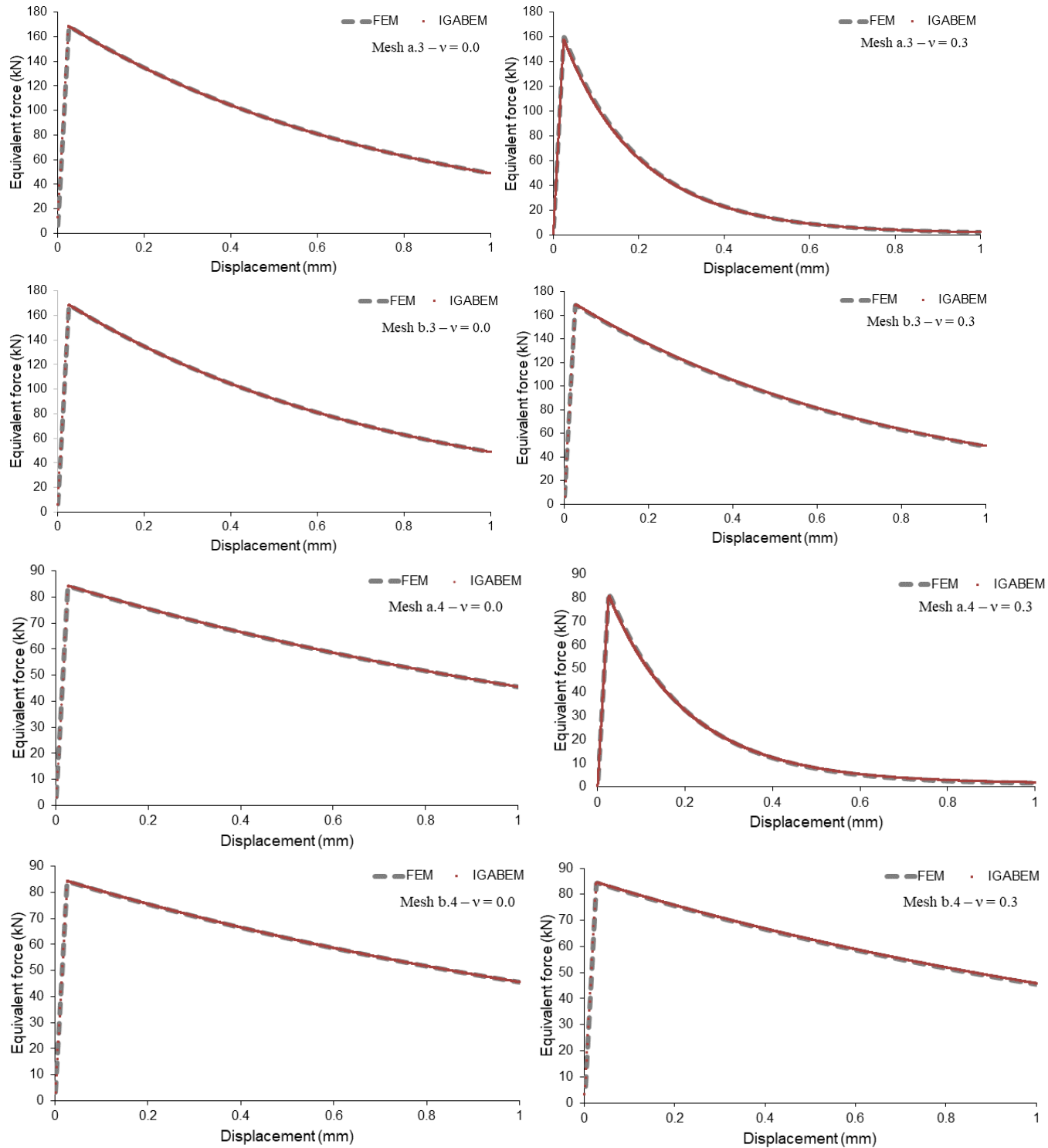
Source: The author.

Figure 33 – Band thickness opening for the square plate under uniform displacement, for the following meshes and Poisson values: (a) a.1 and b.1 for $\nu = 0.0$ and b.1 for $\nu = 0.3$; (b) a.1 for $\nu = 0.3$; (c) a.2 and b.2 for $\nu = 0.0$ and b.2 for $\nu = 0.3$; (d) a.2 for $\nu = 0.3$.

Band thickness in x direction (mm)

0.00   0.100   0.200   0.300   0.400   0.499

(a)

Band thickness in x direction (mm)

0.00   0.200   0.400   0.600   0.800   1.00

(b)

Band thickness in x direction (mm)

0.00   0.100   0.200   0.300   0.400   0.499

(c)

Band thickness in x direction (mm)

0.00   0.200   0.400   0.600   0.800   1.00

(d)
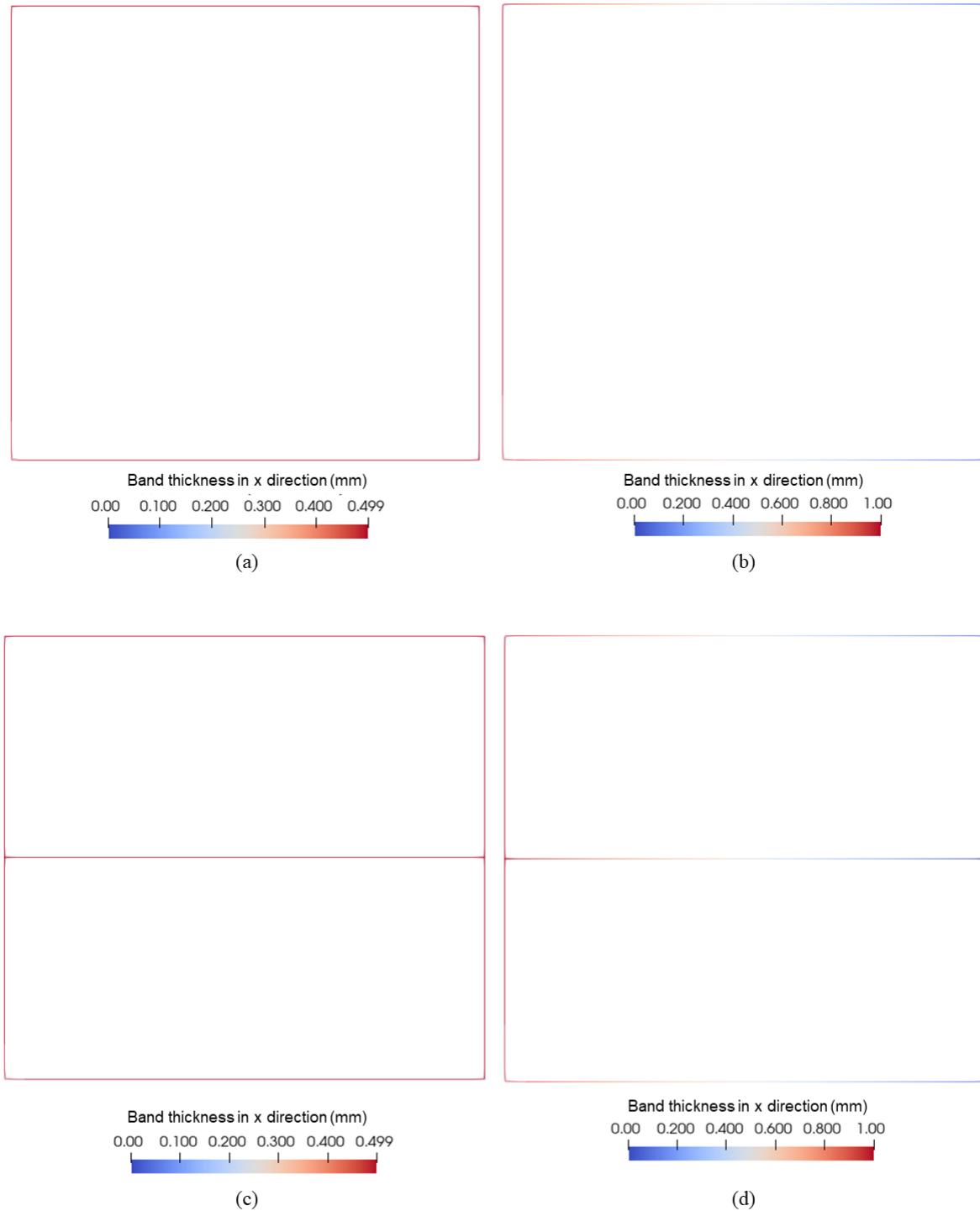
Source: The author.

Figure 34 – Band thickness opening for the square plate under uniform displacement, for the following meshes and Poisson values: (e) a.3 and b.3 for $\nu = 0.0$ and b.3 for $\nu = 0.3$; (f) a.3 for $\nu = 0.3$; (g) a.4 and b.4 for $\nu = 0.0$ and b.4 for $\nu = 0.3$; (h) a.4 for $\nu = 0.3$.

Band thickness in x direction (mm)

0.00 0.0500 0.100 0.150 0.200 0.248

(e)

Band thickness in x direction (mm)

0.00 0.200 0.400 0.600 0.800 0.999

(f)

Band thickness in x direction (mm)

0.00 0.0500 0.100 0.123

(g)

Band thickness in x direction (mm)

0.00 0.200 0.400 0.600 0.800 0.999

(h)
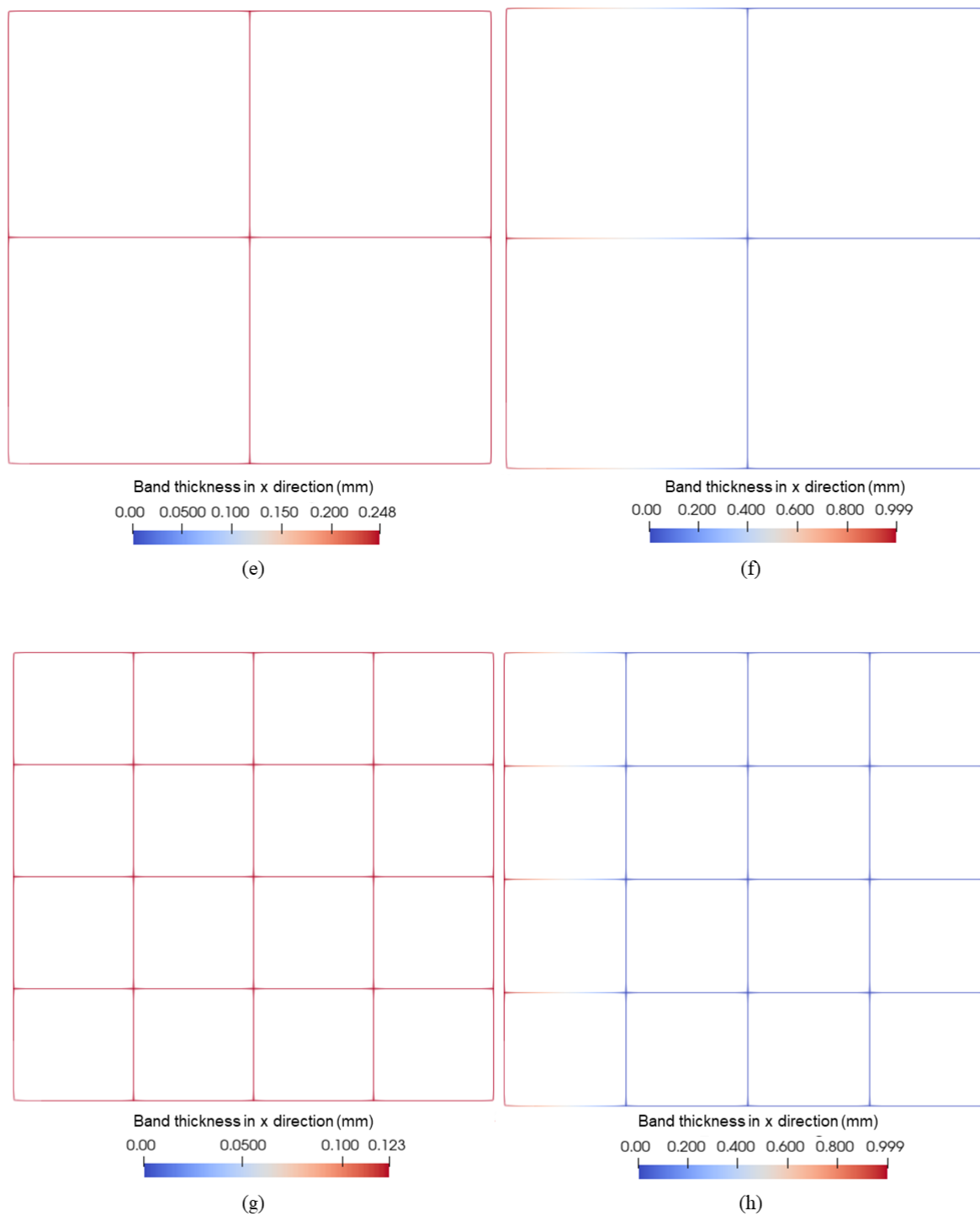
Source: The author.

5.2.2 L-Shaped Plate

This example corresponds to a benchmark test featuring an L-shaped structural member undergoing a prescribed displacement applied $30mm$ from its edge, as shown in Figure 35. The experimental results are provided by Winkler, Hofstetter and Niederwanger (2001). This problem has already been addressed via FEM using the XLDM in Teles (2022). As FEM is a mesh-based method, a convergence study was conducted in order to determine the optimal mesh for accurately capturing the damage propagation. In contrast, considering that IGABEM is a boundary-based method, the focus is on determining the optimal number of cells for analysis without the need to discretize the entire domain. In this context, only the crack path available in the reference is discretized by cells. This is feasible because this region is known a priori, as provided in the experimental results. Consequently, the cells can be strategically placed to ensure that the crack path is consistently contained within cells.

The material properties are $E = 20GPa$, $\nu = 0.18$, $\sigma_{cr} = 2.7MPa$, $q = -25mm^{-1}$, and the thickness is $100mm$. The structural member is discretized using 13 linear NURBS, comprising 213 control points. A plane stress state is considered. A controled displacement of $\overline{u} = 1mm$ is applied at the top left corner of the plate in incremental steps. The considered global tolerance is 10^{-4}.

Hence, a total of 10 meshes are studied, where one and two lines of cells are used to discretize the region where the crack evolves. The meshes are presented in Figure 36. The objective is to examine the convergence of results with varying cell numbers, with the aim of minimizing domain discretization and, consequently, maximizing the advantages offered by the boundary-based method.

Therefore, after post-processing the traction field, with the relations shown in Eqs. 5.4 and 5.5, the equivalent force at the location where the displacement is applied is obtained. The force-displacement curves are presented in Figure 37. As can be observed, convergence is achieved as the number of cells increases. However, nearly identical results are consistently obtained regardless the number of cell lines. This is attributed to the violation of internal stress values occurring within a well-defined region, delineated by the crack path. The XLDM constitutive model utilizes the opening of the band thickness to provide crucial insights into this phenomenon. For better understanding, the thickness of the localization band is presented in Figure 38. The band thickness values are higher near the corner and decrease as the crack propagates. This is expected, as the damage is concentrated near the crack tip. The maximum value is 0.51, which is consistent with the results obtained by Teles (2022). The total processing time for the case with 32 cells in one line is 194.83 seconds.
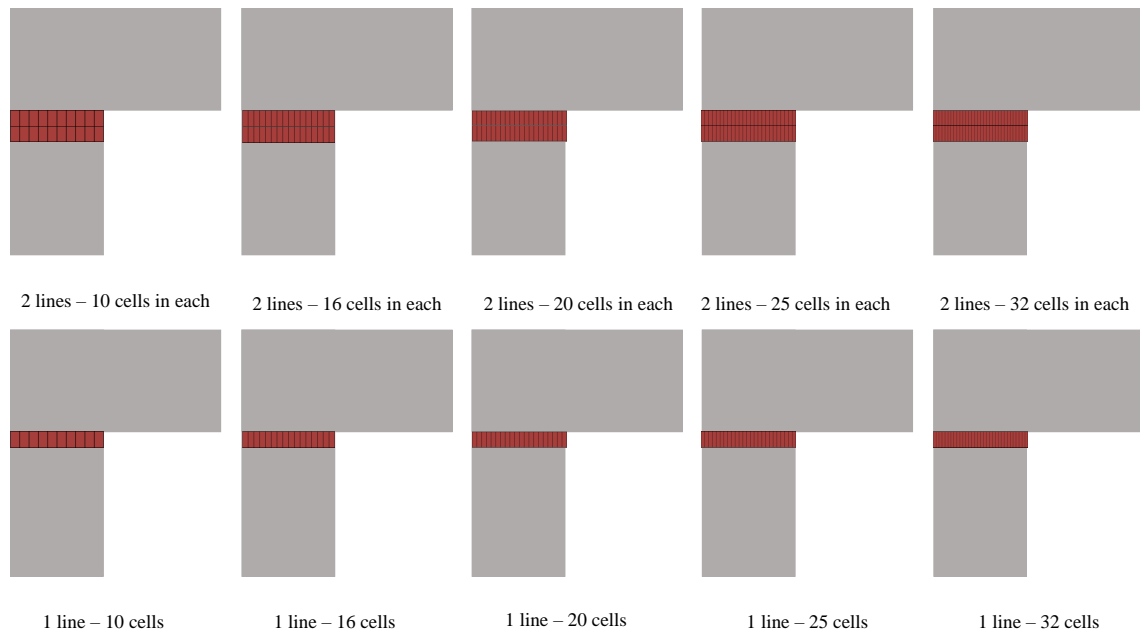
Furthermore, both the force-displacement relationship and the band thickness

Figure 35 – L-shaped structural member: test set-up.
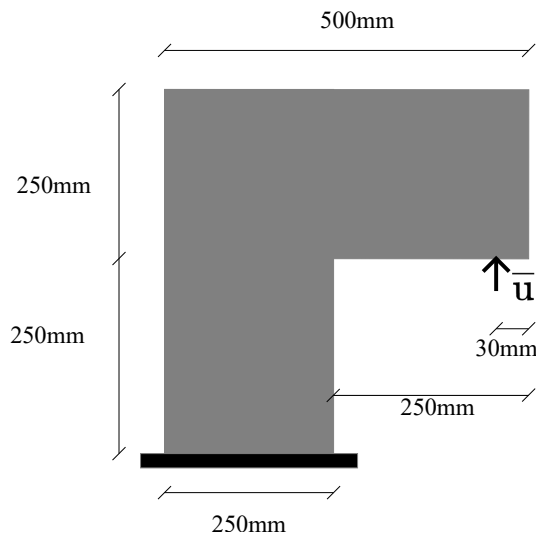
Source: Adapted from Winkler, Hofstetter and Niederwanger (2001).

Figure 36 – L-shape meshes: one and two lines of cells, from 10 to 32 cells.

2 lines – 10 cells in each   2 lines – 16 cells in each   2 lines – 20 cells in each   2 lines – 25 cells in each   2 lines – 32 cells in each

1 line – 10 cells   1 line – 16 cells   1 line – 20 cells   1 line – 25 cells   1 line – 32 cells

Source: The author.

values are in good agreement with the results provided by a FEM analysis in Teles (2022). The results demonstrate the effectiveness of the initial stress field approach via BEM with the adopted constitutive model. Undoubtedly, the most compelling aspect and key advantage of the proposed model is its ability to yield accurate results with a minimal domain mesh. This is advantageous for the BEM community as it enables the method

Figure 37 – Force vs. displacement curves for the L-shaped plate under uniform displacement.
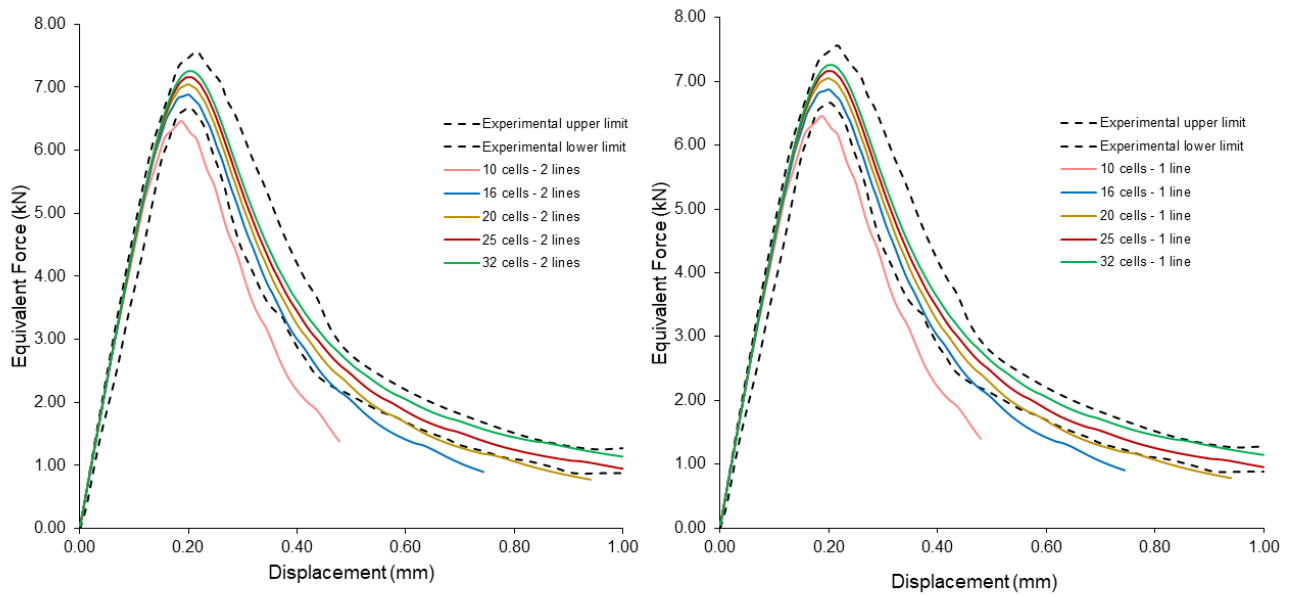
Source: The author.

Figure 38 – Band thickness opening for the L-shaped plate under uniform displacement.
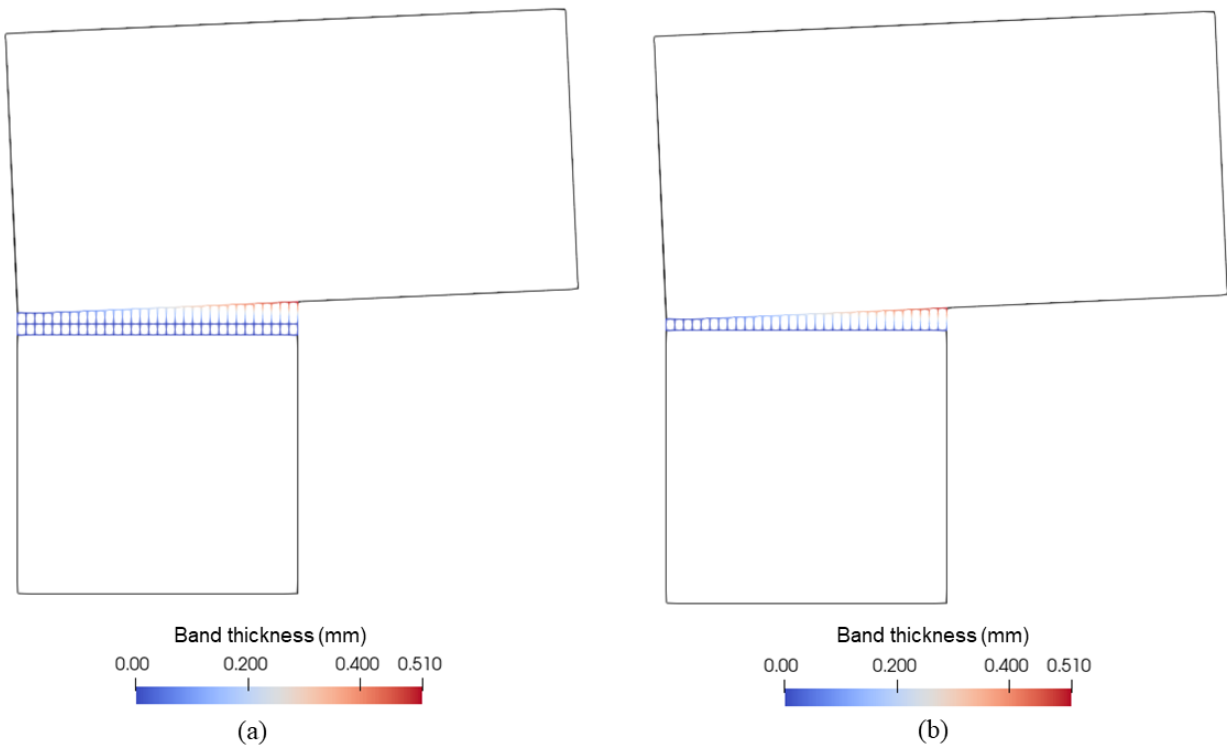
Source: The author.

to be employed in a broader spectrum of problems without requiring extensive domain discretization. It aligns seamlessly with the inherent nature of a numerical method that is naturally boundary-based, thereby eliminating contradictions that may arise when extensive domain discretizations are required.

5.2.3 Three-Point Bending Beam

The example provided in Saleh *et al.* (1997) is a benchmark test for fracture mechanics problems. The beam is subjected to a three-point bending test, as shown in Figure 39. The notch is $l = 50mm$ long. For the numerical modeling, an investigation was conducted on both the notch size and the region where the boundary conditions are applied. This was achieved by calibrating the linear elastic regime based on the reference response. A lenght $a = 40mm$ for the boundary conditions application and a notch length of $b = 8mm$ yielded the most accurate results and was consequently adopted for subsequent analyses.

Figure 39 – Three-point bending beam: test set-up.
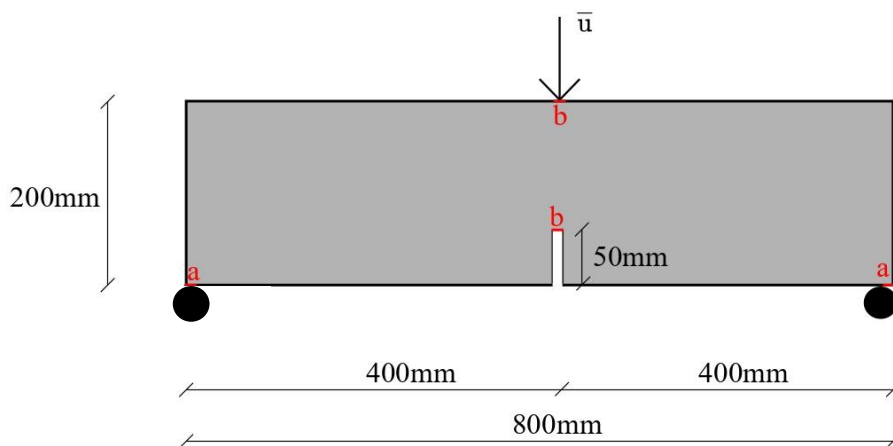
Source: Adapted from Saleh *et al.* (1997).

The considered material properties are: $E = 30GPa$, $\nu = 0.15$, $\sigma_{cr} = 3MPa$, $G_f = 0.075N/mm$ and the thickness is $1000mm$, as given in Saleh *et al.* (1997). A plane stress state is considered. A global tolerance of 10^-4 is adopted. The damage parameter q is computed based on Eq. (4.23), as follows:

$$q = -\frac{\sigma_{cr}}{G_f} = \frac{3 \text{ N/mm}^2}{0.075 \text{ N/mm}} = -40 \text{ mm}^{-1} \tag{5.6}$$

An incremental vertical load at the top mid-point of the beam is applied, using the displacement control method. The final displacement value is $\bar{u} = 0.21mm$. The beam is discretized using 12 linear NURBS, totalling 452 control points. For capturing the nonlinear

Figure 40 – Three-point bending beam: mesh illustrating the two lines of cells.
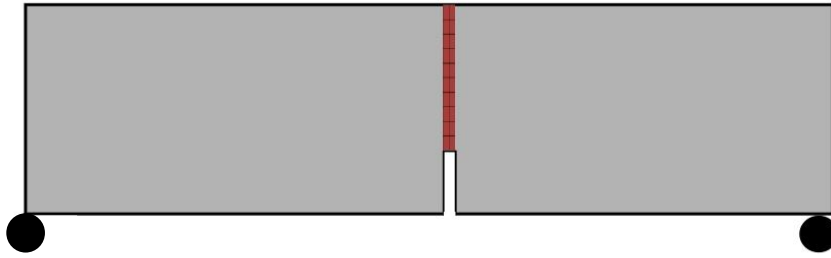
Source: The author.

behavior, once again the domain mesh is chosen to be minimal. In this example, similar to the previous one, the crack path is predetermined: here it is known due to the notch existence. It is located at the center of the beam, displaying higher values at the notch border that gradually decrease as it approaches the point of displacement application.

Convergence studies were conducted to determine the optimal number of cells. Meshes with 40, 80, 160 and 200 cells were analyzed. It was observed that the results became consistent from 160 cells onwards. In Figure 40, for the sake of simplicity, only the two lines of cells discretization are illustrated, each with a generic number of cells.

This example has been a classical benchmark test for fracture mechanics problems. The works from Oliveira (2017), Rocha (2020), Cordeiro (2018), Andrade (2017) and Neto (2023), for instance, have already addressed this problem via BEM considering cohesive models. The results obtained herein are in good agreement with those provided by the aforementioned works.

Hence, the equivalent force versus displacement relationship at the point of displacement application is presented in Figure 41 for the studied meshes, comparing the results with those obtained by Saleh *et al.* (1997) and by Andrade (2017). It is noteworthy to highlight that in the original work by Saleh *et al.* (1997), the presented curve considers a linear cohesive law, while in the curve given by Andrade (2017) and herein presented, it is exponential. This explains why the results obtained through the coupling of XLDM-IGABEM exhibit a better fit with those from Andrade (2017), given that the damage law employed in this study, as proposed by Teles (2022), is characterized by an exponential function. This outcome is significant as it demonstrates the effectiveness of the employed methodology.

In addition, the results show the crack path through the band thickness opening, as illustrated in Figure 42 for the mesh holding 160 cells. It is possible to note that the bands tend to open on the right-hand side of the beam, as expected due to the considered boundary condition application on this side. The higher values (0.144) are concentrated

Figure 41 – Comparison of the force-displacement curves for the three-point bending beam as the number of cells increases.
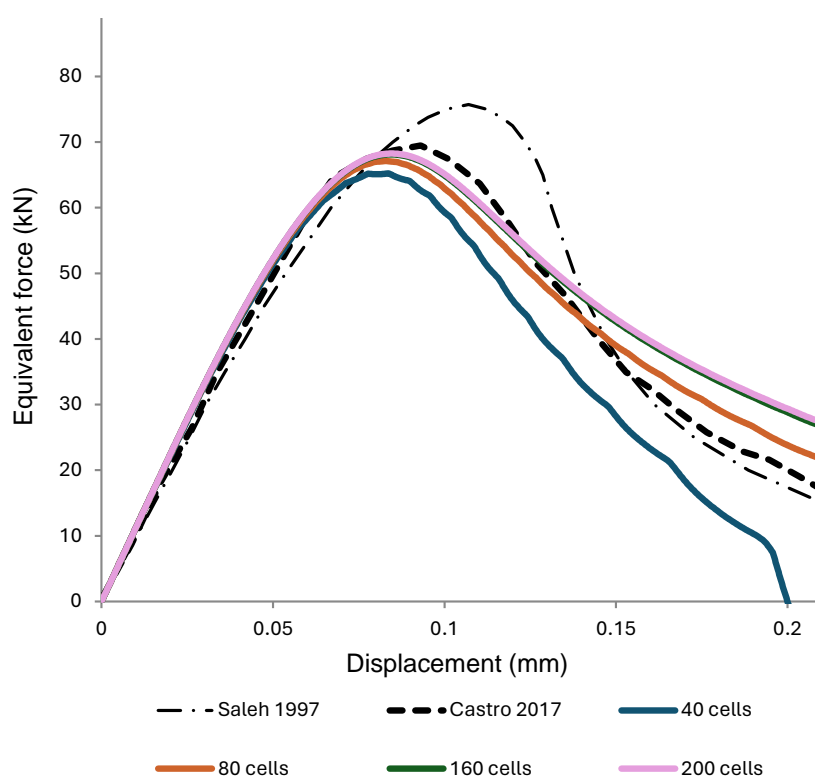
Source: The author.

near the notch, gradually decreasing in direction to the point of displacement application.

In conclusion, Figure 43 illustrates the stress versus band thickness opening for the case with a mesh of 160 cells. This result closely resembles the Crack Opening Displacement (COD) measure used in fracture mechanics to quantify the crack opening. The specific cell analyzed in this result corresponds to the one containing the highest band thickness opening value, i.e, the cell positioned at the notch border on the right-hand side of the beam. As can be noted, the stress values decrease as the band thickness opening increases, demonstrating the loss of resistence as the damage propagates.

Figure 42 – Band thickness opening for the three-point bending beam.
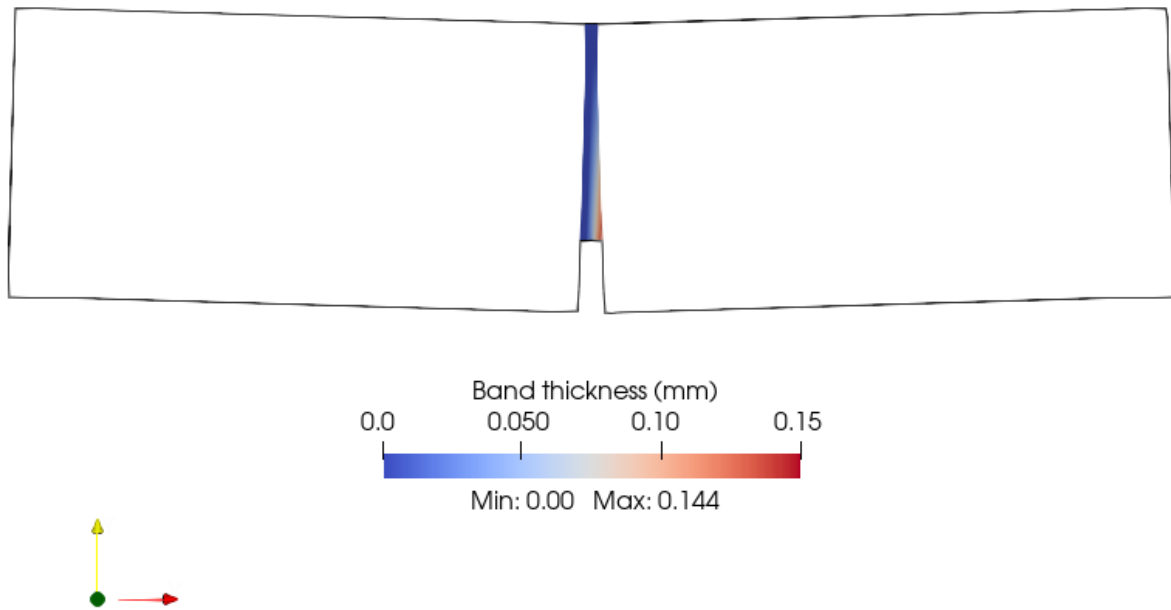
Source: The author.

Figure 43 – Stress at the notch border versus the band thickness opening for the three-point bending beam.
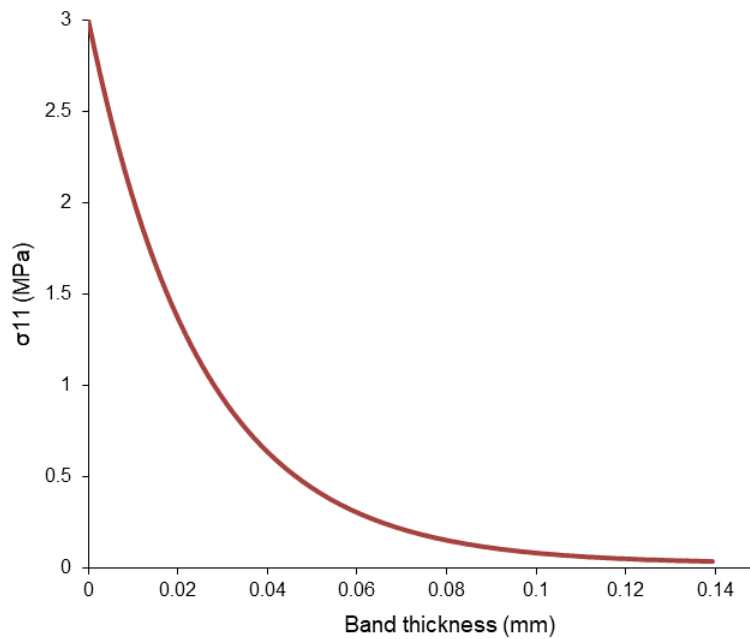
Source: The author.

5.2.4   Semi-circular Bending Test

To explore the advantages of isogeometric analysis within the framework presented herein, an example considering a curved surface is addressed. The study conducted by Lu *et al.* (2021) provides both experimental and numerical findings for a semi-circular bending test. This test is considered a well-established method for evaluating the cracking behavior of asphalt concrete mixtures. In this sense, the problem consists of a semi-circular specimen subjected to a three-point bending test, as illustrated in Figure 44. The authors employ a 3D Discrete Element Method (DEM) formulation to numerically evaluate the cracking evolution, with the provided experimental results serving to validate the numerical outcomes.

Figure 44 – Semi-circular bending test: test set-up.

Source: The author.

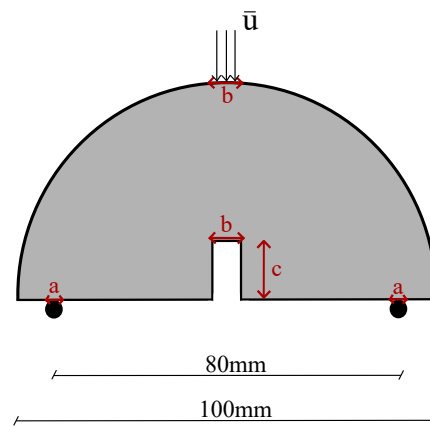The semi-circular specimen is discretized using 12 NURBS, 2 of which are quadratic, resulting in a total of 340 control points. The NURBS lenghts *a* and *b* for the boundary conditions application are $8mm$ and $2mm$, respectively. The authors investigate the influence of the notch lenght *c*, assuming values equal to $5mm$, $10mm$, $15mm$ and $20mm$.

Additionally, as per the findings of Lu *et al.* (2021), the material properties are adopted as follows: $E = 61MPa$, $\nu = 0.42$, $\sigma_{cr} = 0.45MPa$, $q = -1.50mm^{-1}$ and the thickness is $30mm$. The prescribed displacement value is $\bar{u} = 2.475mm$. Important to mention is that the extended lumped damage parameters σ_{cr} and q are adopted through a calibration process to best fit the experimental results. A total of 640 cells distributed into 8 cell lines are used to discretize the domain. Just as in the previous examples, the crack path is known in advance, and the cells are strategically placed to ensure that the crack path is consistently contained within cells, as shown in Figure 45.

The force-displacement relationship is depicted in Figure 46 for the four different notch lengths. For comparison, three random experimental results selected by Lu *et al.*

Figure 45 – Chosen domain discretization containing 640 cells distributed into 8 cell lines.
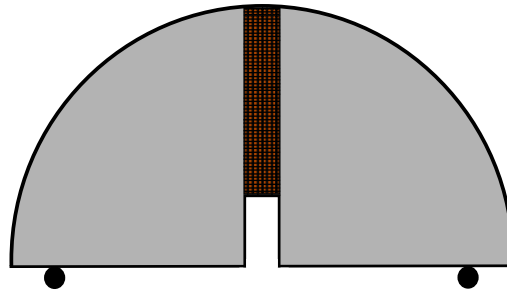
Source: The author.

Figure 46 – Force-displacement relationship for notch values equal to (a) $5mm$, (b) $10mm$, (c) $15mm$ and (d) $20mm$.
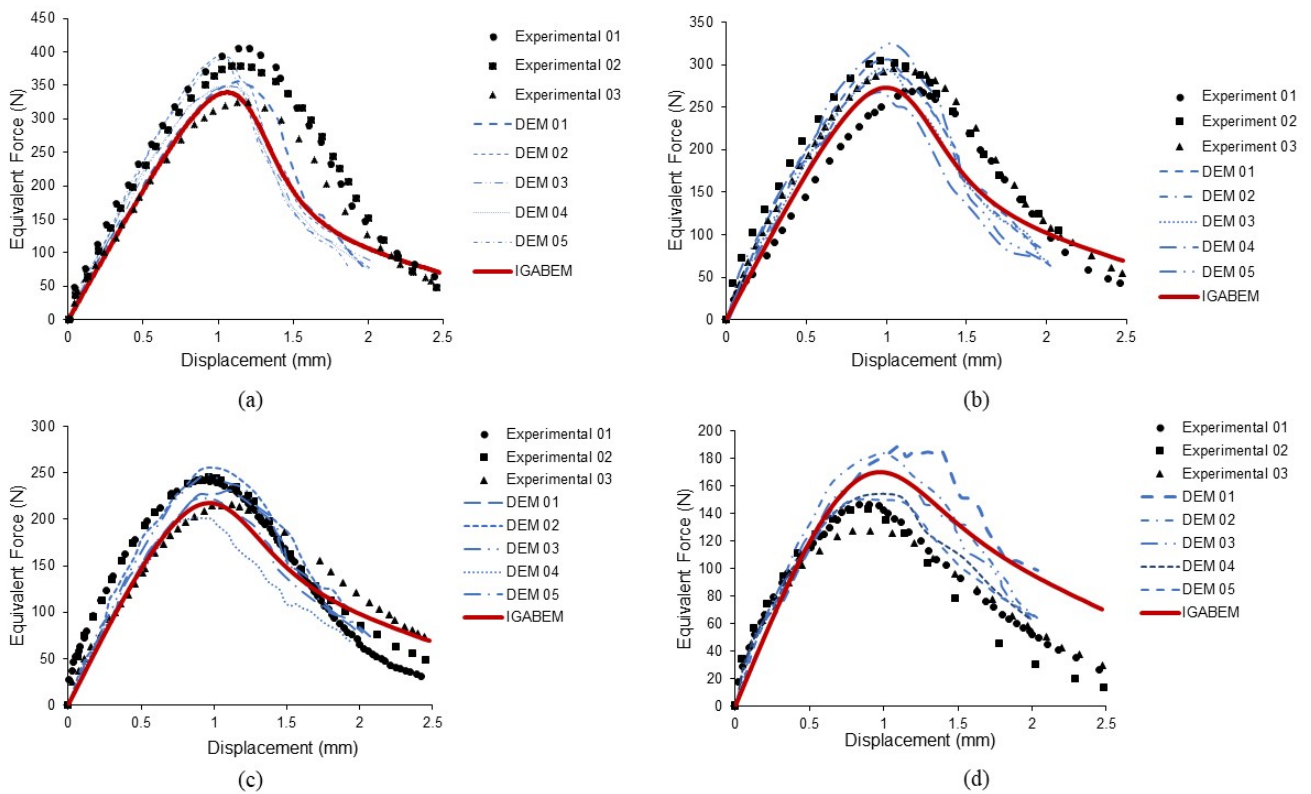
Source: The author.

(2021) are included, represented by the curves plotted in black. Furthermore, five numerical outcomes are represented by the curves in blue. These results vary among themselves due to the authors' consideration of the random arrangement of DEM particles. The outcomes provided by the XLDM-IGABEM approach show a good fit with the experimental results, particularly for the notch lengths $c = 5mm$, $c = 10mm$ and $c = 15mm$. The results

Figure 47 – Band thickness for notch values equal to (a) 5*mm*, (b) 10*mm*, (c) 15*mm* and (d) 20*mm*.
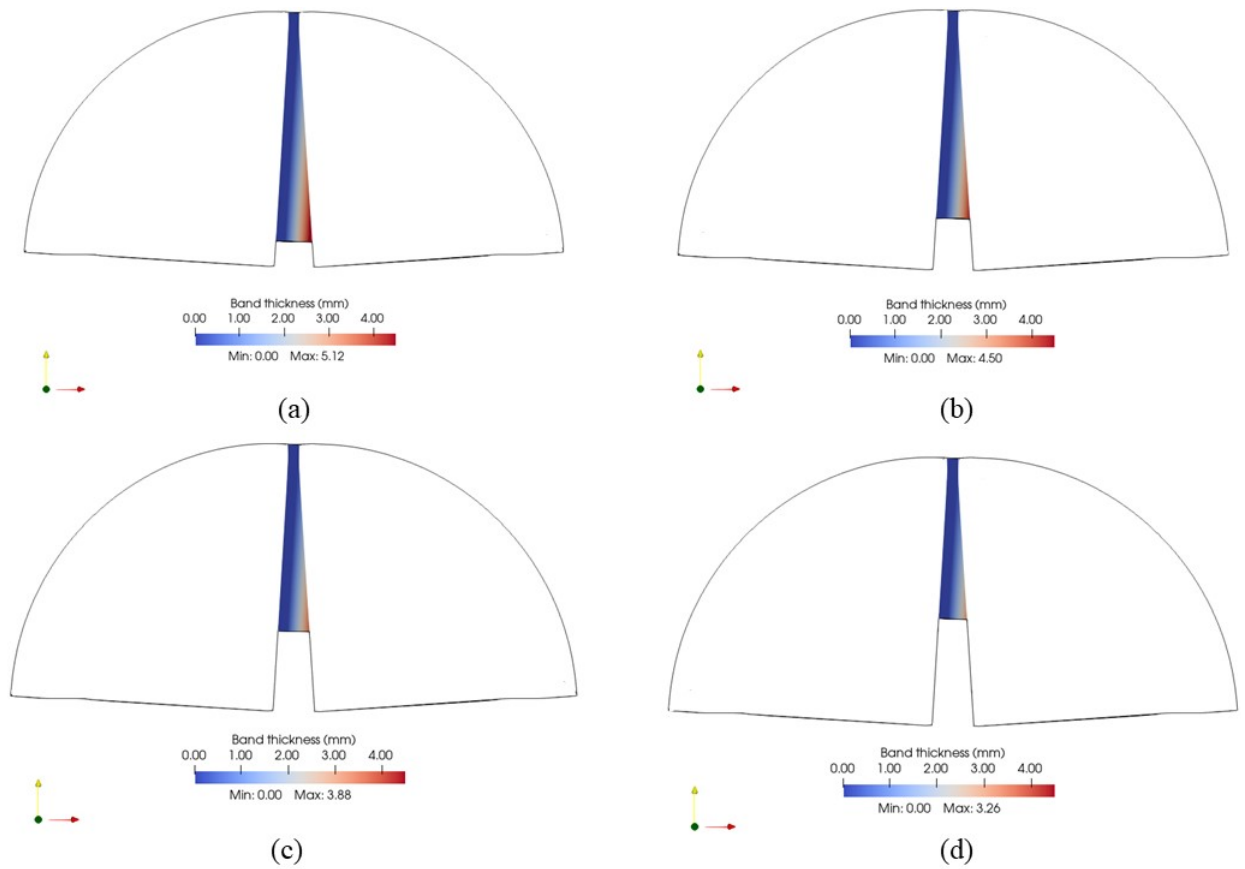
Source: The author.

for $c = 20mm$ are slightly less accurate, but still in good agreement with the author's numerical findings.

The band thickness opening for each notch length is presented in Figure 47. The results show that as the notch lenght increases, the band thickness opening decreases. The average computational time for this example is 10000 seconds, being the most time-consuming case among the examples presented in this work. This is due to the large number of cells used to discretize the domain.

In conclusion, the outcomes achieved through the XLDM-IGABEM method are in good agreement with both the experimental and numerical results presented by Lu *et al.* (2021). This particular example explores the advantages of isogeometric analysis within the framework presented herein. The use of NURBS functions enables precise representation of curved and conical surfaces, resulting in more accurate approximations for both geometry and mechanical fields. In contrast, representing the same problem using traditional FEM analysis would necessitate a more complex mesh with a higher number of

elements and nodes. Therefore, the effectiveness of the proposed methodology in capturing the damage propagation in a curved surface is provided, giving rise to a new perspective for the application of BEM in a broader range of nonlinear problems.

6 CONCLUDING REMARKS

The present work contributes to advancing Boundary Element Method (BEM) formulations for damage mechanics problems. The use of BEM in this context is still incipient, as most of BEM formulations for this purpose adopt extensive domain discretizations, which are required to obtain acceptable accuracy. Therefore, the main advantage of BEM, i.e., the boundary only discretization, is lost when dealing with damage mechanics problems.

In this context, the present research proposes a novel boundary element formulation for modeling damage mechancis problems. Besides the use of an isogeometric analysis, which provides enhanced geometry and mechanical field representation, the proposed work also introduces the Extended Lumped Damage Mechancis (XLDM) consitutive model into an initial stress boundary element approach. The XLDM is a mesh independent model, which is advantageous since most damage models are ill-posed. The model captures the non-linear effect by replacing the kinematic variable: the band elongations are considered rather than directly using the strain values. Furthermore, the XLDM is also capable of capturing the softening behavior and the of circumventing the strain localization phenomenon, which are fundamental aspects for reproducing the structural failure behavior. It's crucial to emphasize that the XLDM has only been formulated within the Finite Element Method (FEM) framework. Therefore, the present research is the first to propose the use of the XLDM in the context of BEM. The proposed approach distinguishes itself by eliminating the requirement for full domain discretization, thereby making more interesting the use of BEM in the context of damage mechanics.

To couple XLDM within IGABEM, the displacement integral equation accounting for the initial stresses is applied. The domain discretization, requeried only at the damaged bands of the XLDM, is performed by considering discretizations with linear cells. From the cell nodal displacements, both the strains and elongations of the constitutive model are defined. A predictor-corrector algorithm is then proposed, effectively inserting the XLDM constituve model into the initial stress field BEM framework. The initial stress field integral equation contains a singular kernel, which is herein regularized by means of a polar integration followed by a subelementation of the parametric space.

The results obtained with the proposed formulation showed that it was possible to obtain a good fit between the present work and those available in the literature. Through a cell convergence study, the optimal number of cells required to obtain accurate results could be determined. The region where the band thickness evolves coincides with the most solicited region of the structure. The computational time required for the nonlinear analysis demonstrates that it tends to increase as the number of cells increases. This is expected

since domain discretization is usually costly in BEM. However, as in the examples herein presented the damage localization path was known a priori, the domain discretization was performed only where the inelastic behavior was expected to propagate. This is a limitation of the proposed approach for more complex cases, where the damage localization path is not always known. A recomendation for cases where the damage localization path is unknown is to carry out a linear elastic analysis to identify the region where the principal stresses are concentrated. This region would be the most solicited region of the structure and, therefore, the region where the cells should be placed.

6.1   Recomendations for future work

The current research development leaves certain aspects for future investigation. The following list presents some of the most relevant topics that can be addressed in the next contributions to this work:

- Non-linear analyzes in large scale problems, such as the dam example, could be performed. In massive structures, specially in large volume-to-boundary ratio problems, the use of BEM is suitable as no domain discretization is required. Hence, only the region where the crack is expected to propagate needs to be discretized with the cells;

- The automatic generation of cells could be implemented. The current implementation requires the user to manually define the cells. This is not a major issue for small problems, but it can become a time-consuming task for mesh generation in large scale problems;

- A tagent operator for the global convergence could be used instead of the constant one used in the present work. This would improve the convergence rate of the proposed algorithm.

REFERENCES

ALIABADI, M.; BREBBIA, C. Boundary element formulations in fracture mechanics: a review. **WIT Transactions on Engineering Sciences**, WIT Press, v. 13, 1970.

ALIABADI, M. H. **The boundary element method, volume 2: applications in solids and structures**. [*S.l.: s.n.*]: John Wiley & Sons, 2002. v. 2.

AMORIM, D. L. *et al.* The extended lumped damage mechanics: A new formulation for the analysis of softening with fe size-independence. **Mechanics Research Communications**, Elsevier, v. 91, p. 13–18, 2018.

AMORIM, D. L. d. F.; PROENÇA, S. P.; FLÓREZ-LÓPEZ, J. A model of fracture in reinforced concrete arches based on lumped damage mechanics. **International Journal of Solids and Structures**, Elsevier, v. 50, n. 24, p. 4070–4079, 2013.

AMORIM, D. L. N. de F. **On the lumped damage mechanics for nonlinear structural analyses: new developments and applications**. 2016. 195 p. Tese (PhD Degree) — Universidade de São Paulo, São Carlos, 2016.

ANDRADE, H. d. C. e. **Análise da propagação de fissuras em estruturas bidimensionais não-homogêneas via Método dos Elementos de Contorno**. 2017. 243 p. Dissertação (Mestrado) — Universidade de São Paulo, São Carlos, 2017.

ARMSTRONG, P. J.; FREDERICK, C. *et al.* **A mathematical representation of the multiaxial Bauschinger effect**. [*S.l.: s.n.*]: Berkeley Nuclear Laboratories Berkeley, CA, 1966. v. 731.

BAI, Y. *et al.* Macromodeling of crack damage in steel beams subjected to nonstationary low cycle fatigue. **Journal of Structural Engineering**, American Society of Civil Engineers, v. 142, n. 10, p. 04016076, 2016.

BAI, Y. *et al.* A new comprehensive model of damage for flexural subassemblies prone to fatigue. **Computers & Structures**, Elsevier, v. 256, p. 106639, 2021.

BARBIRATO, J. C. C. *et al.* Método dos elementos de contorno com a reciprocidade dual para a análise transiente tridimensional da mecânica do fraturamento. **São Carlos. Tese (Doutorado)-Escola de Engenharia de São Carlos-Universidade de São Paulo**, 1999.

BARBOSA, A. *et al.* Analysis of reinforced concrete structures using ansys nonlinear concrete model. Citeseer, 1998.

BATE, P.; WILSON, D. Analysis of the bauschinger effect. **Acta Metallurgica**, Elsevier, v. 34, n. 6, p. 1097–1105, 1986.

BAZÁN, J. A.; BECK, A. T.; FLÓREZ-LÓPEZ, J. Random fatigue of plane frames via lumped damage mechanics. **Engineering Structures**, Elsevier, v. 182, p. 301–315, 2019.

BEER, G.; DUENSER, C. Immersed isogeometric boundary elements: A user friendly method for the 3-d elasto-plastic simulation of underground excavations. **Computers and Geotechnics**, Elsevier, v. 157, p. 105330, 2023.

BEER, G. *et al.* Isogeometric boundary element analysis with elasto-plastic inclusions. part 1: plane problems. **Computer Methods in Applied Mechanics and Engineering**, Elsevier, v. 308, p. 552–570, 2016.

BEER, G.; SMITH, I.; DUENSER, C. **The boundary element method with programming: for engineers and scientists**. [*S.l.: s.n.*]: Springer Science & Business Media, 2008.

BOOR, C. D. On calculating with b-splines. **Journal of Approximation theory**, Academic Press, v. 6, n. 1, p. 50–62, 1972.

BOTTA, A. S. **Método dos elementos de contorno para análise de corpos danificados com ênfase no fenômeno da localização de deformações**. 2003. Tese (Doutorado) — Universidade de São Paulo, 2003.

BOTTA, A. S.; VENTURINI, W. S.; BENALLAL, A. Bem applied to damage models emphasizing localization and associated regularization techniques. **Engineering analysis with boundary elements**, Elsevier, v. 29, n. 8, p. 814–827, 2005.

BREBBIA, C. A.; TELLES, J. C. F.; WROBEL, L. C. **Boundary element techniques: theory and applications in engineering**. [*S.l.: s.n.*]: Springer Science & Business Media, 2012.

BREBBIA, C. A.; WALKER, S. **Boundary element techniques in engineering**. [*S.l.: s.n.*]: Elsevier, 2016.

CHENG, A. H.-D.; CHENG, D. T. Heritage and early history of the boundary element method. **Engineering analysis with boundary elements**, Elsevier, v. 29, n. 3, p. 268–302, 2005.

CIPOLLINA, A.; LÓPEZ-INOJOSA, A.; FLÓREZ-LÓPEZ, J. A simplified damage mechanics approach to nonlinear analysis of frames. **Computers & Structures**, Elsevier, v. 54, n. 6, p. 1113–1126, 1995.

COELHO, K. O. **Modelos numéricos aplicados à modelagem probabilística da degradação mecânica do concreto e corrosão de armaduras**. 2017. Tese (Msc Dissertation) — Universidade de São Paulo, 2017.

CORDEIRO, S. G. F. **Contribuições às análises de fratura e fadiga de componentes tridimensionais pelo método dos elementos de contorno dual**. 2018. Tese (Doutorado) — Universidade de São Paulo, 2018.

CORDEIRO, S. G. F.; LEONEL, E. D.; BEAUREPAIRE, P. Quantification of cohesive fracture parameters based on the coupling of bayesian updating and the boundary element method. **Engineering Analysis with Boundary Elements**, Elsevier, v. 74, p. 49–60, 2017.

COTTRELL, J. A.; HUGHES, T. J.; BAZILEVS, Y. **Isogeometric analysis: toward integration of CAD and FEA**. [*S.l.: s.n.*]: John Wiley & Sons, 2009.

COX, M. G. The numerical evaluation of b-splines. **IMA Journal of Applied mathematics**, Oxford University Press, v. 10, n. 2, p. 134–149, 1972.

FLÓREZ-LÓPEZ, J. Calcul simplifié de portiques endommageables. **Revue Européenne des élements finis**, Taylor & Francis, v. 2, n. 1, p. 47–74, 1993.

FLÓREZ-LÓPEZ, J.; MARANTE, M.; PICÓN, R. **Fracture and damage mechanics for structural engineering of frames: state-of-the-art industrial applications, Hershey**. [*S.l.: s.n.*], 2015. v. 10. 978–1 p.

GARCIA, R.; FLOREZ-LOPEZ, J.; CERROLAZA, M. A boundary element formulation for a class of non-local damage models. **International journal of solids and structures**, Elsevier, v. 36, n. 24, p. 3617–3638, 1999.

GHRIB, F.; TINAWI, R. Nonlinear behavior of concrete dams using damage mechanics. **Journal of Engineering Mechanics**, American Society of Civil Engineers, v. 121, n. 4, p. 513–527, 1995.

GREVILLE, T. N. Numerical procedures for interpolation by spline functions. **Journal of the Society for Industrial and Applied Mathematics, Series B: Numerical Analysis**, SIAM, v. 1, n. 1, p. 53–68, 1964.

HAIFENG, L.; JIANGUO, N. Mechanical behavior of reinforced concrete subjected to impact loading. **Mechanics of Materials**, Elsevier, v. 41, n. 12, p. 1298–1308, 2009.

HELTAI, L. *et al.* A natural framework for isogeometric fluid–structure interaction based on bem–shell coupling. **Computer Methods in Applied Mechanics and Engineering**, Elsevier, v. 316, p. 522–546, 2017.

HERDING, U.; KUHN, G. A field boundary element formulation for damage mechanics. **Engineering analysis with boundary elements**, Elsevier, v. 18, n. 2, p. 137–147, 1996.

HOSSEINI-TEHRANI, P.; ESLAMI, M. Bem analysis of thermal and mechanical shock in a two-dimensional finite domain considering coupled thermoelasticity. **Engineering Analysis with Boundary Elements**, Elsevier, v. 24, n. 3, p. 249–257, 2000.

HU, H.-T.; SCHNOBRICH, W. C. Nonlinear analysis of cracked reinforced concrete. **Structural Journal**, v. 87, n. 2, p. 199–207, 1990.

ITAIPU. Principais características técnicas. *In*: . [*S.l.: s.n.*]: Itaipu Binacional, 2023.

JOHNSON, R. W. Higher order b-spline collocation at the greville abscissae. **Applied Numerical Mathematics**, Elsevier, v. 52, n. 1, p. 63–75, 2005.

JUNIOR, E. T. d. L. **Formulação do método dos elementos de contorno para análise de cascas abatidas**. 2006. Tese (Doutorado) — Universidade de São Paulo, 2006.

JUNIOR, E. T. de L. **Isotropic damage phenomena in saturated porous media: a BEM formulation**. 2011. Tese (Doutorado) — École normale supérieure de Cachan-ENS Cachan; Universidade de São Paulo, 2011.

KACHANOV, L. Time of the rupture process of non-linear solid mechanics. **Otd. Tech. Nauk**, v. 8, p. 28–31, 1958.

KZAM, A. K. L. **Formulação dual em Mecânica da Fratura utilizando Elementos de Contorno curvos de ordem qualquer**. 2009. 202 p. Dissertação (Mestrado) — Universidade de São Paulo, São Carlos, 2009.

LEITAO, V.; ALIABADI, M.; ROOKE, D. Elastoplastic simulation of fatigue crack growth: Dual boundary element formulation. **International Journal of Fatigue**, Elsevier, v. 17, n. 5, p. 353–363, 1995.

LEMAITRE, J.; CHABOCHE, J.-L. **Mechanics of solid materials**. [*S.l.: s.n.*]: Cambridge university press, 1994.

LEONEL, E. D. Método dos elementos de contorno aplicado à análise de sólidos multi-fraturados. Biblioteca Digital de Teses e Dissertações da USP, 2006.

LEONEL, E. D.; VENTURINI, W. S.; CHATEAUNEUF, A. A bem model applied to failure analysis of multi-fractured structures. **Engineering Failure Analysis**, Elsevier, v. 18, n. 6, p. 1538–1549, 2011.

LEUNG, C. Concrete as a building material, encyclopaedia of materials. *In*: . [*S.l.: s.n.*]: Oxford, UK: Elsevier, 2001.

LI, K. *et al.* Isogeometric boundary element method for isotropic damage elastic mechanical problems. **Theoretical and Applied Fracture Mechanics**, Elsevier, v. 124, p. 103802, 2023.

LIANG, Z. *et al.* A three-dimensional numerical investigation of the fracture of rock specimens containing a pre-existing surface flaw. **Computers and Geotechnics**, Elsevier, v. 45, p. 19–33, 2012.

LU, D. X. *et al.* Experimental and numerical investigations of non-standardised semi-circular bending test for asphalt concrete mixtures. **International Journal of Pavement Engineering**, Taylor & Francis, v. 22, n. 8, p. 960–972, 2021.

MARANTE, M.; FLÓREZ-LÓPEZ, J. Model of damage for rc elements subjected to biaxial bending. **Engineering Structures**, Elsevier, v. 24, n. 9, p. 1141–1152, 2002.

MELLINGS, S.; BAYNHAM, J.; ADEY, R. A. Automatic crack growth prediction in rails with bem. **Engineering fracture mechanics**, Elsevier, v. 72, n. 2, p. 309–318, 2005.

MENDELSON, A. Boundary-integral methods in elasticity and plasticity. *In*: . [*S.l.: s.n.*], 1973.

MUKHERJEE, S. Corrected boundary-integral equations in planar thermoelastoplasticity. **International Journal of Solids and Structures**, Elsevier, v. 13, n. 4, p. 331–335, 1977.

NARAYAN, S.; ANAND, L. A gradient-damage theory for fracture of quasi-brittle materials. **Journal of the Mechanics and Physics of Solids**, Elsevier, v. 129, p. 119–146, 2019.

NARDI, D. C.; LEONEL, E. D. The probabilistic mechanical-material modeling of complex non-homogeneous structures using the coupling of isogeometric boundary element method and reliability approach. **Proceedings of the Institution of Mechanical Engineers, Part L: Journal of Materials: Design and Applications**, SAGE Publications Sage UK: London, England, p. 14644207231218166, 2023.

NETO, A. R. **Numerical formulations based on the Isogeometric Boundary Element Method for the mechanical analysis of three-dimensional reinforced nonhomogeneous solids**. 2023. Tese (Doutorado) — Universidade de São Paulo, 2023.

NIE, Z. *et al.* Stability analysis of landslides using bem and variational inequality based contact model. **Computers and Geotechnics**, Elsevier, v. 123, p. 103575, 2020.

OLIVEIRA, H. L. **Modelos numéricos aplicados à análise viscoelástica linear e à otimização topológica probabilística de estruturas bidimensionais: uma abordagem pelo Método dos Elementos de Contorno**. 2017. Tese (Doutorado) — Universidade de São Paulo, 2017.

OLIVEIRA, H. L.; LEONEL, E. D. Cohesive crack growth modelling based on an alternative nonlinear bem formulation. **Engineering Fracture Mechanics**, Elsevier, v. 111, p. 86–97, 2013.

PAN, E. A bem analysis of fracture mechanics in 2d anisotropic piezoelectric solids. **Engineering Analysis with Boundary Elements**, Elsevier, v. 23, n. 1, p. 67–76, 1999.

PANJI, M.; ANSARI, B. Modeling pressure pipe embedded in two-layer soil by a half-plane bem. **Computers and Geotechnics**, Elsevier, v. 81, p. 360–367, 2017.

PEIXOTO, R. G. Análise de degradaçao material, bifurcaçao e transiçao entre descontinuidades fracas e fortes através do método dos elementos de contorno. Universidade Federal de Minas Gerais, 2016.

PEIXOTO, R. G.; RIBEIRO, G. O.; PITANGUEIRA, R. L. A progressive cells activation algorithm for physically non-linear bem analysis. **Journal of the Brazilian Society of Mechanical Sciences and Engineering**, Springer, v. 40, p. 1–13, 2018.

PELLIZZER, G. P. **Análise mecânica e probabilística da corrosão de armaduras de estruturas de concreto armado submetidas à penetração de cloretos**. 2015. Tese (Doctoral thesis) — Universidade de São Paulo, 2015.

PIEGL, L.; TILLER, W. **The NURBS book**. [*S.l.: s.n.*]: Springer Science & Business Media, 1996.

PROCHÁZKA, P. The bem applied to optimization and contact problems in geotechnics. **Acta Montana ICIt, CSAV, Ser. AI**, p. 21–32, 1992.

QIN, Q.-H.; MAI, Y.-W. Bem for crack-hole problems in thermopiezoelectric materials. **Engineering Fracture Mechanics**, Elsevier, v. 69, n. 5, p. 577–588, 2002.

RABOTNOV, Y. N. **Creep rupture**. [*S.l.: s.n.*]: Applied Mechanics: Proceedings of the Twelfth International Congress of Applied Mechanics, Stanford University, August 26–31, 1968, 1969.

RAVEENDRA, S.; CRUSE, T. Bem analysis of problems of fracture mechanics. **Developments in Boundary Element Methods: Industrial applications**, CRC Press, p. 182, 1989.

RAVNIK, J.; ŠKERGET, L.; HRIBERŠEK, M. The wavelet transform for bem computational fluid dynamics. **Engineering analysis with boundary elements**, Elsevier, v. 28, n. 11, p. 1303–1314, 2004.

RIBEIRO, T.; BEER, G.; DÜNSER, C. Efficient elastoplastic analysis with the boundary element method. **Computational Mechanics**, Springer, v. 41, p. 715–732, 2008.

RICCARDELLA, P. C. **An implementation of the boundary-integral technique for planar problems of elasticity and elasto-plasticity**. [*S.l.: s.n.*]: Carnegie Mellon University, 1973.

ROCHA, M. **Análise da fratura coesiva com base em formulações enriquecidas do Método dos Elementos de Contorno tridimensional**. 2020. Tese (Doutorado) — Universidade de São Paulo, 2020.

SALEH, A. L. *et al.* **Crack growth in concrete using boundary elements**. [*S.l.: s.n.*]: TOPICS IN ENGINEERING: Computational Mechanics Publications, 1997. v. 30.

SAUTER, S. A.; SCHWAB, C. Boundary element methods. *In*: **Boundary Element Methods**. [*S.l.: s.n.*]: Springer, 2010. p. 183–287.

SHAH, S. P.; SWARTZ, S. E.; OUYANG, C. **Fracture mechanics of concrete: applications of fracture mechanics to concrete, rock and other quasi-brittle materials**. [*S.l.: s.n.*]: John Wiley & Sons, 1995.

SILVA, R. C. d. S. **Análise tridimensional multifísica da difusão de cloretos em estruturas de concreto armado: uma abordagem pelo método dos elementos finitos**. 2023. Tese (Doutorado) — Universidade de São Paulo, 2023.

SIMPSON, R. N. *et al.* An isogeometric boundary element method for elastostatic analysis: 2d implementation aspects. **Computers & Structures**, Elsevier, v. 118, p. 2–12, 2013.

SIMPSON, R. N. *et al.* A two-dimensional isogeometric boundary element method for elastostatic analysis. **Computer Methods in Applied Mechanics and Engineering**, Elsevier, v. 209, p. 87–100, 2012.

SOARES, F. S.; ITURRIOZ, I. Modelagem do desenvolvimento de dano em materiais quase frágeis heterogênios utilizando uma versão do método de elementos discretos formados por barras. **Mecánica Computacional**, v. 34, n. 38, p. 2635–2652, 2016.

SWEDLOW, J.; CRUSE, T. Formulation of boundary integral equations for three-dimensional elasto-plastic flow. **International Journal of Solids and Structures**, Elsevier, v. 7, n. 12, p. 1673–1683, 1971.

TELES, D. V. C. **Mecânica do dano concentrado para meios bidimensionais: formulação para modo I com lei de dano não linear**. 2022. 107 p. Dissertação (Mestrado) — Programa de Pós-Graduação em Engenharia Civil, Universidade Federal de Sergipe, São Cristóvão, 2022.

TELLES, J.; BREBBIA, C. On the application of the boundary element method to plasticity. **Applied Mathematical Modelling**, Elsevier, v. 3, n. 6, p. 466–470, 1979.

TELLES, J.; BREBBIA, C. The boundary element method in plasticity. **Applied Mathematical Modelling**, Elsevier, v. 5, n. 4, p. 275–281, 1981.

TELLES, J. C. F. **The boundary element method applied to inelastic problems**. [*S.l.: s.n.*]: Springer Science & Business Media, 2012. v. 1.

TIMOSHENKO, S.; GOODIER, J. **Theory of elasticity. New York and London**. [*S.l.: s.n.*]: McGraw-Hill Book, 1934.

TONYALI, Z.; ATES, S. The coupling finite-boundary element method for soil-structure interaction under spatially varying ground motion. *In*: . [*S.l.: s.n.*], 2018.

VENTURINI, W.; BREBBIA, C. Boundary element formulation for nonlinear applications in geomechanics. **Applied Mathematical Modelling**, Elsevier, v. 8, n. 4, p. 251–260, 1984.

WINKLER, B.; HOFSTETTER, G.; NIEDERWANGER, G. Experimental verification of a constitutive model for concrete cracking. **Proceedings of the Institution of Mechanical Engineers, Part L: Journal of Materials: Design and Applications**, SAGE Publications Sage UK: London, England, v. 215, n. 2, p. 75–86, 2001.

ZHANG, Y.-M.; QU, W.-Z.; CHEN, J.-T. Bem analysis of thin structures for thermoelastic problems. **Engineering Analysis with Boundary Elements**, Elsevier, v. 37, n. 2, p. 441–452, 2013.

ZHONGHUA, L.; HAICHENG, G. Bauschinger effect and residual phase stresses in two ductile-phase steels: Part i. the influence of phase stresses on the bauschinger effect. **Metallurgical Transactions A**, Springer, v. 21, n. 2, p. 717–724, 1990.

ZHOU, X. *et al.* Damage evolution modeling for steel structures subjected to combined high cycle fatigue and high-intensity dynamic loadings. **International Journal of Structural Stability and Dynamics**, World Scientific, v. 22, n. 03n04, p. 2240012, 2022.

APPENDIX A – FUNDAMENTALS OF THE LINEAR ELASTICITY

This appendix outlines the key concepts of elasticity theory that are relevant to the BEM formulations discussed in this study. The present study is carried out only for a two-dimensional state of stress and strain, considering small displacements and deformations. Besides, the material is considered perfectly elastic, satisfying the conditions of homogeneity and isotropy. Firstly, consider a closed domain Ω with an enclosed boundary Γ, as shown in Figure A.

Figure 48 – Two-dimensional solid.
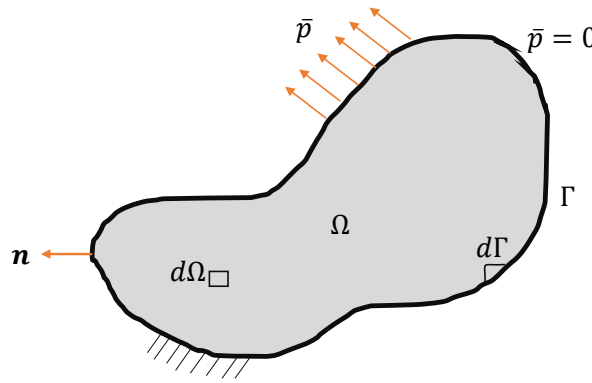
Source: The author

Considering an infinitesimal element $d\Omega$, the stress state inside the solid can be analyzed, as shown in Figure A. After balancing the moments, the Cauchy stress tensor is obtained:

$$\sigma_{ij} = \sigma_{ji}, \quad i = 1, 2 \tag{A.1}$$

Thus, the tensor is symmetrical, where there are only 6 independent stress components, as shown:

$$\sigma = \sigma^t = \begin{bmatrix} \sigma_{11} & \sigma_{12} & \sigma_{13} \\ \sigma_{12} & \sigma_{22} & \sigma_{23} \\ \sigma_{13} & \sigma_{23} & \sigma_{33} \end{bmatrix} = \sigma_{ij} = \sigma_{ji} \tag{A.2}$$

Moreover, the static equilibrium equations, considering the body forces b_i, are given by:

Figure 49 – Stress state in an infinitesimal element.
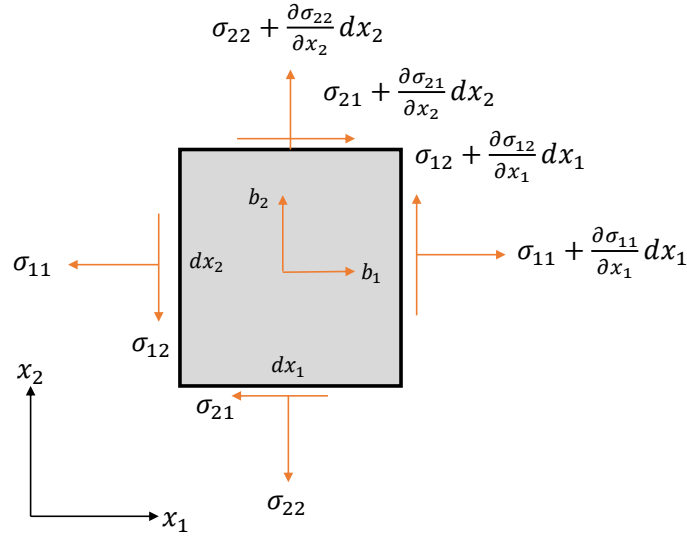
Source: The author

$$\sigma_{ij,j} + b_i = 0, \quad i = 1, 2. \tag{A.3}$$

The traction components at the boundary are defined from Cauchy's formula, which is obtained by the balance on an infinitesimal boundary element:

$$t_i = \sigma_{ij} n_j, \quad i = 1, 2. \tag{A.4}$$

where n_j are the outward unit normal vector components at the boundary.

It is also necessary to define the displacement field of a body when it is subjected to some variation. The resulting displacements come exclusively from deformation processes, once in structural terms, rigid body displacements (translations and rotations) are avoided through constraints. Thus, the linear stress tensor, which similarly to the stress one has 6 independent components, is defined as:

$$\varepsilon_{ij} = \frac{u_{i,j} + u_{j,i}}{2}, \quad i = 1, 2. \tag{A.5}$$

where u_i are the displacements.

Regarding now the constitutive relationships, through Hooke's law it is established that:

$$\sigma_{ij} = \lambda \delta_{ij} \varepsilon_{kk} + 2\mu \varepsilon_{ij} \tag{A.6}$$

where λ is the Lamé constant; and δ_{ij} is the Kronecker delta, as respectively shown:

$$\lambda = \frac{2v\mu}{(1 - 2v)} \tag{A.7}$$

$$\delta_{ij} = \begin{cases} 1, & i = j \\ 0, & i \neq j \end{cases} \tag{A.8}$$

The inverse relationship between strains and stresses is defined as

$$\varepsilon_{ij} = \frac{\sigma_{ij}}{2\mu} - \frac{\nu}{E}\sigma_{kk}\delta_{ij} \tag{A.9}$$

where μ is given by

$$\mu = \frac{E}{2(1 + v)} \tag{A.10}$$

If a plane stress state is considered, i.e, if $\sigma_{zz} = \sigma_{xz} = \sigma_{yz} = 0$, on the surface of the body and in its domain, the following relations are valid for the deformations:

$$\varepsilon_{zz} = -\frac{v}{1 - v}\left(\varepsilon_{xx} + \varepsilon_{yy}\right), \varepsilon_{xz} = \varepsilon_{yz} = 0 \tag{A.11}$$

On the other hand, if a plane strain state is taken into account, i.e, if $\varepsilon_{zz} = \varepsilon_{xz} = \varepsilon_{yz} = 0$, the following relationships are valid:

$$\sigma_{zz} = v\left(\sigma_{xx} + \sigma_{yy}\right), \sigma_{xz} = \sigma_{yz} = 0 \tag{A.12}$$

$$\varepsilon_{xx} = \frac{1 - v^2}{E}\left(\sigma_{xx} - \frac{v}{1 - v}\sigma_{yy}\right), \varepsilon_{yy} = \frac{1 - v^2}{E}\left(\sigma_{yy} - \frac{v}{1 - v}\sigma_{xx}\right) \text{ e } \varepsilon_{xy} = \frac{1 + v^2}{E}\sigma_{xy} \tag{A.13}$$

for the stresses and the strains, respectively.

The constitutive law in the plane strain state can represent the problems in the plane stress state by modifying the Poisson coefficient and the longitudinal modulus of elasticity of the material, through the following:

$$\bar{v} = \frac{v}{1+v} \tag{A.14}$$

$$\bar{E} = E \left[1 - \left(\frac{v}{1+v} \right)^2 \right] \tag{A.15}$$

Hence, the set of equations contemplating the equilibrium equations, the compatibility and the constitutive ones along with the boundary conditions form the boundary value problem. Such problems present an analytical solution for just a few range of problems. Numerical modelling is then required in order to abroad the applications of the method. In the present work, the BEM is adopted for obtaining the approximated results.

More specifically, for the problems herein analyzed, once the force and displacement values in the contour are known, it is necessary to determine the other unknown fields, for example, it is aimed to determine the internal fields, such as displacements, stresses and the deformation ones.

APPENDIX B – FUNDAMENTAL SOLUTIONS

Initially, consider that the body force in the differential equation that governs the problem (the equilibrium one, given in A.3) is represented by a punctual action whose intensity is provided by the Dirac Delta function. As it is known, such a function assumes an infinity value at its application point and zero at the other points of the domain. Thus, it is aimed to obtain the displacement field due to such action.

For that, in the first place, (A.6) is written in terms of displacements, by substituting (A.5) into it and by remembering that $\varepsilon_{kk} = u_{k,k}$:

$$\sigma_{ij} = \lambda \delta_{ij} u_{k,k} + \mu(u_{i,j} + u_{j,i}) \tag{B.1}$$

By taking the derivative of (B.1) and by remembering the relations shown in (A.7) and (A.10), after some manipulations, one obtains

$$\sigma_{ij,j} = G \left[\frac{u_{k,ki}}{(1 - 2v)} + u_{i,jj} \right] \tag{B.2}$$

Thus, replacing (B.2) into (A.3), the Navier's equation is obtained:

$$\frac{1}{1 - 2\nu} u_{j,ji} + u_{i,jj} + \frac{b_i}{\mu} = 0 \tag{B.3}$$

The solution of such a relation can be obtained via the Galerkin vector strategy, a vector which replaces the displacements by second-order derived functions, as shown:

$$u_i^* = \phi_{i,kk} - \frac{1}{2(1 - \nu)} \phi_{k,ik} \tag{B.4}$$

Hence, substituting (B.4) into (B.3) and considering (2.12), the following is written:

$$\mu \phi_{i,kkjj} - \frac{\mu}{2(1 - \nu)} \phi_{k,ikjj} + \frac{\mu}{(1 - \nu)} \left(\phi_{j,kkij} - \frac{1}{2(1 - \nu)} \phi_{k,jkij} \right) + \Delta \left(\mathbf{x} - \mathbf{x}' \right) e_i = 0 \tag{B.5}$$

Since $\phi_{k,jkij} = \phi_{k,jjki}$, $\phi_{j,kkjj} = \phi_{k,jjki}$, and $\phi_{k,ikjj} = \phi_{k,jjki}$, (B.12) is reduced to

$$\mu \phi_{i,kkjj} + \Delta \left(\mathbf{x} - \mathbf{x}' \right) e_i = 0 \tag{B.6}$$

or

$$\nabla^2 F_i + \frac{1}{\mu} \Delta \left(\mathbf{x} - \mathbf{x}' \right) e_i = 0 \tag{B.7}$$

where $F_i = \nabla^2 \phi_i$. The solution for such differential equation (B.7) is well known from the potential theory, given by:

$$F_i = -\frac{1}{2\pi\mu}\ln(r)e_i \tag{B.8}$$

which implies that

$$\phi_i = -\frac{1}{8\pi\mu}r^2\ln(r)e_i \tag{B.9}$$

Substituting (B.9) into (B.4) and considering the first relation shown in (2.15), the displacement fundamental solution is obtained according to:

$$U_{ij}^*\left(\mathbf{x}',\mathbf{x}\right) = \frac{1}{8\pi\mu(1-\nu)}\left[(3-4\nu)\ln\left(\frac{1}{r}\right)\delta_{ij} + r_{,i}r_{,j}\right] \tag{B.10}$$

satisfying, in this way, (B.3), where the distance derivatives are evaluated as:

$$r_{,i} = \frac{\partial r}{\partial x_i} = \frac{x_i - x_i'}{r} \tag{B.11}$$

$$\mu\phi_{i,kkjj} - \frac{\mu}{2(1-\nu)}\phi_{k,ikjj} + \frac{\mu}{(1-\nu)}\left(\phi_{j,kkij} - \frac{1}{2(1-\nu)}\phi_{k,jkij}\right) + \Delta\left(\mathbf{x}-\mathbf{x}'\right)e_i = 0 \tag{B.12}$$

The traction fundamental solution can be obtained from (A.5), the generalized Hooke's Law and then by applying (A.4), as follows:

$$T_{ij}^*\left(\mathbf{x}',\mathbf{x}\right) = -\frac{1}{4\pi(1-\nu)r}\left\{(1-2\nu)\left(r_{,j}n_i - r_{,i}n_j\right) + r_{,n}\left[(1-2\nu)\delta_{ij} + 2r_{,i}r_{,j}\right]\right\} \tag{B.13}$$

where

$$r_{,n} = \frac{\partial r}{\partial n} = r_{,m}n_m \tag{B.14}$$

From differentiating U_{ij}^* and T_{ij}^* with respect to $\mathbf{x}'$, the kernels for calculating the internal stresses shown in Eq. (2.18) are given by:

$$D_{kij}^*\left(\mathbf{x}',\mathbf{x}\right) = \frac{1}{4\pi(1-\nu)r}\left[(1-2\nu)\left(r_{,i}\delta_{jk} + r_{,j}\delta_{ik} - r_{,k}\delta_{ij}\right) + 2r_{,i}r_{,j}r_{,k}\right] \tag{B.15}$$

$$S_{kij}^*\left(\mathbf{x}',\mathbf{x}\right) = \frac{\mu}{2\pi(1-\nu)r^2}\left\{2\frac{\partial r}{\partial n}\left[(1-2\nu)r_{,k}\delta_{ij} + \nu\left(r_{,i}\delta_{jk} + r_{,j}\delta_{ik}\right) - 4r_{,i}r_{,j}r_{,k}\right]\right. +$$

$$\left. +2\nu\left(n_i r_{,j}r_{,k} + n_j r_{,i}r_{,k}\right) + (1-2\nu)\left(2n_k r_{,i}r_{,j} + n_i\delta_{jk} + n_j\delta_{ik}\right) - (1-4\nu)n_k\delta_{ij}\right\} \tag{B.16}$$

APPENDIX C – BODY FORCES

The presence of forces acting on the volume of a body can be represented by definite integrals over the problem domain. For the particular case of gravitational forces, b is constant, so $b = \rho(\mathbf{x})g(\mathbf{x})$, where $\rho(\mathbf{x})$ and $g(\mathbf{x})$ are the density of the material and the gravity's acceleration, respectively. The Galerkin vector can be used to transform the domain body force into boundary ones. The displacement fundamental solution is related to the Galerkin vector according to

$$U_{ij}^* \left(\mathbf{x}', \mathbf{x}\right) = \phi_{ij,kk}\left(\mathbf{x}', \mathbf{x}\right) - \frac{1}{2(1-v)}\phi_{ik,jk}\left(\mathbf{x}', \mathbf{x}\right) \tag{C.1}$$

and the domain integral can be written as

$$B_i = \int_\Omega U_{ij}^*\left(\mathbf{x}', \mathbf{x}\right)b_j(x)d\Omega = \int_\Omega \left[\phi_{ij,kk}\left(\mathbf{x}', \mathbf{x}\right) - \frac{1}{2(1-v)}\phi_{ik,jk}\left(\mathbf{x}', \mathbf{x}\right)\right]b_j d\Omega \tag{C.2}$$

Applying the Divergence theorem shown in (2.4) and taking the constant term b_j out of the integral, one obtains

$$B_i = b_j \int_\Gamma \left\{\phi_{ij,k} - \frac{1}{2(1-\nu)}\phi_{ik,j}\right\}n_k d\Gamma = \int_\Gamma P_i d\Gamma \tag{C.3}$$

where the solution of the Galerkin vector is given by

$$\phi_{ki} = \frac{-1}{8\pi G}r^2 \ln(r)\delta_{ki} \tag{C.4}$$

in which the δ_{ki} and r are the Kronecker Delta and the distance from the source point $\mathbf{x}'$ to field one $\mathbf{x}$. After substituting (C.1) into (C.3) and after some manipulations, one obtains:

$$P_i = \frac{r}{8\pi\mu}\left\{\left[2\ln\frac{1}{r} - 1\right]\left(b_i n_k r_{,k} - \frac{1}{2(1-v)}b_k r_{,k}n_i\right)\right\} \tag{C.5}$$

Notwithstanding, the domain term must be included in the internal stress values, that is:

$$\int_\Omega D_{kij}b_k d\Omega = \int_\Gamma D_{ij}d\Gamma \tag{C.6}$$

where

$$
\begin{aligned}
D_{ij} =& \frac{1}{8\pi} \left\{ 2n_m r_{,m} \left(b_i r_{,j} + b_j r_{,i} \right) \right. \\
&+ \frac{1}{1-v} \left[v\delta_{ij} \left(2n_m r_m b_k r_{,k} + \left[1 - 2\ln\frac{1}{r} \right] b_m n_m \right) - b_m r_{,m} \left(n_i r_j + n_j r_i \right) \right. \\
&\left. \left. + \frac{1-2v}{2} \left(1 - 2\ln\frac{1}{r} \right) \left(b_i n_j + b_j n_i \right) \right] \right\}
\end{aligned}
\tag{C.7}
$$

APPENDIX D – MATRICES FROM XLDM

In the present appendix, the matrixes and vectors of the XLDM theory are presented. First, the kinematic matrixes are introduced. These include a matrix that converts displacements to strains, another that transforms displacements to the elongations of *numexes*, and a third that converts *numexes* elongations to strains. The first one, featured in Eq. 4.11, is expressed as follows:

$$[B]_b = \begin{bmatrix} \partial\phi_i/\partial x_1 & 0 & \partial\phi_j/\partial x_1 & 0 & \partial\phi_k/\partial x_1 & 0 & \partial\phi_l/\partial x_1 & 0 \\ 0 & \partial\phi_i/\partial x_2 & 0 & \partial\phi_j/\partial x_2 & 0 & \partial\phi_k/\partial x_2 & 0 & \partial\phi_l/\partial x_2 \\ \partial\phi_i/\partial x_2 & \partial\phi_i/\partial x_1 & \partial\phi_j/\partial x_2 & \partial\phi_j/\partial x_1 & \partial\phi_k/\partial x_2 & \partial\phi_k/\partial x_1 & \partial\phi_l/\partial x_2 & \partial\phi_l/\partial x_1 \end{bmatrix}$$
(D.1)

in which ϕ_i, ϕ_j, ϕ_k and ϕ_l are the shape functions of the element.

The second transformation matrix, presented in Eq. 4.13, is given by:

$$[\mathbf{b}]_b = \begin{bmatrix} b_{11} & b_{12} & b_{13} & b_{14} & 0 & 0 & 0 & 0 \\ b_{21} & b_{22} & 0 & 0 & b_{25} & b_{26} & 0 & 0 \\ b_{31} & b_{32} & 0 & 0 & 0 & 0 & b_{37} & b_{38} \\ 0 & 0 & b_{43} & b_{44} & b_{45} & b_{46} & 0 & 0 \\ 0 & 0 & 0 & 0 & b_{55} & b_{56} & b_{57} & b_{58} \end{bmatrix}$$
(D.2)

where the coefficients b_{ij} are defined as follows:

$$b_{11} = \frac{x_i - x_j}{\sqrt{(x_j - x_i)^2 + (y_j - y_i)^2}} \quad b_{12} = \frac{y_i - y_j}{\sqrt{(x_j - x_i)^2 + (y_j - y_i)^2}}$$
$$b_{13} = \frac{x_j - x_i}{\sqrt{(x_j - x_i)^2 + (y_j - y_i)^2}} \quad b_{14} = \frac{y_j - y_i}{\sqrt{(x_j - x_i)^2 + (y_j - y_i)^2}}$$
(D.3)

$$b_{21} = \frac{x_i - x_k}{\sqrt{(x_k - x_i)^2 + (y_k - y_i)^2}} \quad b_{22} = \frac{y_i - y_k}{\sqrt{(x_k - x_i)^2 + (y_k - y_i)^2}}$$
$$b_{25} = \frac{x_k - x_i}{\sqrt{(x_k - x_i)^2 + (y_k - y_i)^2}} \quad b_{26} = \frac{y_k - y_i}{\sqrt{(x_k - x_i)^2 + (y_k - y_i)^2}}$$
(D.4)

$$b_{31} = \frac{x_i - x_l}{\sqrt{(x_l - x_i)^2 + (y_l - y_i)^2}} \quad b_{32} = \frac{y_i - y_l}{\sqrt{(x_l - x_i)^2 + (y_l - y_i)^2}}$$
$$b_{37} = \frac{x_l - x_i}{\sqrt{(x_l - x_i)^2 + (y_l - y_i)^2}} \quad b_{38} = \frac{y_l - y_i}{\sqrt{(x_l - x_i)^2 + (y_l - y_i)^2}}$$
(D.5)

$$b_{43} = \frac{x_j - x_k}{\sqrt{(x_k - x_j)^2 + (y_k - y_j)^2}} \qquad b_{44} = \frac{y_j - y_k}{\sqrt{(x_k - x_j)^2 + (y_k - y_j)^2}}$$

$$b_{45} = \frac{x_k - x_j}{\sqrt{(x_k - x_j)^2 + (y_k - y_j)^2}} \qquad b_{46} = \frac{y_k - y_j}{\sqrt{(x_k - x_j)^2 + (y_k - y_j)^2}} \tag{D.6}$$

$$b_{55} = \frac{x_k - x_l}{\sqrt{(x_l - x_k)^2 + (y_l - y_k)^2}} \qquad b_{56} = \frac{y_k - y_l}{\sqrt{(x_l - x_k)^2 + (y_l - y_k)^2}}$$

$$b_{57} = \frac{x_l - x_k}{\sqrt{(x_l - x_k)^2 + (y_l - y_k)^2}} \qquad b_{58} = \frac{y_l - y_k}{\sqrt{(x_l - x_k)^2 + (y_l - y_k)^2}} \tag{D.7}$$

Finally, the third transformation matrix, presented in Eq. 4.14, is defined by a simple multiplication of the two previous matrixes, as already shown in Eq. 4.15, but rewritten here for the sake of completeness:

$$[\boldsymbol{T}]_b = \left([\boldsymbol{B}]_b [\boldsymbol{b}]_b^T\right) \left([\boldsymbol{b}]_b [\boldsymbol{b}]_b^T\right)^{-1} \tag{D.8}$$

Finally, the vector containing the elongations due to damage of the *numexes*, shown in 4.17, is expressed by the following relationship:

$$\{\boldsymbol{\delta}\}^d = [\boldsymbol{b}]\{\boldsymbol{q}\}^d \tag{D.9}$$

where $\{\boldsymbol{q}\}^d$ is the vector of displacements due to damage, defined as:

$$\left\{\boldsymbol{q}^d\right\} = \left\{ \begin{array}{c} s_{ij} \cdot e_i^{ij} - s_{il} \cdot e_i^{il} \\ -c_{ij} \cdot e_i^{ij} + c_{il} \cdot e_i^{il} \\ s_{ij} \cdot e_j^{ij} + s_{jk} \cdot e_j^{jk} \\ -c_{ij} \cdot e_j^{ij} - c_{jk} \cdot e_j^{jk} \\ s_{jk} \cdot e_k^{jk} - s_{lk} \cdot e_k^{lk} \\ -c_{jk} \cdot e_k^{jk} + c_{lk} \cdot e_k^{lk} \\ -s_{il} \cdot e_l^{il} - s_{lk} \cdot e_l^{lk} \\ c_{il} \cdot e_l^{il} + c_{lk} \cdot e_l^{lk} \end{array} \right\} \tag{D.10}$$

where s_{ij} and c_{ij} are the sine and cosine of the angle between the i and j nodes, respectively, and e_i^{ij} is the band thickness of the element ij at node i, and so on for the other indexes.

The matrices of the linerized system of equations given in Eq. 4.31 are presented below. The derivative of the elasticity matrix with respect to the stress is performed for every node, as follows:

$$
\left[\frac{\partial \boldsymbol{R}}{\partial \boldsymbol{\sigma}}\right]_{12\times12} =
\begin{bmatrix}
\frac{\partial R1}{\partial \sigma_{11}^i} & \frac{\partial R1}{\partial \sigma_{22}^i} & \frac{\partial R1}{\partial \sigma_{12}^i} & \frac{\partial R1}{\partial \sigma_{11}^j} & \frac{\partial R1}{\partial \sigma_{22}^j} & \frac{\partial R1}{\partial \sigma_{12}^j} & \frac{\partial R1}{\partial \sigma_{11}^k} & \frac{\partial R1}{\partial \sigma_{22}^k} & \frac{\partial R1}{\partial \sigma_{12}^k} & \frac{\partial R1}{\partial \sigma_{11}^l} & \frac{\partial R1}{\partial \sigma_{22}^l} & \frac{\partial R1}{\partial \sigma_{12}^l} \\
\frac{\partial R2}{\partial \sigma_{11}^i} & \frac{\partial R2}{\partial \sigma_{22}^i} & \frac{\partial R2}{\partial \sigma_{12}^i} & \frac{\partial R2}{\partial \sigma_{11}^j} & \frac{\partial R2}{\partial \sigma_{22}^j} & \frac{\partial R2}{\partial \sigma_{12}^j} & \frac{\partial R2}{\partial \sigma_{11}^k} & \frac{\partial R2}{\partial \sigma_{22}^k} & \frac{\partial R2}{\partial \sigma_{12}^k} & \frac{\partial R2}{\partial \sigma_{11}^l} & \frac{\partial R2}{\partial \sigma_{22}^l} & \frac{\partial R2}{\partial \sigma_{12}^l} \\
\frac{\partial R3}{\partial \sigma_{11}^i} & \frac{\partial R3}{\partial \sigma_{22}^i} & \frac{\partial R3}{\partial \sigma_{12}^i} & \frac{\partial R3}{\partial \sigma_{11}^j} & \frac{\partial R3}{\partial \sigma_{22}^j} & \frac{\partial R3}{\partial \sigma_{12}^j} & \frac{\partial R3}{\partial \sigma_{11}^k} & \frac{\partial R3}{\partial \sigma_{22}^k} & \frac{\partial R3}{\partial \sigma_{12}^k} & \frac{\partial R3}{\partial \sigma_{11}^l} & \frac{\partial R3}{\partial \sigma_{22}^l} & \frac{\partial R3}{\partial \sigma_{12}^l} \\
\frac{\partial R4}{\partial \sigma_{11}^i} & \frac{\partial R4}{\partial \sigma_{22}^i} & \frac{\partial R4}{\partial \sigma_{12}^i} & \frac{\partial R4}{\partial \sigma_{11}^j} & \frac{\partial R4}{\partial \sigma_{22}^j} & \frac{\partial R4}{\partial \sigma_{12}^j} & \frac{\partial R4}{\partial \sigma_{11}^k} & \frac{\partial R4}{\partial \sigma_{22}^k} & \frac{\partial R4}{\partial \sigma_{12}^k} & \frac{\partial R4}{\partial \sigma_{11}^l} & \frac{\partial R4}{\partial \sigma_{22}^l} & \frac{\partial R4}{\partial \sigma_{12}^l} \\
\frac{\partial R5}{\partial \sigma_{11}^i} & \frac{\partial R5}{\partial \sigma_{22}^i} & \frac{\partial R5}{\partial \sigma_{12}^i} & \frac{\partial R5}{\partial \sigma_{11}^j} & \frac{\partial R5}{\partial \sigma_{22}^j} & \frac{\partial R5}{\partial \sigma_{12}^j} & \frac{\partial R5}{\partial \sigma_{11}^k} & \frac{\partial R5}{\partial \sigma_{22}^k} & \frac{\partial R5}{\partial \sigma_{12}^k} & \frac{\partial R5}{\partial \sigma_{11}^l} & \frac{\partial R5}{\partial \sigma_{22}^l} & \frac{\partial R5}{\partial \sigma_{12}^l} \\
\frac{\partial R6}{\partial \sigma_{11}^i} & \frac{\partial R6}{\partial \sigma_{22}^i} & \frac{\partial R6}{\partial \sigma_{12}^i} & \frac{\partial R6}{\partial \sigma_{11}^j} & \frac{\partial R6}{\partial \sigma_{22}^j} & \frac{\partial R6}{\partial \sigma_{12}^j} & \frac{\partial R6}{\partial \sigma_{11}^k} & \frac{\partial R6}{\partial \sigma_{22}^k} & \frac{\partial R6}{\partial \sigma_{12}^k} & \frac{\partial R6}{\partial \sigma_{11}^l} & \frac{\partial R6}{\partial \sigma_{22}^l} & \frac{\partial R6}{\partial \sigma_{12}^l} \\
\frac{\partial R7}{\partial \sigma_{11}^i} & \frac{\partial R7}{\partial \sigma_{22}^i} & \frac{\partial R7}{\partial \sigma_{12}^i} & \frac{\partial R7}{\partial \sigma_{11}^j} & \frac{\partial R7}{\partial \sigma_{22}^j} & \frac{\partial R7}{\partial \sigma_{12}^j} & \frac{\partial R7}{\partial \sigma_{11}^k} & \frac{\partial R7}{\partial \sigma_{22}^k} & \frac{\partial R7}{\partial \sigma_{12}^k} & \frac{\partial R7}{\partial \sigma_{11}^l} & \frac{\partial R7}{\partial \sigma_{22}^l} & \frac{\partial R7}{\partial \sigma_{12}^l} \\
\frac{\partial R8}{\partial \sigma_{11}^i} & \frac{\partial R8}{\partial \sigma_{22}^i} & \frac{\partial R8}{\partial \sigma_{12}^i} & \frac{\partial R8}{\partial \sigma_{11}^j} & \frac{\partial R8}{\partial \sigma_{22}^j} & \frac{\partial R8}{\partial \sigma_{12}^j} & \frac{\partial R8}{\partial \sigma_{11}^k} & \frac{\partial R8}{\partial \sigma_{22}^k} & \frac{\partial R8}{\partial \sigma_{12}^k} & \frac{\partial R8}{\partial \sigma_{11}^l} & \frac{\partial R8}{\partial \sigma_{22}^l} & \frac{\partial R8}{\partial \sigma_{12}^l} \\
\frac{\partial R9}{\partial \sigma_{11}^i} & \frac{\partial R9}{\partial \sigma_{22}^i} & \frac{\partial R9}{\partial \sigma_{12}^i} & \frac{\partial R9}{\partial \sigma_{11}^j} & \frac{\partial R9}{\partial \sigma_{22}^j} & \frac{\partial R9}{\partial \sigma_{12}^j} & \frac{\partial R9}{\partial \sigma_{11}^k} & \frac{\partial R9}{\partial \sigma_{22}^k} & \frac{\partial R9}{\partial \sigma_{12}^k} & \frac{\partial R9}{\partial \sigma_{11}^l} & \frac{\partial R9}{\partial \sigma_{22}^l} & \frac{\partial R9}{\partial \sigma_{12}^l} \\
\frac{\partial R10}{\partial \sigma_{11}^i} & \frac{\partial R10}{\partial \sigma_{22}^i} & \frac{\partial R10}{\partial \sigma_{12}^i} & \frac{\partial R10}{\partial \sigma_{11}^j} & \frac{\partial R10}{\partial \sigma_{22}^j} & \frac{\partial R10}{\partial \sigma_{12}^j} & \frac{\partial R10}{\partial \sigma_{11}^k} & \frac{\partial R10}{\partial \sigma_{22}^k} & \frac{\partial R10}{\partial \sigma_{12}^k} & \frac{\partial R10}{\partial \sigma_{11}^l} & \frac{\partial R10}{\partial \sigma_{22}^l} & \frac{\partial R10}{\partial \sigma_{12}^l} \\
\frac{\partial R11}{\partial \sigma_{11}^i} & \frac{\partial R11}{\partial \sigma_{22}^i} & \frac{\partial R11}{\partial \sigma_{12}^i} & \frac{\partial R11}{\partial \sigma_{11}^j} & \frac{\partial R11}{\partial \sigma_{22}^j} & \frac{\partial R11}{\partial \sigma_{12}^j} & \frac{\partial R11}{\partial \sigma_{11}^k} & \frac{\partial R11}{\partial \sigma_{22}^k} & \frac{\partial R11}{\partial \sigma_{12}^k} & \frac{\partial R11}{\partial \sigma_{11}^l} & \frac{\partial R11}{\partial \sigma_{22}^l} & \frac{\partial R11}{\partial \sigma_{12}^l} \\
\frac{\partial R12}{\partial \sigma_{11}^i} & \frac{\partial R12}{\partial \sigma_{22}^i} & \frac{\partial R12}{\partial \sigma_{12}^i} & \frac{\partial R12}{\partial \sigma_{11}^j} & \frac{\partial R12}{\partial \sigma_{22}^j} & \frac{\partial R12}{\partial \sigma_{12}^j} & \frac{\partial R12}{\partial \sigma_{11}^k} & \frac{\partial R12}{\partial \sigma_{22}^k} & \frac{\partial R12}{\partial \sigma_{12}^k} & \frac{\partial R12}{\partial \sigma_{11}^l} & \frac{\partial R12}{\partial \sigma_{22}^l} & \frac{\partial R12}{\partial \sigma_{12}^l}
\end{bmatrix}
\tag{D.11}
$$

where $R1$, $R2$ and $R3$ are the elasticity laws evaluated for node i; $R4$, $R5$ and $R6$ are the elasticity laws evaluated for node j, and so on. Thus, by recalling the initial relation presented in Eq. 4.28, the derivatives above yield a 12×12 identity matrix.

The derivative of the elasticity law with respect to the band thickness for each node is defined as:

$$
\left[\frac{\partial R}{\partial \delta}\right]_{3x8} = [\boldsymbol{H}]_{(3x3)}[\boldsymbol{T}]_{(3x5)}[\boldsymbol{B}]_{(5x8)} \left[\frac{\partial \{\boldsymbol{q}^d\}}{\partial \{\boldsymbol{\delta}\}}\right]_{(8\times8)}
\tag{D.12}
$$

in which $\left[\frac{\partial \{\boldsymbol{q}^d\}}{\partial \{\boldsymbol{\delta}\}}\right]$ is easily obtained by differentiating the vector $\{\boldsymbol{q}^d\}$ given in D.9 with respect to the band thickness, as follows:

$$
\left[\frac{\partial \boldsymbol{R}}{\partial \boldsymbol{\delta}}\right]_{8\times8} =
\begin{bmatrix}
sin_{ij} & 0 & -sin_{il} & 0 & 0 & 0 & 0 & 0 \\
-cos_{ij} & 0 & cos_{il} & 0 & 0 & 0 & 0 & 0 \\
0 & sin_{ij} & 0 & 0 & sin_{jk} & 0 & 0 & 0 \\
0 & cos_{ij} & 0 & 0 & -cos_{jk} & 0 & 0 & 0 \\
0 & 0 & 0 & 0 & 0 & sin_{jk} & 0 & -sin_{lk} \\
0 & 0 & 0 & 0 & 0 & -cos_{jk} & 0 & cos_{lk} \\
0 & 0 & 0 & -sin_{il} & 0 & 0 & -sin_{lk} & 0 \\
0 & 0 & 0 & cos_{il} & 0 & 0 & cos_{lk} & 0
\end{bmatrix}
\tag{D.13}
$$

In sequence, for obtaining the derivative of the damage law with respect to the stresses, recall the relation given in 4.19. Thus, for sake of readability, the obtained matrix

is presented as:

$$
\begin{bmatrix}
a & b & c & 0 & 0 & 0 & 0 & 0 & 0 & 0 & 0 & 0 \\
0 & 0 & 0 & a & b & c & 0 & 0 & 0 & 0 & 0 & 0 \\
d & e & f & 0 & 0 & 0 & 0 & 0 & 0 & 0 & 0 & 0 \\
0 & 0 & 0 & 0 & 0 & 0 & 0 & 0 & 0 & d & e & f \\
0 & 0 & 0 & g & h & i & 0 & 0 & 0 & 0 & 0 & 0 \\
0 & 0 & 0 & 0 & 0 & 0 & g & h & i & 0 & 0 & 0 \\
0 & 0 & 0 & 0 & 0 & 0 & 0 & 0 & 0 & j & k & l \\
0 & 0 & 0 & 0 & 0 & 0 & j & k & l & 0 & 0 & 0
\end{bmatrix}
\tag{D.14}
$$

where

$$
\begin{aligned}
&\text{a} = \sin^2_{ij} && \text{b} = \cos^2_{ij} && c = -2\cos_{ij}\sin_{ij} \\
&d = \sin^2_{il} && e = \cos^2_{il} && f = -2\cos_{il}\sin_{il} \\
&g = \sin^2_{jk} && h = \cos^2_{jk} && i = -2\cos_{jk}\sin_{jk} \\
&j = \sin^2_{lk} && k = \cos^2_{lk} && l = -2\cos_{lk}\sin_{lk}
\end{aligned}
\tag{D.15}
$$

Finally, the last derivative is the one of the damage law with respect to the band thickness, which is given by the subsequent diagonal matrix:

$$
\left[\frac{\partial g}{\partial \delta}\right]_{8x8} =
\begin{bmatrix}
a_{11} & 0 & 0 & 0 & 0 & 0 & 0 & 0 \\
0 & a_{22} & 0 & 0 & 0 & 0 & 0 & 0 \\
0 & 0 & a_{33} & 0 & 0 & 0 & 0 & 0 \\
0 & 0 & 0 & a_{44} & 0 & 0 & 0 & 0 \\
0 & 0 & 0 & 0 & a_{55} & 0 & 0 & 0 \\
0 & 0 & 0 & 0 & 0 & a_{66} & 0 & 0 \\
0 & 0 & 0 & 0 & 0 & 0 & a_{77} & 0 \\
0 & 0 & 0 & 0 & 0 & 0 & 0 & a_{88}
\end{bmatrix}
\tag{D.16}
$$

in which

$$
a_{11} = -\sigma_{cr}qe^{q\delta^i_{ij}} \quad a_{22} = -\sigma_{cr}qe^{q\delta^j_{ij}} \quad a_{33} = -\sigma_{cr}qe^{q\delta^i_{il}} \quad a_{44} = -\sigma_{cr}qe^{q\delta^l_{il}}
$$

$$
a_{55} = -\sigma_{cr}qe^{q\delta^j_{jk}} \quad a_{66} = -\sigma_{cr}qe^{q\delta^k_{jk}} \quad a_{77} = -\sigma_{cr}qe^{q\delta^l_{lk}} \quad a_{88} = -\sigma_{cr}qe^{q\delta^k_{lk}}
\tag{D.17}
$$